Czech Technical University in Prague
Faculty of Nuclear Sciences and Physical Engineering
Department of Physics

Diploma Thesis

Measurement of Magnetic Fields on GOLEM Tokamak

Author: **Bc. Tomáš Markovič**

Supervisor: **Ing. Ivan Ďuran, Ph.D.** **Prague, 2012**

insert assignment here

Prohlášení

Prohlašuji, že jsem svou diplomovou práci vypracoval samostatně a použil jsem pouze podklady uvedené v přiloženém seznamu.

Nemám závažný důvod proti užití tohoto školního díla ve smyslu § 60 Zákona č.121/2000 Sb., o právu autorském, o právech souvisejících s právem autorským a o změně některých zákonu (autorský zákon).

V Praze dne ______________ ____________________

podpis

Acknowledgements

I would like to express my gratitude to my advisor, Ing. Ivan Ďuran, Ph.D. for his guidance, supervision and patience over the course of past years and for his help and numerous valuable advices on the field of research and beyond. Furthermore, I am thankful to Ing. Vojtěch Svoboda, Csc. for enabling me to work with tokamak GOLEM from the very first year of my studies and for his thoughtful advice and help, when I was standing on crossroads of my life. My thanks also goes to RNDr. Jan Mlynář, Ph.D. for his humane approach to students and for his valuable advices on priorities in one's life. Finally, my endless gratitude belongs to my family, for their support in the course of past years and for enduring my constant absence.

Název práce: Měření magnetických polí na tokamaku GOLEM

Autor: Bc. Tomáš Markovič

Obor: Fyzikální inženýrství

Druh práce: Diplomová práce

Vedoucí práce: Ing. Ivan Ďuran, Ph.D., Ústav fyziky plazmatu, AV ČR

Abstrakt:

Tato práce pojednává of problematice magnetických polí zařízení typu tokamak, jmenovitě o jejich generaci, metodách jejich detekce a metodach interpretace měření. Pro tyto účely je podán přehledný soupis senzorů magnetických polí tokamaku GOLEM, včetně vysvětlení jejich základních principů a kalibračních konstant. Toto se netýká pouze stávající diagnostiky, činící 2 smyčky na detekci globálních magnetických toků, Rogowského pásku k detekci I_p, sedlové cívky na detekci průmerného vertikálního pole a malých cívek k lokální detekci B_ϕ a B_θ, nýbrž také diagnostiky nově zaváděné. Konkrétně, sady 16 cívek a teplotně odolných Hallových sond dodaných Poznan University of Technology. Za použití nové sady detekčních cívek bylo vykonáno systematické měření rozptylových polí, kde se ukázalo že s největší pravděpodobností je hlavní příčinou jejich generace saturace transformátorového jádra (a tedy pole indukované proudy v komoře tokamaku). I když se zdá že použití těchto cívek k detekci nízkofrekvenčního signálu plazmatu není plně optimální, vykazují velice dobré výsledky v oblasti detekce fluktuací B_θ, což je mimo jiné jejich hlavní účel. Díky tomu bylo možné detekovat a charakterizovat MHD magnetické ostrovy na tokamaku GOLEM. Bylo pozorováno jak tyto ostrovy mění frekvenci své poloidální rotace sledováním změny q a jak tato rotace závisí také na struktuře ostrovů a na eventuální přítomnosti stabilizačního B_R pole. Mimo jiného byl také vyvinut model magnetických polí tokamaku, zahrnující vinutí B_ϕ a B_θ, jádro tokamaku a jeho komoru (jako potenciální zdroj rozptylových polí). Do modelu je zahrnut také jednoduchý model magnetických ostrovů.

Klíčová slova: Magnetická diagnostika, tokamak GOLEM, magnetické cívky, Hallův jev, model magnetických polí, FFT, cross-korelační analýza, model ferromagnetika, magnetické ostrovy.

Title: Measurement of magnetic fields on GOLEM tokamak

Author: Bc. Tomáš Markovič

Abstract:

In this thesis, a characterization of tokamak GOLEM magnetic fields and of methods of their measurement is provided. Specifically, calibration constants and methods of application of magnetic diagnostics on this device are summarized. This includes not only up-to date detectors of global discharge parameters, but also new detectors for local B_θ perturbation studies. Design, manufacture, calibration and tokamak implementation of the latter diagnostics (refered to as *ring coils*) is described in detail. Temperature-resistant state-of-art Hall probes provided by Poznan University of Technology are characterized as well, althought their tokamak implementation did not take place yet. Measurements of stray fields on tokamak GOLEM using ring coils suggest, that main cause of their presence is local saturation of ferromagnetic core, i.e. not currents in tokamak chamber. Measurement of plasma B_θ by ring coils was found to be less reliable as B_θ fluctuation measurement. The latter allows detection and characterization of plasma MHD structures – the magnetic islands. An investigation of tokamak GOLEM islands yields that they change their poloidal rotation frequency by following change in q, most likely due to tendencies to keep constant v_θ. For $m = 3$ islands, $v_\theta \approx 0.7$ km/s is observed, however for discharges with vertical stabilization horizontal field, island $v_\theta \approx 2.0$ km/s velocities are typical. Also, model of tokamak GOLEM magnetic field was developed. Model includes fields by windings of B_ϕ and external B_θ, by tokamak iron core and by tokamak chamber currents. A model of plasma B_θ perturbation field from MHD structures is presented as well.

Key Words: Magnetic diagnostics, tokamak GOLEM, detection coils, Hall effect, model of magnetic fields, FFT, cross-correlation, ferromagnetic model, magnetic islands.

Chapter 1

Introduction

Sun is principal source of energy of all the natural processes taking place around us, such as circulation of water, tidal effects, atmospheric processes or drive of food chain. Our star has been an object of our observations and source of inspiration over the whole course of history of mankind. Attempts at imitating this source of energy – i.e. large-scale reproduction of fusion nuclear reactions on our planet, are therefore understandable and natural. Energy of 17.6 MeV is released by fusion of two nuclei of hydrogen isotopes – deuterium (D) and tritium (T). This implies that 1 kg of DT gas mixture is sufficient fuel for 1 GW power-plant for the whole day (ref. [1]). Literature [2] points-out that eventual fusion power station would be of large-scale character only. However, advantages of fuel abundance (D is obtained from water and T bred from Li), inherent safety of reactor and even lesser environmental impact than that of fission nuclear reactors, are more than enough to counterweight this limitation. To effectively harness fusion energy, the fuel needs to be in thermal equilibrium and in form of ionized gas – plasma, the fourth state of matter. There are several approaches how to effectively provide this, with tokamak reactor concept being currently the most popular and successful. Since late 60's, tokamak research has progressed significantly – there are currently about 30 operational experimental reactors worldwide. Additionally, in the past 10-15 years there was a significant improvement in the field of particle transport, fuel operational density and its stability (ref. [3]). Not to mention that construction of ITER reactor of intended heat power output being 10 × higher than input is planned to finish in 2020 (ref. [4]).

This thesis is aimed on one aspect of tokamak research – tokamak magnetic fields, specifically those of tokamak GOLEM. Following sections of this chapter provide overview of magnetic fields present in tokamak devices, as well as implications of presence of these fields for device operation. Magnetohydrodynamics (MHD) approach to plasma stability issues and introduction of tokamak GOLEM are contained within this chapter as well. Chapter 2 describes used methods of tokamak GOLEM magnetic field measurements, and provides calibration constants of respective sensors. For studies of plasma MHD instabilities, up-to date magnetic diagnostics on this tokamak was not sufficient. Therefore, chapter 3 refers about design, construction, calibration and installation of a new set of magnetic diagnostics probes. Given their way of implementation into tokamak chamber, these sensors are named as *ring coils.* Investigation of applicability of ring coils for measurements of plasma magnetic field is provided in chapter 5. This concerns mainly implications for plasma position measurements. However, since coils detect net magnetic field from tokamak windings and plasma, the preceding chapter 4 introduces detailed models of tokamak pre-breakdown (vacuum) magnetic fields. Models are intended for determination, resp. estimation of contribution of tokamak winding fields in net magnetic field signal, which is demonstrated in chapter 5 as well. Still, the main purpose of ring coils is to detect fluctuations of plasma magnetic field, rather than its unperturbed magnitude. This is how plasma MHD structures manifest their presence, as it is shown in chapter 6. Resultant measurement and discussion of these structures on tokamak GOLEM is contained in chapter 7. Summarization of key findings, as well as proposal for future work is provided in summary (chap. 8).

1.1 Tokamak magnetic fields

Let there be D-T fusion reaction:

$$^{2}\mathrm{H} +^{3}\mathrm{H} \rightarrow \mathrm{n}\ (14.1 MeV) +^{4}\mathrm{He}\ (3.5 MeV)$$

and let ε_α denote 3.5 MeV energy of He product. Neutron takes 4/5 of fusion energy to the reactor wall, where this energy is absorbed and used in thermal cycle of eventual power-plant, while ε_α energy of α particle stays in reacting medium. Literature [1] shows that total rate of reactions of particles, having differential cross-section $\sigma(v_1 - v_2)$ and velocity distribution functions $f_1(v_1)$ and $f_2(v_2)$, is

$$\mathfrak{R} = \int\int \sigma(v_1 - v_2) \cdot (v_1 - v_2) \cdot f_1(v_1) f_2(v_2) \mathrm{d}v_1^3 \mathrm{d}v_2^3.$$

Fusion fuel is thermalized, thus f_i equals to Maxwellian distribution, i.e. $\mathfrak{R} = n_d n_t \overline{\sigma v}$, where overline represents integration over velocity dimensions. If densities of fuel com-

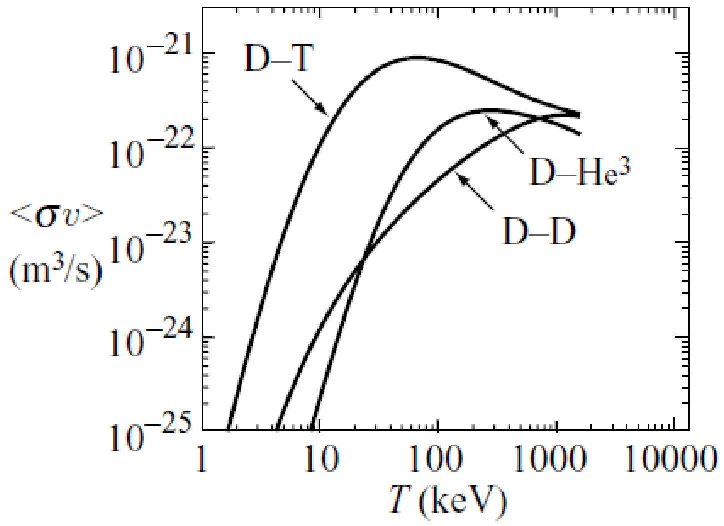

Figure 1.1: Temperature dependence of $\overline{\sigma v}$ quantity for top fusion reactions [2].

ponents are $n_d = n_t = n/2$, then heating power per unit volume of reacting medium is (ref. [1]):

$$P_H = \frac{1}{4} n^2 \overline{\sigma v} \varepsilon_\alpha$$

Let now τ_e denote *confinement time* representing loss of energy in manner:

$$P_L = \frac{W}{\tau_e} \,,$$

where P_L is energy loss power per unit volume and $W = 3\overline{nT}$ is total plasma energy density (see ref. [1]). In this case, overline represents integration over space dimensions. *Fusion ignition* refers to reactor-optimal conditions of $P_H = P_L$, i.e. when fusion reaction provides 1/5 of its output power to cover for energy losses of its fuel, while 4/5 of the power becomes part of thermal cycle of power-plant. This happens once:

$$n\tau_e > \frac{12}{\overline{\sigma v}} \frac{T}{\varepsilon_\alpha} \,.$$

Looking on plot in fig. 1.1, it can be seen that it is optimal to thermalize fusion fuel at $T \approx 30$ keV. At such conditions, work gas is in fully ionized state of *plasma*. To raise τ_e and prevent drop in T (mind that $\overline{\sigma v} \sim T^2$ for $T \approx 30$ keV), plasma is kept from contact with reactor wall by magnetic fields.

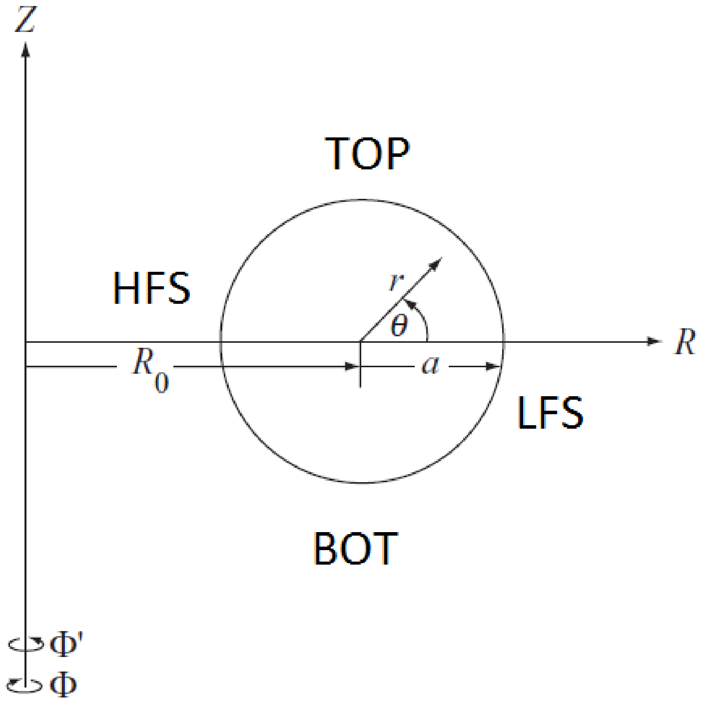

Figure 1.2: Coordinate system assumed in the whole thesis (ref. [2]).

Fig. 1.3 shows magnetic field in tokamak, along with windings of its generation. Main confinement field is of toroidal character (referred to as B_ϕ) – see fig. 1.3, generated by number of coils distributed all around the chamber. In chapter 4 it is shown, that $B_\phi \sim 1/R$ i.e. $\nabla B \neq 0$. Gyrating center motion approach (ref. [5]) for plasma particles in magnetic field yields:

$$\dot{\mathbf{R}}_\perp = \frac{\mathbf{F_{ext}} \times \mathbf{B} - \mu \nabla B \times \mathbf{B} - m\ddot{\mathbf{R}} \times \mathbf{B}}{QB^2} \,. \tag{1.1}$$

$\dot{\mathbf{R}}_\perp$ represents velocity of center of motion perpendicular to magnetic field lines, $\mathbf{F_{ext}}$ external force, Q particle charge, m its mass and $\mu = \frac{mv_\perp^2}{2B}$, where $v_\perp$ is particle velocity component perpendicular to magnetic field lines. $B_\phi \sim 1/R$ thus yields motion of plasma particles across the field lines:

$$\dot{R}_Z = \frac{mv_\perp^2}{2q} \frac{1}{B_\phi(R_0)R_0} \,. \tag{1.2}$$

Above expression represents upwards motion of positive ions and downwards motion of electrons, which leads to charge separation and induction of downwards-oriented $\mathbf{E}$. Then, $\mathbf{F_{ext}}$ term of eq. 1.1 yields that:

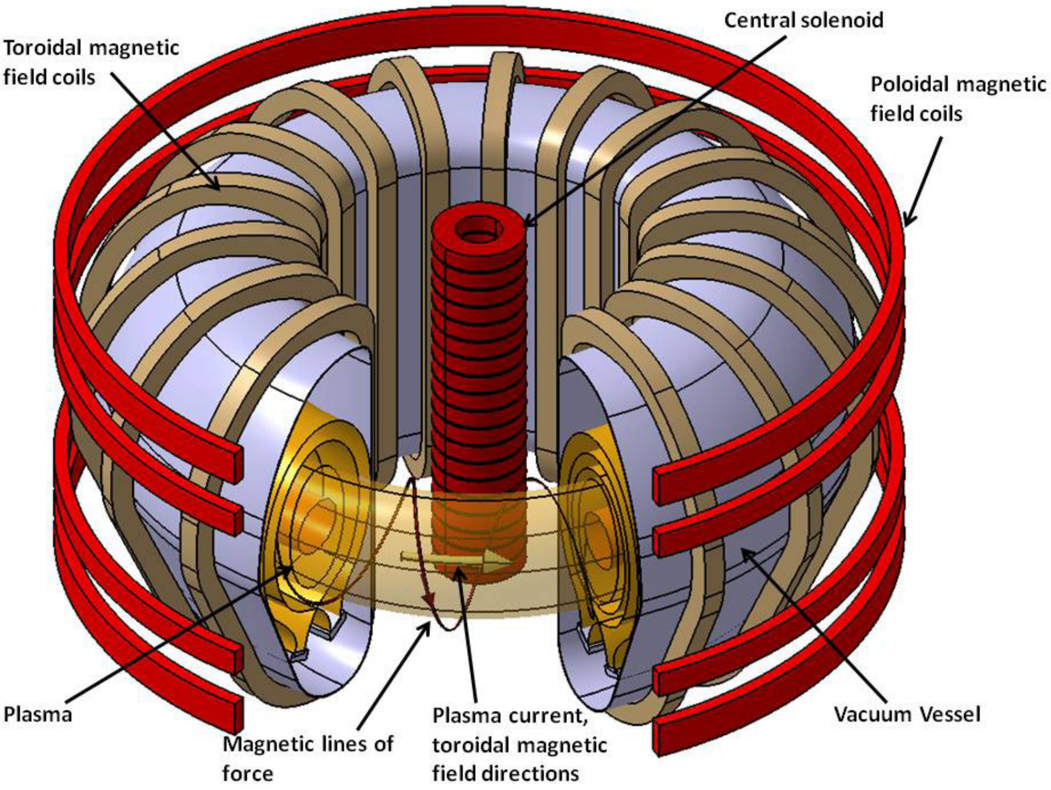

Figure 1.3: Principal scheme of tokamak [3].

$$\dot{R}_R = \frac{E}{B_\phi},$$

i.e. plasma as a whole escapes across magnetic field lines in outward direction.

However, should there be present poloidal magnetic field B_θ of magnitude $B_\theta/B_\phi \sim 10^{-1}$, field lines will be of slightly helical character (see fig. 1.3). In that case, center of particle gyration itself will rotate in poloidal direction with period T. Change of r coordinate (mind coordinate system in fig. 1.2) of center of gyration follows $\dot{R}_r(t) = \dot{R}_Z \cdot \sin(\frac{2\pi}{T}\,t)$. Net effect of drift obtained by integration:

$$\Delta_r = \int_0^T \dot{R}_Z \cdot \sin\left(\frac{2\pi}{T}\,t\right) \mathrm{d}t = 0,$$

which excludes charge separation. In tokamaks, B_θ is generated by plasma current, provided by toroidal electrical field E_ϕ. Integral form of Faraday's law:

$$\oint_l \mathbf{E} \cdot \mathrm{d}\mathbf{l} = -\frac{\partial}{\partial t} \int_{S_l} \mathbf{B} \cdot \mathrm{d}\mathbf{S},$$

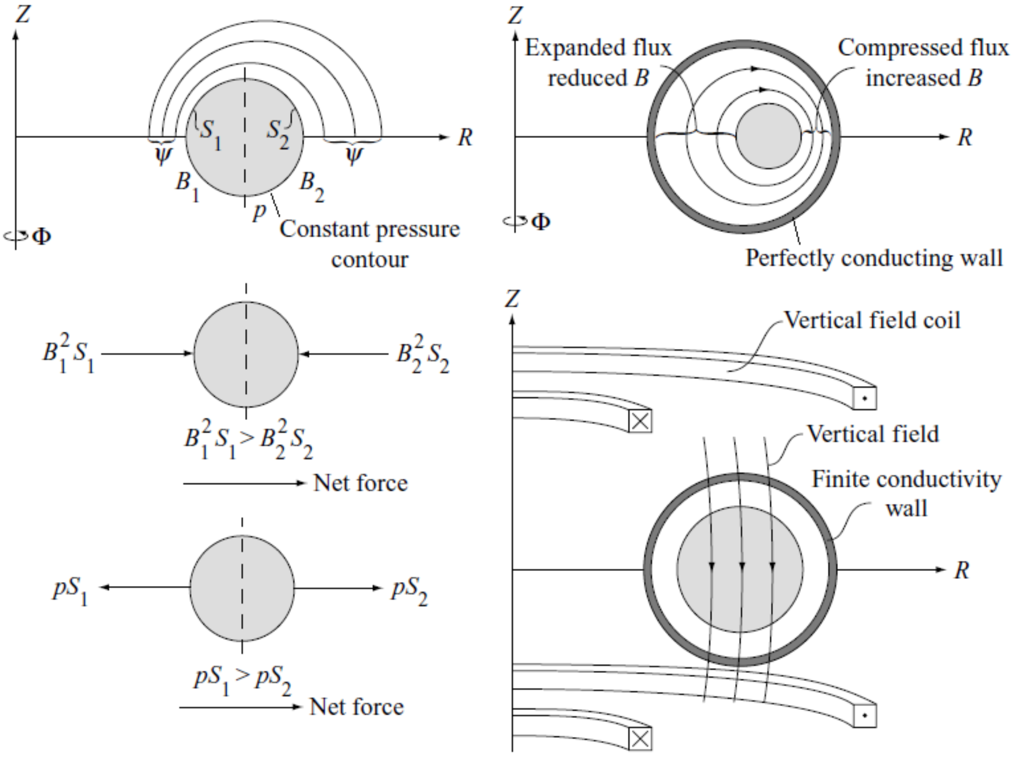

Figure 1.4: Qualitative figure of hoop and pressure forces in tokamak, along with role of conducting wall and B_θ windings [2].

implies that for induction of stationary E_ϕ, linear temporal change of magnetic flux through midplane (i.e. plane of $Z = 0$ coordinate) is necessary. This is provided by long solenoidal coil placed along the major axis of tokamak toroid as shown in fig. 1.3. In older tokamaks, ferromagnetic core is used to lead the magnetic flux perpendicularly to midplane.

However, plasma-generated B_θ is stronger on inner side of torus (B_1 in fig. 1.4) than on its outer side (B_2 therein). By dividing plasma torus surface on inner and outer part (ref. [2]) as in fig. 1.4, two surfaces $S_1 < S_2$ are defined. Magnetic tension force on these surfaces can be estimated as $F_i = \frac{B_i^2 S_i}{2\mu_0}$, with respective directions shown in fig. 1.4. Quadrate of B_i^2 against S_i^1 then determines that net force (refered to as *hoop force*) is pointed outwards from main torus axis.

Since surface of torus represents $p = \text{const}$, another outwards-directed net force arises from $S_1 < S_2$ and $F_i = pS_i$ – see fig. 1.4. This force is referred to as *tire tube force* (ref. [2]).

Were tokamak chamber walls made of perfect conductor, both of these forces would be balanced by eddy currents induced therein due to plasma motion. Since poloidal magnetic flux ψ would not be able to diffuse beyond the walls, resulting significant $\frac{\partial \psi}{\partial R}$ gradient would induce strong B_2 (since $B_Z \sim \frac{\partial \Psi}{\partial R}$) and magnetic tension force would negate hoop and tire tube forces.

Therefore all the tokamaks use conducting chamber walls. Material is naturally of finite conductance, therefore eddy current screening is not perfect and it is necessary to provide part of B_2 by external poloidal field windings – see fig. 1.3 and fig. 1.4. Also, windings of this character are used for plasma shaping and control of its position in manner of Lorentz force density action $\mathbf{f} = \mathbf{j} \times \mathbf{B}$. More detailed and correct analysis of toroidal force balance in general toroidal devices can be found in refs. [2, 1, 6].

1.2 Plasma MHD stability

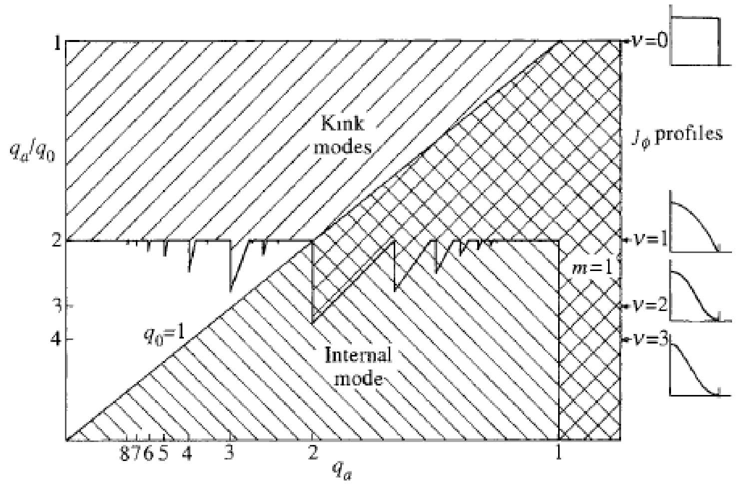

Figure 1.5: An example of ideal MHD stability criteria for tokamak (ref. [1]).

Even uder presence of force balance, another threat for succesfull tokamak operation comes from instabilities due to pressure and current gradients within plasma itself. Stability condition can be expressed as (see ref. [2])

$$\delta W = -\frac{1}{2} \int_V \xi \cdot \mathbf{F} \mathrm{d}V > 0,$$

where ξ represents plasma displacement vector, defined by plasma velocity linear perturbation of $\mathbf{u_1} = \frac{\partial \xi}{\partial t}$ (ref. [5]). For plasma force $\mathbf{F}$, expression:

$$\mathbf{F} = \mathbf{j} \times \mathbf{B} - \nabla p$$

is valid, where $\mathbf{j}$ is plasma current density and p plasma pressure. Ideal magnetohydrodynamics (MHD) assume that plasma resistivity $\eta \to 0$. Therefore, magnetic field equation of [5]:

$$\frac{\partial \mathbf{B}}{\partial t} = \frac{\eta}{\mu} \nabla^2 \mathbf{B} + \nabla \times (\mathbf{u} \times \mathbf{B}) \tag{1.3}$$

takes form:

$$\frac{\partial \mathbf{B}}{\partial t} = \nabla \times (\mathbf{u} \times \mathbf{B}).$$

General ξ can be Fourier-decomposed into harmonic modes $\xi = \xi_r(r) \cdot \exp[\mathrm{i}(m\theta - n\phi - \omega t)]$ and stability of each of these modes can be analyzed individually. For large aspect ratio tokamak (i.e. $R >> a$), literature [1] calculates δW for each of these modes as:

$$\begin{aligned} \partial W = & \frac{\pi^2 B_\phi^2}{\mu_0 R} \int_0^a \left[\left(r \frac{\mathrm{d}\xi_r}{\mathrm{d}r} \right)^2 + (m^2 - 1)\xi_r^2 \right] \left(\frac{n}{m} - \frac{1}{q} \right)^2 r \mathrm{d}r \\ & + \frac{\pi^2 B_\phi^2}{\mu_0 R} \left[\frac{2}{q_a} \left(\frac{n}{m} - \frac{1}{q_a} \right) + (1 + m\lambda) \left(\frac{n}{m} - \frac{1}{q_a} \right)^2 \right] a^2 \xi_a^2, \end{aligned} \tag{1.4}$$

where

$$\lambda = \frac{1 + (a/b)^{2m}}{1 - (a/b)^{2m}} \quad \text{and} \quad q(r) = \frac{r}{R} \frac{B_\phi}{B_\theta} \quad \text{for} \quad r \in (0, a).$$

Quantity of b represents radial coordinate of tokamak wall. If plasma current density is given by

$$j(r) = j_0 \left(1 - \frac{r^2}{a^2} \right)^\nu, \quad \text{where} \quad j_0 = \frac{\nu + 1}{\pi a^2} I_p,$$

and with I_p standing for total plasma current and ν for profile peaking factor, then average B_θ is expressed as:

$$B_\theta(r) = \frac{\mu_0 j_0}{r} \int_0^r \rho \left[1 - \left(\frac{\rho}{a} \right)^2 \right] \mathrm{d}\rho.$$

Thus, *safety factor* q is given by relation:

$$q(r) = \frac{2\pi B_\phi}{R\mu_0 I_p} \frac{r^2}{1-(1-\frac{r^2}{a^2})^{\nu+1}}\,. \tag{1.5}$$

General ξ vector of ideal MHD is provided in ref. [5], or for specific mode of $\xi_r \cdot \exp[\mathrm{i}(m\theta - n\phi - \omega t)]$ in ref. [1]. By substitution of this quantity, and that of q from eq. 1.5 into relation 1.4, stability of specific mode for given plasma parameters can be investigated. Eventual unstable cases are referred to as *kink modes*.

Kink mode stability refers to whole plasma r profile and depends mainly on profile peaking factor of ν – see fig. 1.5. From figure, presence of an additional instability of *internal kink* (mode of $n = 1$, $m = 1$) can be seen as well. Its stability condition is referred to as Kruskal-Shafranov criterion and is in form:

$$q(r) > 1 \quad \text{for} \quad r \in (0, a),$$

$\partial q/\partial r > 0$ character of relation 1.5 makes this mode to depend mainly on parameters of plasma central region, hence the name *internal kink*. Althought criterion itself standardly characterizes cyllindrical configuration (see e.g. [5]), literature [3] presents approximation that enables application to toroidal geometry and refers that observed character of observed internal kinks on tokamaks conform to implications of Kruskal-Shafranov criterion.

Even thought resistivity η is small across for tokamak plasma, on resonant r_s radii of $q(r_s) = m/n$, there is $\mathbf{B} \parallel \mathbf{u}$ and thus diffusive element of relation 1.3 becomes dominant:

$$\frac{\partial \mathbf{B}}{\partial t} = \frac{\eta}{\mu} \nabla^2 \mathbf{B}. \tag{1.6}$$

Plasma behavior on such a resonant surface is subject to resistive MHD. Eq. 1.4 and of ξ from ref. [1] and [5] were obtained by ideal MHD and thus are not relevant for this specific case. Still, $\delta W > 0$ stability condition for resistive MHD can be found in ref. [1]. Respective instabilities, referred to as *tearing modes*, are driven by the same mechanisms as kink modes – i.e. by ∇j and ∇p, and take periodic form of *magnetic islands*. These are generated by B_r perturbation resulting from eq. 1.6, see section 6.1.

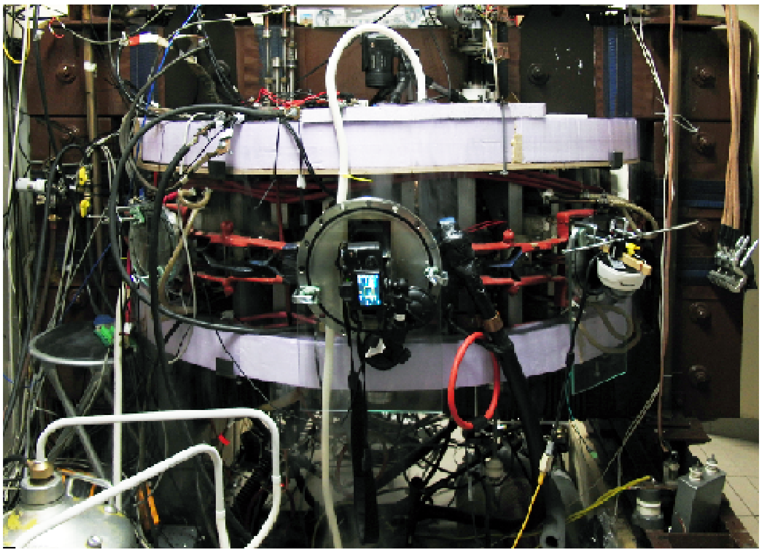

Figure 1.6: Tokamak GOLEM in its current state, including cryostat for high-temperature superconductors (HTS).

1.3 Tokamak GOLEM

Tokamak GOLEM (see fig. 1.6), being one of the longest operating tokamaks, was constructed in Kurchatov Institute in Moscow and operated under name of TM-1-MH until it was transported to IPP CAS in Prague in 1976 [7]. There, it was exploited as tokamak CASTOR to study processes taking place in edge plasma and for investigation of plasma-wave interation. In 2007 was given to Czech Technical University and resultantly moved to Faculty of Nuclear Sciences and Physical Engineering where it was renamed to GOLEM. At the present, its primary designation is for educational purposes within Fusenet Association.

Chamber of this tokamak is of circular cross-section with minor radius of $a_0 = 0.1$ m and major radius of $R_0 = 0.4$ m (ref. [7] and [8]). Plasma region is defined by full circular limiter on $a = 0.085$ m radius, made of molybdenum. The chamber itself is made of bellows stainless steel [7], with port openings covering up to 14% of toroid surface (see ref. [9]). Volume inside is evacuated using turbomolecular pump up to $p \sim 10^{-4}$ Pa, with work gas (H_2 or He_2) being injected to pressures of $p \sim 10^{-3}$ Pa. Outermost wall is represented by 2 cm thick copper coating, on which there are 28 coils of B_ϕ generation installed. For more information on these coils and on their field, refer to section 4.1. For information on external B_θ windings and fields, refer to section 4.2.

As can be seen from fig. 1.6 and even more from scheme in fig. 1.7, there is iron core

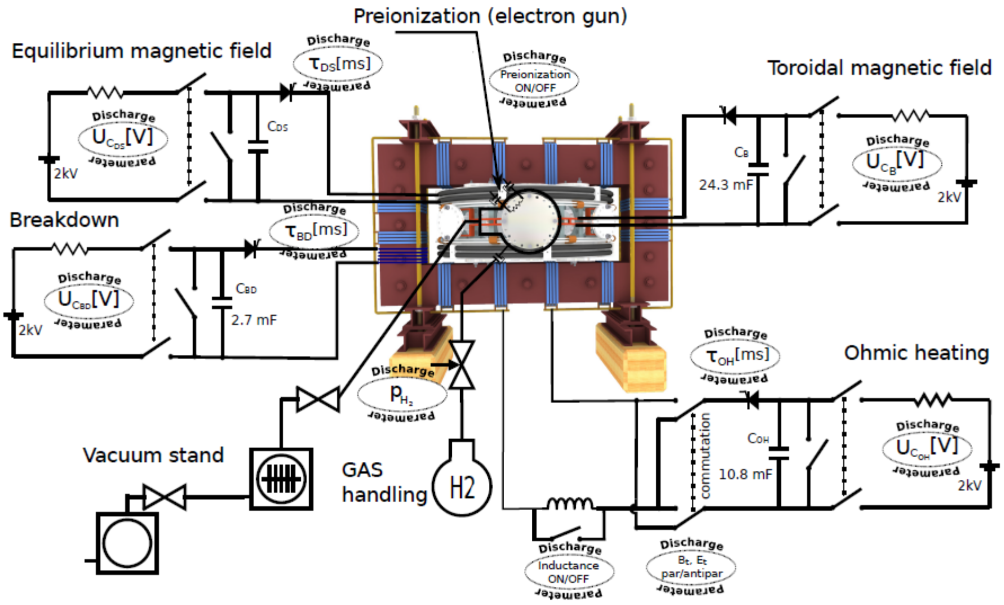

Figure 1.7: Engineering scheme of tokamak GOLEM depicting all the systems of its operation [10].

implemented into plasma current drive system (which is referred to as *ohmic heating*). Implications of this fact are discussed within chapter 4. Scheme also shows that energy to supply tokamak windings is stored in capacitor banks, therefore magnetic fields during discharge take form of single impulses of various time constants. Fig. 1.8 shows typical GOLEM plasma parameters (for explanation of how are these quantities detected, refer to chapter 2). As can be seen, present configuration of capacitor banks can provide $B_\phi \sim 10^{-1}$ T and $I_p \sim 10^0$ kA, which yields typical $q(a) \sim 10^1$. Thus, in order to study MHD structures, different discharge parameters need to be used – see chapter 7.

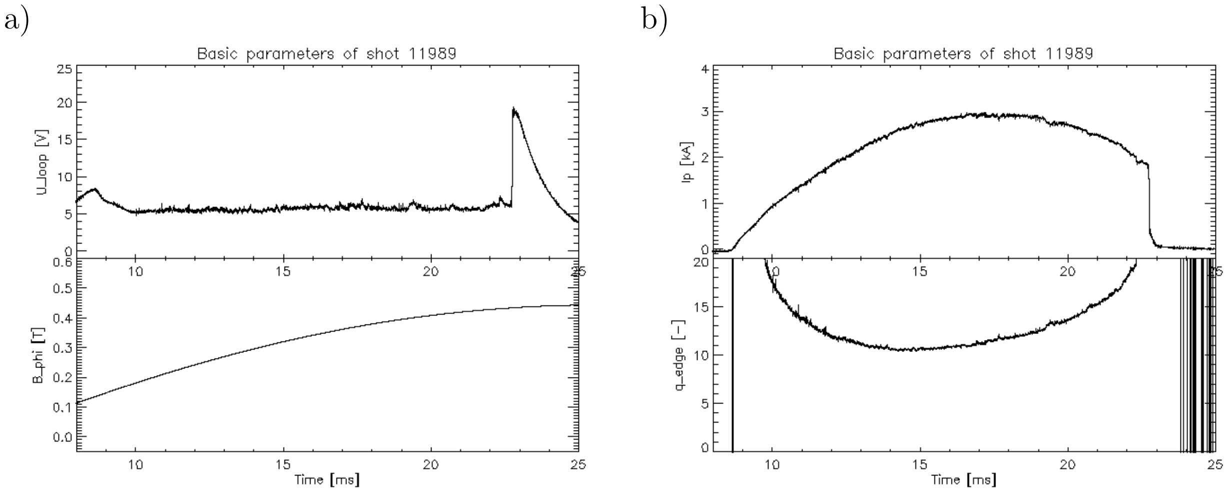

Figure 1.8: Global parameters of typical GOLEM plasma discharge. Figure a) – poloidal loop voltage U_{loop} and B_ϕ toroidal magnetic field. Figure b) – total plasma current I_p and $q(a)$.

Chapter 2

Magnetic Diagnostics on Tokamak GOLEM

2.1 General priniciple of inductive sensors

Sensors of tokamak magnetic field detection are standardly of external and passive character [11]. In principle, measurements are inductive, based on Faraday's law in integral form:

$$\oint_l \mathbf{E} \cdot \mathrm{d}\mathbf{l} = \frac{\partial}{\partial t} \int_{S_l} \mathbf{B} \cdot \mathrm{d}\mathbf{S}. \tag{2.1}$$

Signal detected by probe is represented by left-hand side of the equation:

$$\oint_l \mathbf{E} \cdot \mathrm{d}\mathbf{l} = U_{sig},$$

i.e. by physical quantity of voltage. Since such sensors are easily user-manufacturable, made at low-cost, using widely-available materials [12], they are the most common type of sensors used for measurement of magnetic fields in tokamaks.

Temporal derivation and scalar product on right-hand side of equation 2.1 imply that only rate of change of normale component of **B** to the area of detection loop S_l is measured. Magnitude of this component is obtained from expression:

$$B(t) = \frac{1}{S_l} \int_0^t U_{sig}(\tau) \mathrm{d}\tau.$$

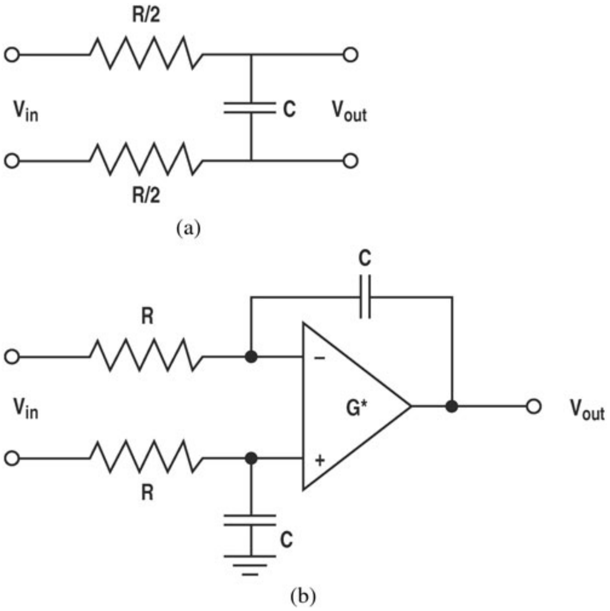

Figure 2.1: Basic passive – fig. a) and active – fig. b) integrating circuit for magnetic diagnostics sensors [11]. V_{in} is equivalent to U_{sig} and V_{out} to U_{out}. G^* represents gain of amplifier G.

2.1.1 Analogue integration methods

Necessity of U_{sig} integration is the main drawback in use of inductive sensors. To obtain quantity $B(t)$ in given time t, U_{sig} needs to be detected for the whole duration of B up to that moment. Additionally, effect of all the errors of U_{sig}, such as DC offset, missing data etc. is accumulated in the integration process. The integration itself can be carried out numerically, or by analogue circuits – see fig. 2.1. Depending on whether amplifier element is used or not, these are recognized as *active* and *passive integrator circuits* respectively.

General $B(t)$ can be Fourier-decomposed into harmonic signals $B_H(\omega, t)$ in following manner:

$$B(t) = \frac{1}{\sqrt{2\pi}} \int \tilde{B}(\omega) \mathrm{e}^{\mathrm{i}\omega t} \mathrm{d}\omega = \frac{1}{\sqrt{2\pi}} \int B_H(\omega, t) \mathrm{d}\omega \tag{2.2}$$

Substitution of harmonic B_H into eq. **??** yields induction of harmonic U^{ω}_{sig}:

$$U^{\omega}_{sig} = -\mathrm{i}\omega S_l B_H.$$

Relation between U^{ω}_{sig} induced by B_H and U^{ω}_{out} registered by data acquisition system can

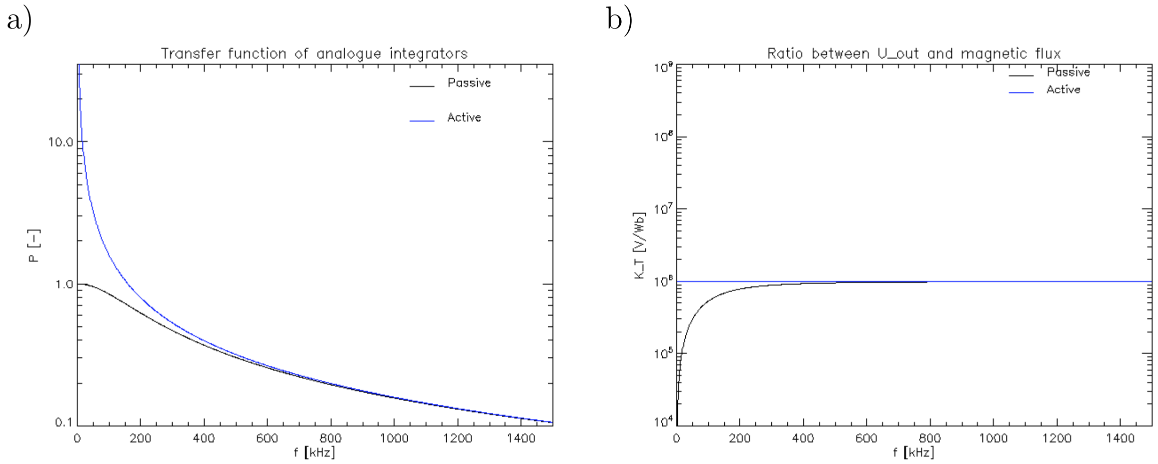

Figure 2.2: $|P(f)|$ and $K_C(f)$ functions for circuits in fig. 2.1, using $C =$ 10 pF, $R = 100\ \Omega$ and $G = 10^5$.

be expressed by *transfer function* $P(\omega) = \frac{U_{out}}{U_{sig}}$, which in principle is complex function. For circuits in fig. 2.1, transfer functions follow (ref. [11]):

$$P_1(\omega) = \frac{1}{1 + \mathrm{i}\omega RC}$$

for passive, and

$$P_2(\omega) = \frac{G}{1 + \mathrm{i}\omega RC(1+G)}$$

for active integration circuit respectively. To characterize signal magnitude transfer, $|P(\omega)|$ function of real domain is sufficient. Relation between magnitude of B_H and U_{out} then is given by:

$$|U_{out}| = \omega |P(\omega)| S_l |B_H| = K_C(\omega) S_l |B_H|.$$

From plotted $|P(\omega)|$ and K_C quntities of both passive and active integration circuits in fig. 2.2 it can be clearly seen that for harmonic $B_H = \text{const} \cdot U_{out}$, hence the name *integration circuit*. Note that real signal transfer from magnetic diagnostics is also significantly influenced by L inductance of detection coil. Refer to section 3.1 for more general analysis. Also, for more information on the subject of signal integration and its specifications, refer to review publications of [11, 12, 13].

2.2 General principle of Hall effect sensors

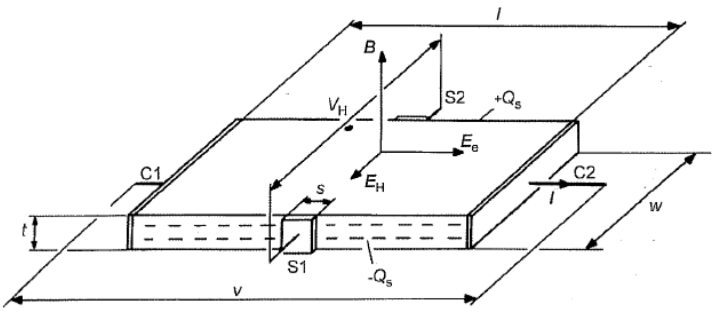

Figure 2.3: Standard form of semiconductor plate used as a Hall effect sensor with principal fields depicted. From ref. [14].

Signal integration issues may be avoided by using methods of measurement, where detected quantity is directly proportional to B. This is characteristic feature of galvanometric Hall effect sensors [11]. By definition (ref. [14]), *Hall effect* is induction of transverse *Hall voltage* due to electromotive force, which emerges in sample due to presence of electric current and perpendicular B component at the same time. Althought Hall effect takes place into some degree in any medium with free charge carriers, it is strongest in doped semiconductors.

Let there be isothermal charge carriers in semiconductor plate in fig. 2.3, represented as continuous media with common velocities, in analogy to MHD approximation in plasma. Voltage drop between ends C1 and C2 induces external electric field $\mathbf{E_e}$ and thus electric current densities of different charge carriers follow

$$\mathbf{J_i} = n_i q_i \mu_i \mathbf{E_e}.$$

Quantity of n_i represents density and μ_i mobility of resp. particles of charge q_i (note that sign of μ_i is the same as the one of q_i). If an external magnetic field B is present in such a system, charge carriers start to drift in direction of $q\mathbf{E_e} \times \mathbf{B}$ product. Upon reaching the respective edge of semiconducting plate, resultant accumulation of charge carriers lead to generation of respective Hall electric field $\mathbf{E_{Hi}}$. This field acts against the initial drift motion, in order to fullfill condition of electromotive force equilibrium. Therefore:

$$\mathbf{E_{Hi}} = -\mu_i \mathbf{E_e} \times \mathbf{B},$$

Since μ_i quantity depends on charge sign, $\mathbf{E_{Hi}}$ field induced by holes is of oposite direction to that of electrons. In the case that one kind of charge carriers is dominant over the other, approximation:

$$\mathbf{E_H} = -\frac{1}{qn}\mathbf{J} \times \mathbf{B} = -R_H\mathbf{J} \times \mathbf{B}$$

becomes relevant. Quantity R_H is referred to as *Hall coefficient.* Note that in the previous relation, the current density $\mathbf{J}$ is still parallel with initial external electric field $\mathbf{E_e}$, althought this is no longer case for total electric field $\mathbf{E} = \mathbf{E_e} + \mathbf{E_H}$. Following geometry in fig. 2.3, V_H is given by expression:

$$V_H = \frac{R_H}{t} IB \tag{2.3}$$

Note, that t represents thickness of the plate (not time). Relation 2.3 yields $V_H = \mathrm{const}\cdot B$. However, it is necessary to provide stable current I, as well as stable temperature conditions due to dependence of semiconductor carrier density on this quantity. I.e. $n = n(T)$ in Hall coefficient $R_H = R_H(n)$. Also, due to this dependence, semiconductor Hall sensors exhibit susceptibility to radiation damage by radiation-induced conductivity (RIC) which, together with low temperature resistance of probe components, is the main challenge in applicability of these sensors to future fusion experiments. Thought, as ref. [11] states, it has been shown that even with current technologies, there are Hall probes available that can withstand ITER-like doses of radiation into sufficient degree. In section 3.4 specifically prototypes of Hall probes which can operate under high temperatures unaffected are presented.

2.3 Global parameter sensors of tokamak GOLEM

2.3.1 Flux loops

Detected flux	N_{turn}	r [m]	Divider
χ	1	0.145	1 : 2

Table 2.1: Parameters of GOLEM χ detection loop. Radius represents r quantity in fig. 1.2.

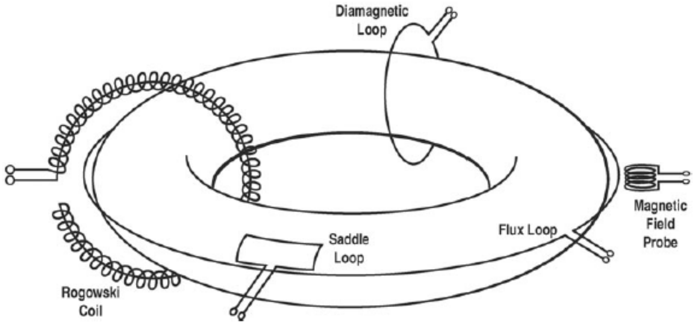

Figure 2.4: Standard geometry of inductive sensors on tokamak devices [11].

Detected flux	N_{turn}	R [m]	Divider
ψ	1	0.57	1 : 5.5

Table 2.2: Parameters of GOLEM ψ detection loop. Radius represents R quantity in fig. 1.2.

Among magnetic diagnostics sensors, flux loops are the most straightforward in implementation. Principally, they consist of only one, resp. several loops, althought voltage divider or integration circuit may be implemented as well. As their name suggests, they are used for detection of average magnetic flux Φ across their effective area S_l, following relation 2.1 in manner:

$$\Phi(t) = \int_{S_l} \mathbf{B} \cdot \mathrm{d}\mathbf{S} = \int_0^t U_{loop}(\tau)\mathrm{d}\tau,$$

where U_{loop} represents voltage detected at the ends of the loop. Relation above also implies that detected Φ is of perpendicular character to detection plane. On tokamaks, poloidal magnetic flux ψ and toroidal magnetic flux χ are detected this way. For measurements of χ across the whole chamber of tokamak GOLEM, there is used a single-loop conductor encircling the tokamak chamber from outside of the copper shell. It has the same design and orientation as diamagnetic loop shown in fig. 2.4. For its technical details, see tab. 2.1.

Measurements of ψ are provided by similar single-loop conductor (see tab. 2.2 for more details), located at the top of tokamak chamber – see fig. 2.4. Such a loop detects both magnetic flux driven through central column of tokamak core and magnetic flux generated by plasma current. For tokamaks, it is standard to use multiple ψ loops

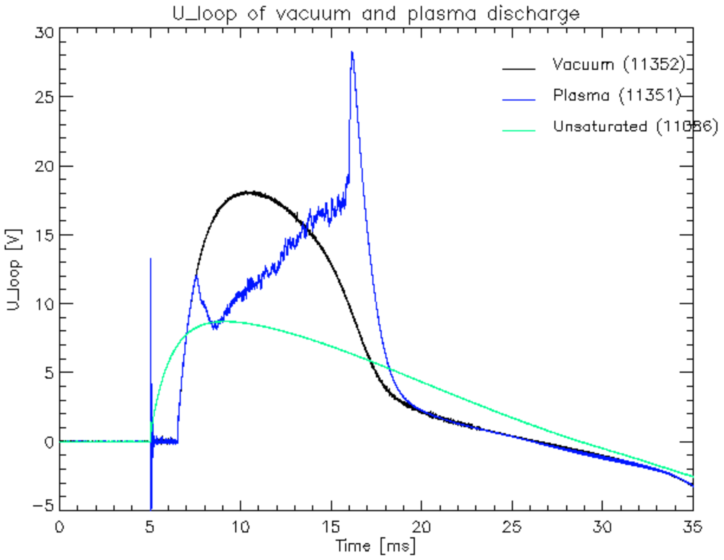

Figure 2.5: Temporal evolution of U_{loop} quantity for vacuum discharge, plasma discharge, both with saturated core at the end of discharge, and vacuum discharge without saturated core as refference.

distributed across poloidal cross-section, in order to obtain spatial distribution of plasma ψ – an important input parameter for plasma equilibrium reconstruction (see ref. [11]). On tokamak GOLEM thought, only single ψ detection loop is used to measure net ψ of plasma and of current drive system across central column. Since these two fluxes are of opposite direction, plasma manifests its existence as drop in U_{loop} at the ends of the detection loop – see fig. 2.5.

Quantity of U_{loop} can be also used for evaluation of total ohmic heating power provided by current drive system P_{CD}, and for calculation of total current in tokamak conducting wall I_{ch} (see ref. [15]):

$$P_{CD} = I_p U_{loop}$$

and

$$I_{ch} = \frac{U_{loop}}{R_{ch}} \tag{2.4}$$

respectively. I_p represents total plasma current (for means of its detection see section 2.3.2) and $R_{ch} = 9.24$ mΩ stands for total chamber resistance. Additionally, physical representation of U_{loop} is that of line-integrated intensity of toroidal electric field:

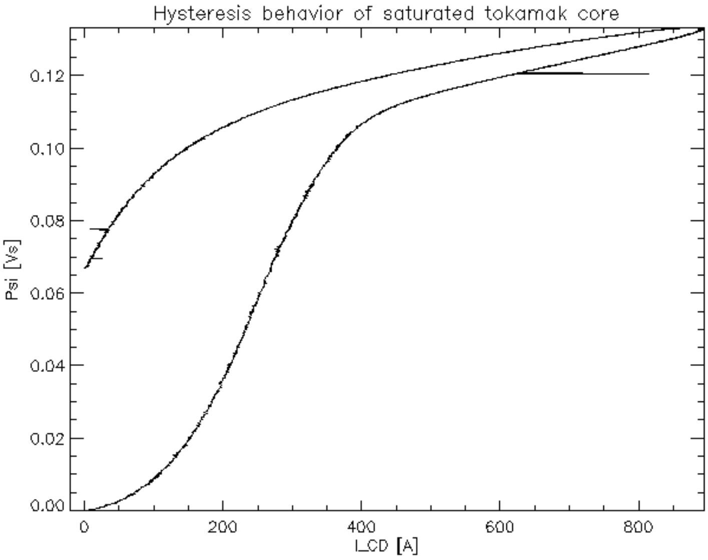

Figure 2.6: Measurement of hysteresis of tokamak GOLEM core for shot 4833. I_{CD} represents current in CD windings.

$$U_{loop} = \oint_l \mathbf{E} \cdot \mathrm{d}\mathbf{l} = 2\pi R E_\phi .$$

See section 4.3 for further implications of this fact.

Another physical quantity that can be extracted from on GOLEM U_{loop} is degree of transformer saturation. Fig. 2.5 also shows two different vacuum discharges, one with core close to saturation at the end of discharge and one that remained on linear part of hysteresis curve for its whole duration. Hysteresis curve of tokamak GOLEM is obtained, when total ψ (i.e. $\int U_{loop} \mathrm{d}t$) dependency on current in CD windings is plotted – see fig. 2.6. For tokamak CASTOR, maximal possible $\psi \approx 0.16$ Vs [9] and it seems that similar, althought a slightly lower limit applies for tokamak GOLEM as well.

2.3.2 Rogowski coil

Lenght [cm]	Diameter [cm]	n [m^{-1}]	$\frac{1}{nS\mu_0}$ [AV^{-1}s^{-1}]
230	0.8	$3 \cdot 10^3$	$5.3 \cdot 10^6$

Table 2.3: Technical parameters of GOLEM Rogowski coil.

Ever since 1912, when its principle of operation was published in [?], Rogowski coil has

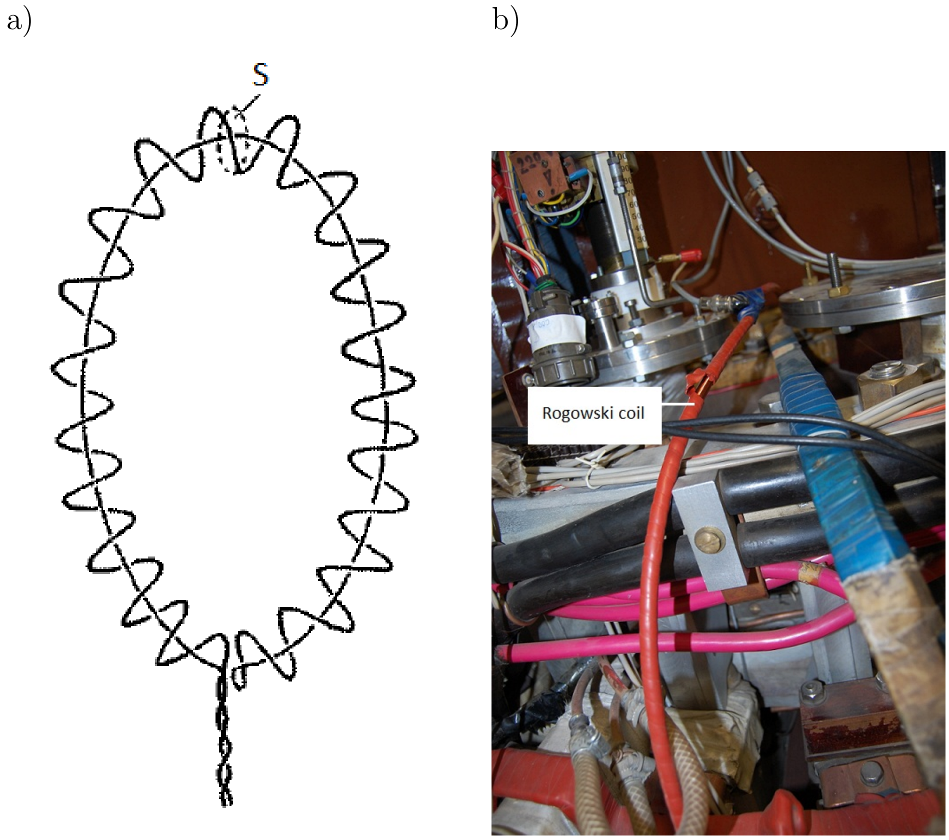

Figure 2.7: Figure a) – principal scheme of Rogowski coil [13]. Figure b) – Rogowski coil used for I_p measurements on tokamak GOLEM.

been widely known as a reliable sensor of high currents [12]. Principally, it is an inductive sensor of magnetic field, thus uses Faraday's law 2.1 to get relation between magnetic flux and detected voltage. Then, application of Ampere's law yields relation between measured magnetic flux and current which generated it. Schematic drawing of Rogowski coil is shown in fig. 2.7 a). Presence of return loop in design of Rogowski coil provides that only poloidal component of Φ is detected. Ref. [12] explains that design of reliable Rogowski coil must use small S area of turns, as well as to have small turn-spacing with as much uniformity as possible. Then (see literature [13]):

$$\Phi = n \oint_l \int_S \mathrm{d}S \; \mathbf{B} \cdot \mathrm{d}\mathbf{l}.$$

Quantity n represents turns per unit lenght, S is area of each turn and l lenght of Rogowski coil. Ampere's law yields:

$$\mu_0 I = \oint_l \mathbf{B} \cdot \mathrm{d}\mathbf{l},$$

which also implies that result does not depend on chosen path (i.e. shape of coil), but only on current encircled by the coil. Together with Faraday's law in form:

$$U_{sig} = \frac{\partial \Phi}{\partial t}$$

this leads to principal relation of Rogowski coil:

$$I = \frac{1}{nS\mu_0} \int_0^t U_{sig}(\tau) \mathrm{d}\tau \tag{2.5}$$

Advantages of Rogowski coil are in its linearity over wide frequency band and pricipal possibility of I measurement of any magnitude. Still, equation 2.5 implies inductive character of the measurement and thus the necessity to integrate U_{sig}.

On tokamaks, Rogowski coils are used for measurements of total plasma current I_p, currents in tokamak coils and currents within conducting structures of tokamak, such as its wall [11]. For tokamak GOLEM, there are several small commercial Rogowski coils with built-in analog integrators that are used for measurements of currents in tokamak windings. To measure I_p, a long rogowski coil poloidally encircles tokamak chamber – see fig. 2.4 and fig. 2.7 b) and tab. 2.3 for its techical parameters. Since this coil envelopes both plasma and tokamak chamber, it in fact detects sum of their currents I_{tot}. Chamber current can be specified from relation 2.4, and thus plasma current temporal evolution is obtained in following manner:

$$I_p(t) = I_{tot}(t) - \frac{U_{loop}(t)}{R_{ch}} = \frac{1}{nS\mu_0} \int_0^t U_{sig}(\tau) \mathrm{d}\tau - \frac{U_{loop}(t)}{R_{ch}},$$

where U_{sig} represents voltage of raw Rogowski coil signal.

2.3.3 Saddle coils

Number of turns	Effective area [cm^2]
8	147

Table 2.4: Technical parameters of GOLEM saddle coil.

In context of magnetic diagnostics, term saddle coil reffers to rectangular, single- or multiple-turn conductor configuration, standardly located on top of tokamak chamber as in fig. 2.4, to detect average vertical poloidal field $\overline{B_Z}$ generated by plasma. This has mainly use in equilibrium reconstruction – saddle coil can complement information from ψ measurements by flux loops and also provide local ψ measurements where a full flux loop can not be instaled [11]. Additionally, saddle coils can be also used to detect nonrotating (or small-frequency) MHD instabilities [11].

On tokamak GOLEM, literature [17] refers that there is a saddle coil for $\overline{B_Z}$ measurements under the copper shell of tokamak. Due to its non-accessible location, it is hard to confirm its status thought. Nevertheless, its principal parameters as steted in [17] are provided in tab. 2.4.

2.3.4 Local magnetic field sensors

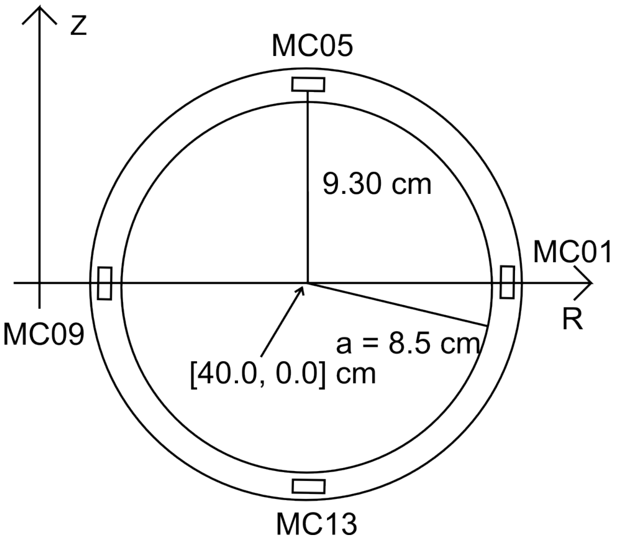

Figure 2.8: Scheme of names and spatial distribution of old Mirnov coils of tokamak GOLEM.

r [cm]	l [cm]	d_1 [cm]	N_1	d_2 [cm]	N_2	d_{wire} [mm]
9.3	3	0.63	46	0.66	45	0.3

Table 2.5: Geometrical parameters of old GOLEM Mirnov probes. r represents radial distance of coils from chamber center, A_{eff} their total effective area, l length of coil core, d_1 diameter of first layer of winding, N_1 number of its turns, d_2 diameter of second layer of winding and N_2 number of its turns.

L [μH]	R [Ω]	A_{eff} [cm^2]
14	1.06	37

Table 2.6: Operational parameters of old GOLEM Mirnov probes. L represents inductance, R resistance and A_{eff} effective coil area (obtained from its geometrical parameters from tab. 2.5).

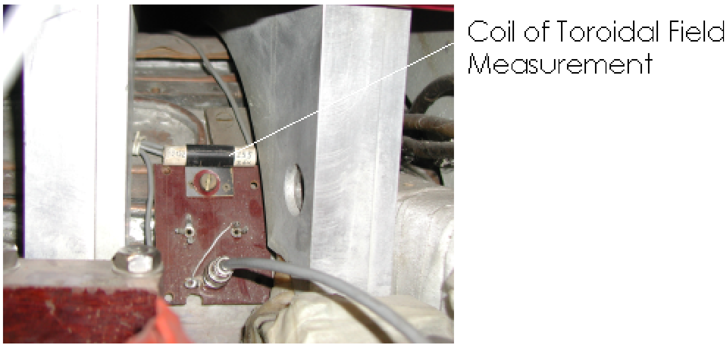

Figure 2.9: Coil for detection of B_ϕ component.

Local magnetic field sensor (see fig. 2.4) refers to single- or multi- layer coil, used for detection of chosen component of local $\mathbf{B}$. These properties arise from $\int_{S_l} \mathbf{B} \cdot \mathrm{d}\mathbf{S}$ term in principal relation 2.1. In-depth analysis of local magnetic field detection coil is provided in section 3.1 in context of design of new local B_θ probes for tokamak GOLEM. In this section, there are described only *old* local B sensors, which include 4 in-vessel Mirnov coils located close to limiter and single ex-vessel coil used for B_ϕ measurements.

Mirnov coils in question are uniformly distributed across poloidal cross-section (see fig. 2.8) to detect B_θ component. Geometrical parameters of these coils are provided in tab. 2.5. As can be seen there, coils are of long cyllindrical shape and made of 0.3 mm thick wire, wound in two layers. The coils themselves are protected from plasma by being put into hollow Al_2O_3 ceramic cyllinder. Electrical and operational parameters of these coils are stated in tab. 2.6 and discussed in chapter 3.

B_ϕ field present in center of tokamak chamber may be obtained in several possible ways. In section 4.1 it is shown that this field follows analytical expression of current in toroidal field winding and therefore measurement of this current would be sufficient. Another way is to use χ flux loop described in section 2.3.1 – simultaneous measurement of toroidal winding current and of total χ, enables to specify A_{eff} quantity of relation:

D [cm]	N	S [cm^2]	A_{eff} [cm^2]
1	255	64	127

Table 2.7: Operational parameters of B_ϕ detection coil. D represents its diameter, N total turn number, S coil effective area given by its geometrical parameters and A_{eff} effective area of coil obtained by calibration for coil to correspond to B_ϕ in center of tokamak chamber.

$$B_{\phi 0} = \frac{1}{A_{eff}} \int_0^t U_\chi(\tau) \mathrm{d}\tau.$$

U_χ refers to voltage detected at the ends of χ detection loop and $B_{\phi 0}$ to value of this quantity in center of tokamak chamber, obtained analytically from current in toroidal winding (see section 4.1). However, the most straightforward method how to measure B_ϕ (which is also the one that is actually used) is to detect U_{sig} of coil in fig. 2.9. Althought location of this coil is arbitrary, thanks to linearity of magnetic fields on winding current, $B_{\phi 1}$ in center of chamber can be obtained by relation:

$$B_{\phi 1}(t) = \frac{1}{A_{eff}} \int_0^t U_{sig}(\tau) \mathrm{d}\tau.$$

However, effective area A_{eff} in above expression is not equal to geometrical parameters of the coil, but it is obtained from condition of $B_{\phi 1} = B_{\phi 0}$, where latter quantity is comes from analytical expression described in section 4.1. For value of A_{eff}, see tab. 2.7.

Chapter 3

New B_θ probes for tokamak GOLEM

As it was covered in previous chapter, magnetic field probe measures local magnitude of component of **B** vector, which is parallel to normale of detection area of the coil A_{eff}, with magnitude averaged across this area. This quantity will be referred to as B, and its relation to voltage induced on probe U_{sig} follows:

$$B(t) = \frac{1}{A_{eff}} \int_0^t U_{sig}(\tau) \mathrm{d}\tau. \tag{3.1}$$

For local measurements, the tendency would be to reduce A_{eff} as much as possible, in order to keep averaging of B to minimum. However, $U_{sig} \sim A_{eff} B$ and thus signal from such a probe would be very low. Sections 3.1.1 and 3.1.2 describe how optimal compromise was found for new local B_θ probes of tokamak GOLEM.

U_{sig} in relation 3.1 is not generally the same as U_{out} detected by data acquisition – in section 2.1.1 it was shown how this is exploited for analogue integration. In section 3.1.3 is signal transmission investigated more generally, including also coil inductance and parasitic effects of transmission line.

Afterwards, close description of new GOLEM Mirnov coils is provided. Section 3.2 describes mechanical manipulator on which the new coils are installed. Implications from section 3.1 and constraints from section 3.2 are then applied in section 3.3 to design new Mirnov coils. Their calibration and transmission properties are referred in this section as well. New experimental Hall probes, intended for implementation into GOLEM are characterized in section 3.4.

3.1 Theory of local magnetic field detection probe

3.1.1 Coil dimension constraints

In-vessel B detectors in tokamaks are genereally constrained by available space, thus general dimensions of coils are standardly chosen as large as possible. Their shape, besides traditional cyllinder also employs rectangular or race-track shape [18]. For tokamak GOLEM thought, the cyllindrical shape was chosen, as this enabled better prediction of coil parameters upon manufacture – see following sections. Additionally, literature [12] refers cyllindrical shape of ratio:

$$\frac{l}{D} = K = 0.866 \tag{3.2}$$

to be optimal for measurements of inhomogeneous fields (provided that coil has small number of thin layers). Quantity D represents diameter of cyllinder and l its length. This relation also implies that coils actually are closer to discs than to cyllinders in their shape.

3.1.2 Coil signal strength constraints

Once again, let $B(t)$ be Fourier-decomposed into its harmonic components B_H by relation 2.2. Each of

$$B_H = B_0 \mathrm{e}^{2\pi \mathrm{i} f t},$$

components induces voltage of magnitude:

$$|U^f_{sig}| = 2\pi f A_{eff} B_0.$$

Let notation $|U^f_{sig}| = U_{sig}$ be used and detection coil to be of cyllindrical shape with diameter D, length l, diameter of wire D_{wire}, having N_l layers with N turns per layer. Also, let the coil be thin, i.e. $N_l D_{wire} << D$. In that case, A_{eff} is calculated in following manner:

$$A_{eff} = N_l \frac{\pi D^2}{4} N = N_l \frac{\pi D^2 l n}{4} = N_l \frac{\pi D^2 l}{4 D_{wire}}.$$

Quantity n represents turns per unit length and it is evident that $n = 1/D_{wire}$. Substitution into relation for U_{sig} yields:

$$U_{sig} = N_l \frac{\pi^2 D^2 l}{2D_{wire}} f B_0. \tag{3.3}$$

It should be also noted here, that quantities D and l are related by constant K from expression 3.2. Therefore, previous relation can be also in form:

$$U_{sig} = N_l \frac{\pi^2 D^3 K}{2D_{wire}} f B_0.$$

Therefore, the best way how to increase output signal of coil is to increase its diameter. Increase in N_l or decrease in D_{wire} may be used as well, but it is less efficient. Relation also implies that if field is of high frequency, smaller coil is sufficient (signal transfer from section 3.1.3 implies that small coil is actually a necessity for such fields). Or vice-versa, large A_{eff} coil needs to be used for detection of small frequency fields – provided that field in question is of small magnitude. E.g. for measurements of slowly varying $\sim 0.1-1$ T B_ϕ fields of large tokamaks, even small coils suffice.

Besides strength of signal, magnitude of white noise is another critical parameter of detector output. Thermal noise on resistive element such as coil follows the widely-known relation (i.e. see ref. [12]):

$$U_{th} = 2\sqrt{k_B T \Delta f R}.$$

Quantity k_B is Boltzmann constant, T temperature, Δf coil bandwidth and R its resistance. To determine level of noise, R and Δf need to be estimated first. If it is not exceptionaly long, resistance of wire leading from coil to data acquisition can be neglected with respect to that of coil. Then, it is straightforward to show that:

$$R = \rho \frac{L}{A} \approx N_l \rho \frac{4Dl}{D_{wire}^3}\,, \tag{3.4}$$

where ρ [Ωm] is resistivity of used wire material, L total length of wire that make the coil and A area of wire base. Δf can be roughly estimated to be equal to resonant frequency of coil-conductor system (for more details on bandwidth see next section), which is:

$$\Delta f \approx \frac{1}{2\pi\sqrt{LC}}\,.$$

Capacity of the system can be safely set to be equal to parasitic capacity of coaxial cable of eventual data acquisition system – $C \approx 100$ pF/m (no integrating circuit is assumed here). As for inductance of coil L:

$$L \approx \mu_0 n^2 V = N_l \mu_0 \frac{\pi D^2 l}{4 D_{wire}^2} .$$

V represents detection volume of coil. Substitution of relations above into principal U_{th} relation yields estimate:

$$U_{th} = \frac{4}{D_{wire}} \sqrt[4]{N_l \frac{k_B^2 T^2 \rho^2 l}{\pi^3 C \mu_0}} . \tag{3.5}$$

This quantity is relevant when compared with signal strength from relation 3.3. Therefore, signal-noise ratio SNR of cyllindrical coil follows relation:

$$SNR = \frac{\sqrt[4]{\pi^{11} C \mu_0}}{8\sqrt{k_B T \rho}} \cdot D^2 l^{3/4} N_l^{3/4} \cdot f B_0. \tag{3.6}$$

At this point, it should by emphasized that assumed noise in the estimation was purely thermal. An interesting remark is that D_{wire} does not have implications SNR. When compared to relation 3.3, it can be seen that D remained dominant with its quadrate and that dependency on N_l and l is slightly lower.

3.1.3 Coil bandwidth constraints

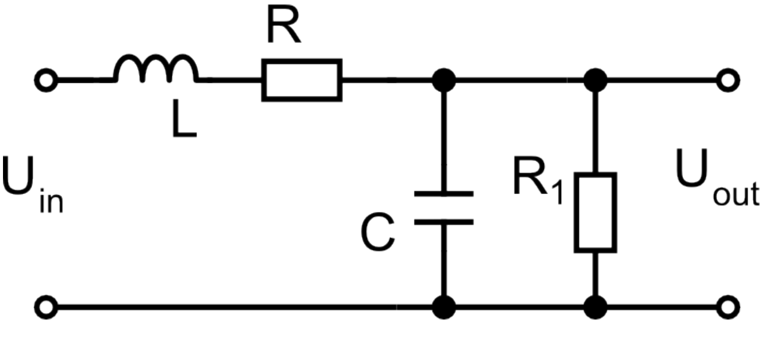

Figure 3.1: Element of real detection circuit. Can represent coil or transmission line. Equivalent to scheme in ref. [19].

Another important constraint on coil parameters is given by desired bandwidth of signal response. Relation 3.3 shows linear dependence of U_{sig} on f. However generally, quantity

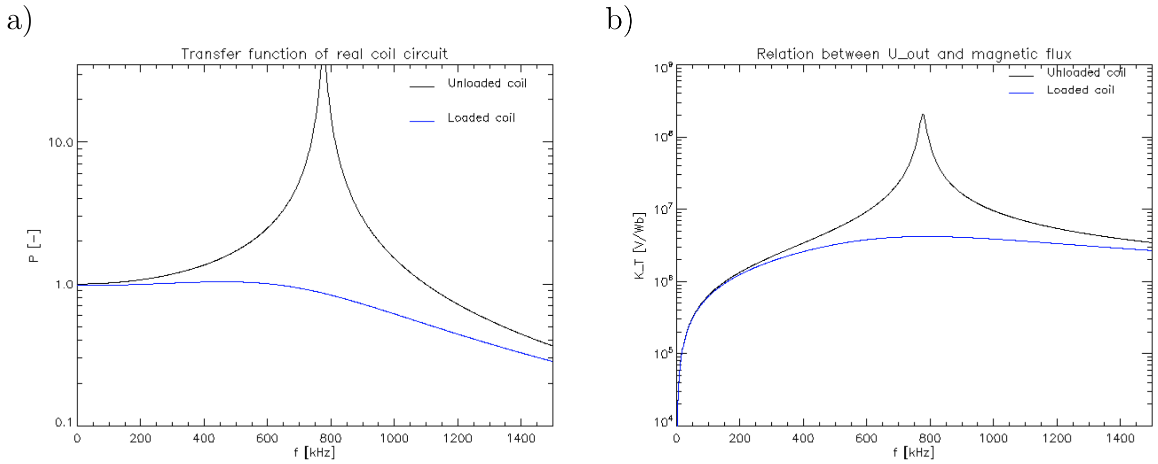

Figure 3.2: Figure a) – transfer function magnitude $|P|$ for parameters of circuit in fig. 3.1 as follows: $L = 140$ μH, $C = 300$ pF, $R = 16$ Ω, and $R_1 \rightarrow \infty$ and $R_1 = 600$ Ω respectively. Figure b) – K_T quantity from relation 3.8 for the same transfer parameters.

registered by data acquisition system $U_{out} \neq U_{sig}$. Ref. [19] proofs that real transfer parameters of magnetic pick-up coil, along with its transmission cable can be represented as a set of circuits shown in fig. 3.1 connected in-series. Coil, transmission line and eventual integrator circuit are characterized by their own inductance L, resistance R, capacity C and conductance $1/R_1$.

For coil, as first element in the series of circuits in fig. 3.1, $U_{in0} = U_{sig}$ and for the rest $U_{in1} = U_{out0}$ etc. naturally. Ref. **??** has investigated by experimental means, that two in-series elements of circuit in fig. 3.1 are sufficient for coil-coaxial cable system. Also, effect of most of the elements is negligible. Ref. [20] shows that typical high-frequency Mirnov coil has parasitic capacity $C_{coil} \approx 30$ pF. However, for coaxial cable $C_{coax} \approx 100$ pF/m, thus it is assumed that $C = C_{coil} + C_{coax} \approx C_{coax}$. I.e. parasitic capacities are merged, ignoring minor correction of fact that they are not on the same node in in-series circuits. Also, literature **??** shows proof that for coaxial cable $L_{coax} = \frac{1}{c^2 C_{coax}} \approx 0.1$ μH. Taking into consideration that $L_{coil} \sim 10 - 100$ μH, once again $L = L_{coil} + L_{coax} \approx L_{coil}$. The same combination goes for R, althought in this case are $R_{coil}/R_{coax} \sim 10^0$ and thus $R = R_{coil} + R_{coax}$. Effect of R_1 is detectable only for coaxial cable, but influence of inherent parasitic element on bandwidth is negligible. However, [12] mentions that often detection circuit ends with low parallel resistance which is being referred to as *load*, thus R_1 will represent this quantity.

To sum-up, series of circuits in fig. 3.1 degenerated into single circuit with $L = L_{coil}$, $C = C_{coax}$, $R = R_{tot}$ and $R_1 = R_{load}$. Straightforward application of Kirchhof's laws will yield transfer function P:

$$P(f) = \frac{U_{out}}{U_{sig}} = \frac{1}{1 + R/R_1 - 4\pi^2 f^2 LC + \mathrm{i}2\pi f(L/R_1 + RC)^2}$$

It was mentioned in section 2.1.1 that P is standardly complex function, which absolute value characterizes magnitude part of transfer and phase characterizes transfer of signal phase. For coil design purposes, only $|P|$ is of interest. Thus:

$$|P(f)| = \frac{1}{\sqrt{(1 + R/R_1 - 4\pi^2 f^2 LC)^2 + 4\pi^2 f^2 (L/R_1 + RC)^2}}\,. \tag{3.7}$$

As can be seen from relation above, ideal transfer properties of $U_{sig} = U_{out}$ can be assumed only if $f << f_{res}$. If no load is present (i.e. $R_1 \to \infty$), then signal resonance takes place at $f_{res} \approx \frac{1}{2\pi\sqrt{LC}}$, yielding $P(f_{res}) \to \infty$. The lower the R_1, the more the resonance is damped, however bandwidth stays the same – see fig. 3.2 a). Relation between detected U_{out} and B_0 of interest thus follows:

$$\frac{|U_{out}|}{A_{eff} B_0} = 2\pi f |P(f)| = K_T(f). \tag{3.8}$$

In fig. 3.2 b) it can be seen that loading element of R_1 flattens K_T and also causes $K_T(f) = \text{const}$ for frequencies around f_{res}. This is referred to as *self-integrating mode* of the coil [12], since magnetic field gets to be directly proportional to output voltage. Direct proportionality of $U_{out} \sim B_0$ due to signal transmission character was also shown in section 2.1.1 for integrating circuits, however in that case, $L = 0$ and $R_1 \to \infty$.

The most relevant quantity for coil design from the analysis above is f_{res}. As can be seen from fig. 3.2 a), signal of higher frequency than f_{res} is significantly mitigated in process of its transmission. Since $f_{res} \approx \frac{1}{2\pi\sqrt{LC}}$, and since most part of C comes from chosen data transmission line (if coaxial cable is used), low L quantity must be chosen for good bandwidth properties of coil. For thin wire coil (see previous section for definition), following relation is valid [21]:

$$L = N_l k \frac{\pi D^2 l}{\pi D_{wire}^2} \quad \text{where} \quad k = 1 - \frac{4D}{3\pi l} + \frac{2D^2}{l^2} - \frac{4D^4}{l^4}\,. \tag{3.9}$$

Therefore, the best bandwidth detectors are those of small coil diameter and thick wire. However, relation 3.3 implies that in such a case the signal might be too low. It is thus evident that an optimal compromise needs to be found for intended B.

3.2 Support mechanical manipulator

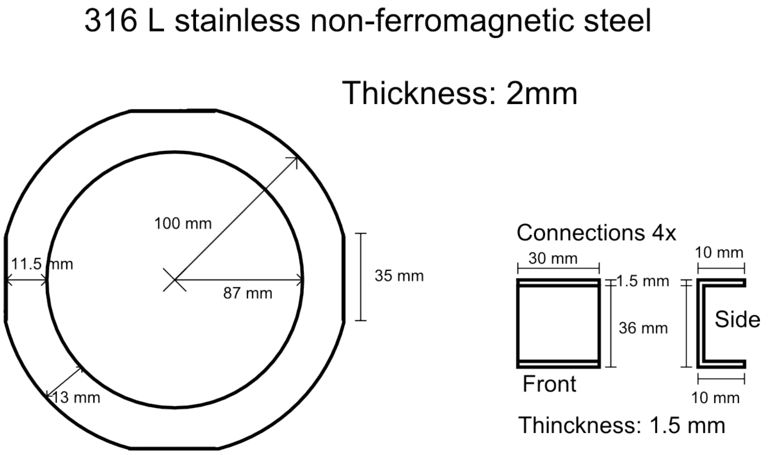

Figure 3.3: Drawing of ring used to hold magnetic field probes, together with parameters of inter-ring connections.

Local magnetic field sensors for tokamaks are standardly installed during the assembly of tokamak itself, not to mention that they tend to be fixed to tokamak wall. To implement newly-constructed B_θ probes for tokamak GOLEM, a large-scale external support structure was used. The main part of the structure is represented by ring shape sheet of 316 L stainless non-ferromagnetic steel (standard material in tokamak engineering), on which the detection sensors are located. To enable the highest possible D of coils, width of the ring was chosen to be as large as possible, while having in mind constraints of $r \in (8.5, 10.0)$ cm imposed by tokamak limiter a and chamber minor radius a_l.

Fig. 3.3 shows resulting parameters of the main ring. Mechanical support onto which it is integrated is shown in fig. 3.4. This external construction was obtained by modification of its previous version (see ref. [?]), which provided better mechanical stabilization of ring position. This was supoosed to prevent possible tremors of the structure during tokamak operation. Since former version of this construction contained two more rings, similar to that in fig. 3.3 , they were re-used and connected to new ring by U-shaped sheets shown in fig. 3.3. This enhanced mechanical stabilization, at the cost of having less space for detectors on the locations where this connection took place, which is on LFS, HFS, TOP and BOT of tokamak chamber.

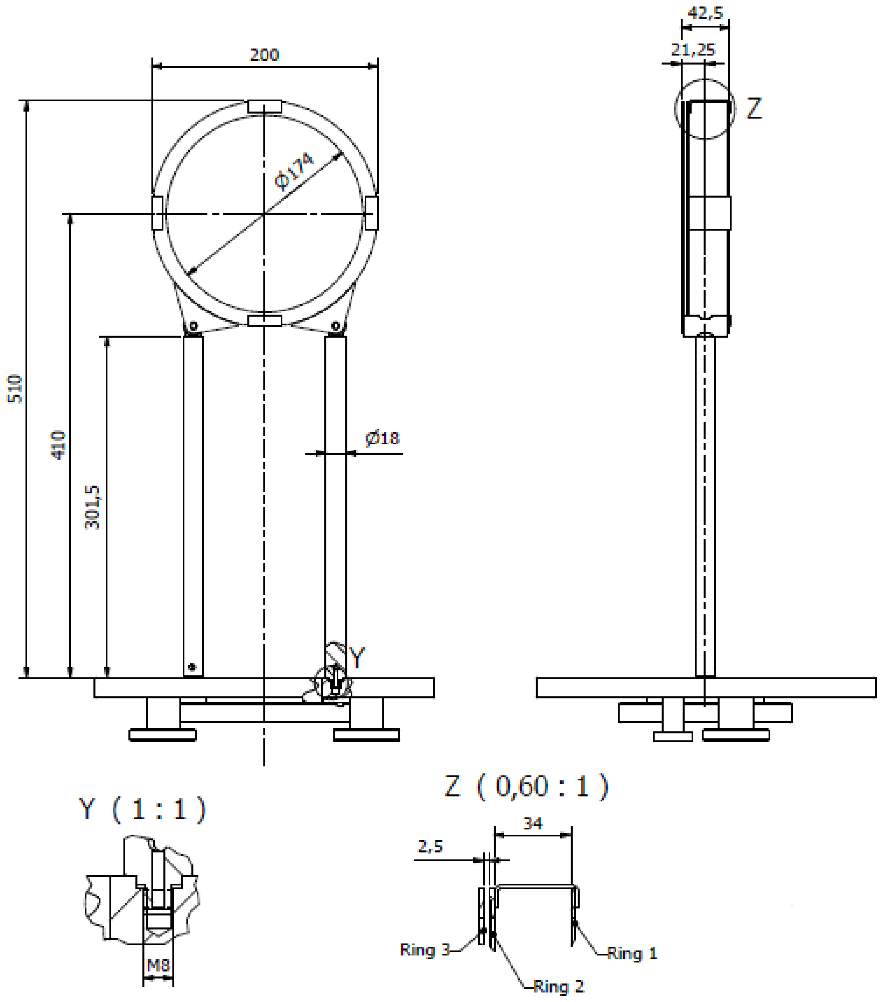

Figure 3.4: Blueprints support structure for the coil ring.

3.3 Array of 16 ring coils

The support ring accomodates 16 local B_θ detectors in total. These are equidistantly distributed along its circumference, facing in $\mathbf{i}_\theta$ direction, as it is shown in fig. 3.5. Fig. 3.3 implies that coils 1, 5, 9 and 13 will need to have reduced dimensions in order to fit on the support. Therefore, there are two types of coils installed on the ring – see fig. 3.6. Material of the cores was chosen to be boron-nitride, due to its relatively easy machining and good thermal properties. Diameter of the cores D was chosen to be the largest possible, while keeping safety margin to prevent direct exposure of coil to plasma. Also, $D/l = 1$ approximation of relation 3.2 is used to keep the core design robust.

Since $U_{sig} \sim D^2$ but $f_{res} \sim \frac{1}{\sqrt{L}} \sim \frac{1}{D}$ (see section 3.1), D of coils was chosen to be

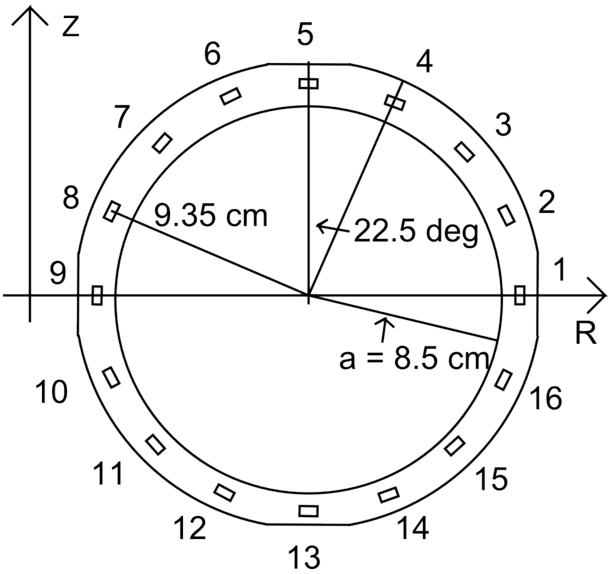

Figure 3.5: Names and spatial distribution of new ring coils across the support.

Type	L [μH]	R [Ω]	A_{eff} [cm^2]	D_{wire} [mm]
1	139.7	13.8	163.4	0.1
2	72.1	8.9	84.5	0.1

Table 3.1: Expected operational parameters of new GOLEM B_θ probes. L represents inductance from relation 3.9, R resistance from expression 3.4 and A_{eff} effective coil area calculated using parameters in blueprints in fig. 3.6.

as large as possible. The trade-out between bandwidth and signal strength of coil was decided by choice of N_l and D_{wire}. Two different $D_{wire1} = 0.3$ mm and $D_{wire2} = 0.1$ mm were available. Because wires of coils need to form twisted pair – to prevent accidental formation of additional loops on transmission line, N_l must be an even number. For 0.3 mm wire in diameter, only $N_{l1} = 2$ will fit to coil. Also, since for 0.1 mm thick wire $N_{l2} = 4$ yields for type 1 coil $L = 250$ μH using relation 3.9, i.e. $f_{res} \approx 450$ kHz for $C_{par} = 500$ pF (i.e. 5 m long coaxial cable). Since intended $f_{nyquist} = 500$ kHz, it was decided that $N_{l2} = 2$ in the case that high-frequency measurements would be needed in future. Thus, from the bandwidth point of view – as long as $N_l = 2$, both $D_{wire1} = 0.3$ mm and $D_{wire2} = 0.1$ mm are satisfactory. From the perspective of SNR, i.e. from relation 3.6, it seems that any D_{wire} will yield the same properties.

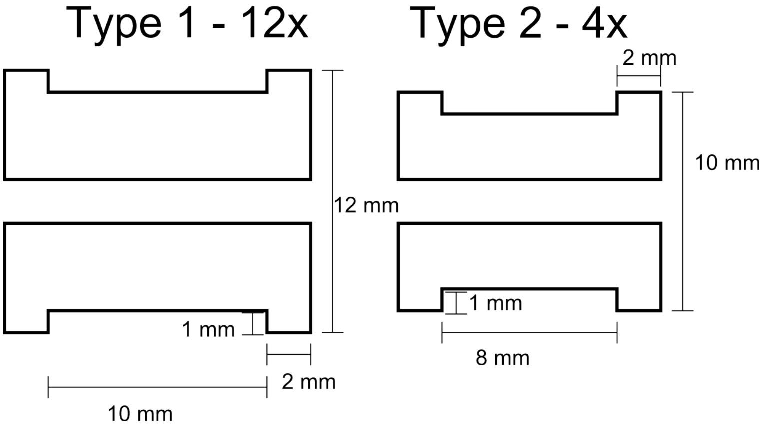

Figure 3.6: Blueprints of cores of ring coils – side cut of hollow cyllinders. Type 2 coils are number 1,5,9 and 13, type 1 coils are all the others.

Comparison SNR_{old} of old Mirnov coil design in tab. 2.5, SNR_1 and SNR_2 respectively for types given by geometrical parameters in fig. 3.6, yields:

$$\frac{SNR_1}{SNR_{old}} = 1.22,$$

$$\frac{SNR_2}{SNR_{old}} = 0.66.$$

However, detected noise voltage of 0.5 mV on old Mirnov coils does not correspond to thermal noise level expected (if connected to 3 m coaxial cable) from relation 3.5 – $U_{th} \approx 2 \cdot 10^{-4}$ mV. This discrepancy implies that relation 3.6 might be not the optimal for characterization of coil signal properties. Since noise seems to be of fixed external character, effective area of coil is the more relevant parameter. Then, expression 3.3 implies that wire of smallest possible D_{wire} is optimal.

Thus, found trade-off between signal strength and bandwidth implies $N_l = 2$ and $D_{wire} = 0.1$ mm for both type of coils. If such coils are connected to coaxial cable of ≈ 3 m lenght, characteristics shown in tab. 3.1 and fig. 3.8 apply. As can be seen, both types of coils are explected to have better signal parameters than old design of coil, while keeping good signal transfer up till $f_{nyquist}$ of intended data acquisition. Photo of resulting probes, installed on the mechanical support can be seen in fig. 3.7.

Althought parametes of R, L and A_{eff} can be calculated from geometrical parameters of coil and its wire (see tab. 3.1), deviations during process of individual coil manufacture and due to approximations in analytical expressions require direct measurement of these

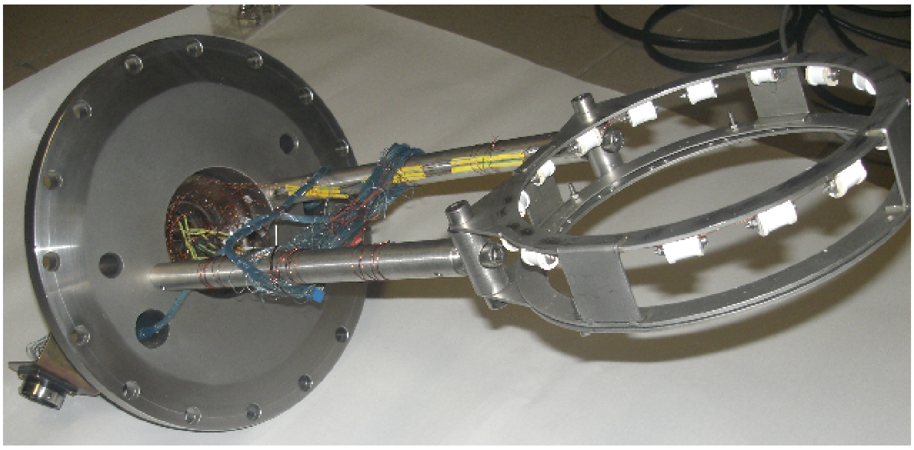

Figure 3.7: Assembled array of ring coils on modified mechanical manipulator.

parameters for each individual coil.

A_{eff} is obtained from calibration of coil in known magnetic field. The optimal way how to generate an appropriate B for this, is to use Helmholtz coils, since they manifest good homogenity of generated field in their centre [23]. However, since inductive sensors react only to change of magnetic field:

$$|U_{sig}| = 2\pi f A_{eff} B_0,$$

current in Helmholtz coils needs to be of AC character for calibration of such sensors. This is of no trivial matter for Helmholtz coils, since they tend to have large L and thus might be close to resonance part of current transmission curve even for low frequencies. Due to this, their current becomes function of frequency $I = I(f)$, leading to $B = B(f)$. However, only $B = B(0)$ for DC current is usually known for these coils.

Whether or not are Helmholtz coils close to resonance for given f can be seen from phase difference between input current I_{in} and U_{sig} from calibrated coil. U_{sig} is phase-shifted with respect to B by $\pi/2$ and at the same time, B has the same phase as I_{out} current transferred through circuit of Helmholtz coils. This circuit is of the same character as that in fig. 3.1. If f is far from f_{res}, then $I_{in}/I_{out} = 1$ both in meaning of magnitude and phase. In that case, phase shift between U_{sig} on calibrated coil and I_{in} on feed cables of Helmholtz coils is equal to $\pi/2$. This needs to be confirmed by oscilloscope before the calibration takes place.

In the process of calibration of 16 Mirnov coils, power for B generation was supplied

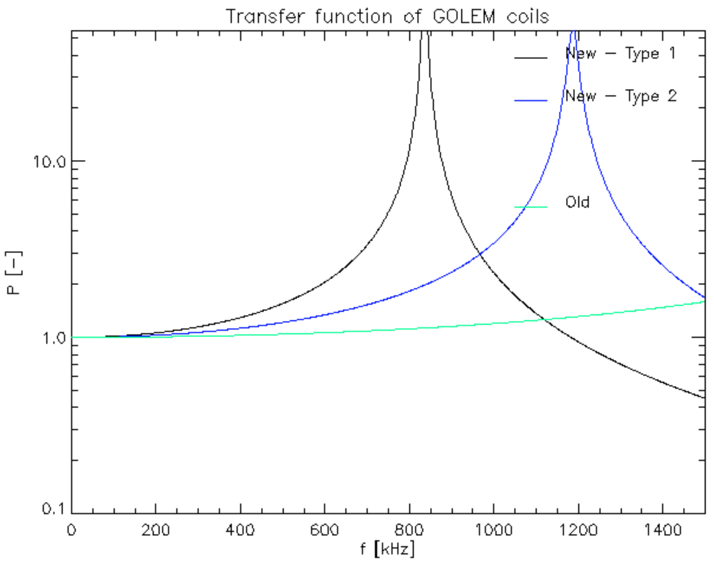

Figure 3.8: Comparison $|P(f)|$ functions of GOLEM local B_θ probes without load, using for 3 m long coaxial cable.

by harmonic grid current of $f = 50$ Hz. Before it was sent to Helmholtz coils, it went through regulation transformer, which enabled to adjust magnitude of I_{in}. This quantity was directly measured by CLS-25 closed loop Hall effect current sensor of $K_1 = 3.32$ A/V sensitivity. Used Helmholtz coils provided $K_2 = 53 \cdot 10^{-4}$ T/A for DC current. Therefore, by measurement of amplitude of harmonic U_{sig} of coil and amplitude of voltage U_{in} on current detector, A_{eff} is obtained from relation:

$$A_{eff} = \frac{1}{2\pi f K_1 K_2} \frac{U_{sig}}{U_{in}} = K \frac{U_{sig}}{U_{in}} . \tag{3.10}$$

As for coil-cable R and L quantities, these have been measured directly, using digital LCR meter ELC-3131D. Results of calibration, i.e. A_{eff}, L of coils and R of coil-cable system, as well as number of turns of each coil layer can be seen in tab. 3.2. In the table, there is also quantity of polarity, which represents whether U_{out} is of positive or negative character for positive B_θ of tokamak plasma (see section 5.1). By comparison of tab. 3.1 to tab. 3.2, it can be seen that real coil parameters are relatively close to their expected values. R is offset by 3 Ω, which is from most part because of data acquisition cable. Difference in A_{eff} arises from coil having less turns than it would be allowed from its geometrical parameters, which is due to imperfect coil manufacture. However, if number of turns for specific coil (see tab. 3.2) is used tp obtain A_{eff}, then e.g. for coil 1 the difference is $A_{eff} - A_{model} = -0.06$ cm^2, instead of -15.6 implied by comparison of

Name	A_{eff} [cm^2]	L [μH]	R [Ω]	Polarity [-]	N_1 [-]	N_2 [-]
1	68.9	88.5	12.1	-1	66	66
2	140.7	176.3	15.6	-1	80	80
3	138.9	180.4	16.6	+1	83	85
4	140.4	186.3	17.3	+1	81	81
5	68.6	86.5	12.5	-1	65	65
6	134.5	173.6	15.8	+1	80	79
7	134.3	165.2	16.2	-1	77	76
8	142.5	191.5	17.6	+1	83	82
9	67.6	86.2	12.2	-1	66	65
10	142.8	187.5	16.7	+1	83	83
11	140.4	187.8	17.4	-1	82	81
12	138.0	172.2	15.7	-1	79	79
13	76.3	88.0	12.3	-1	61	61
14	142.2	185.6	17.1	-1	81	80
15	139.8	184.9	16.4	-1	83	82
16	139.3	172.8	16.1	-1	79	79

Table 3.2: Parameters of coils in fig. 3.5. Coils 1,5,9 and 13 are of design no. 2 in fig. 3.6, the rest is of design no. 1. A_{eff}, R, L and specified experimentally. N_1 represents number of turns in first layer, N_2 turns of second layer.

aforementioned tables.

3.4 High-temperature resistant Hall probes

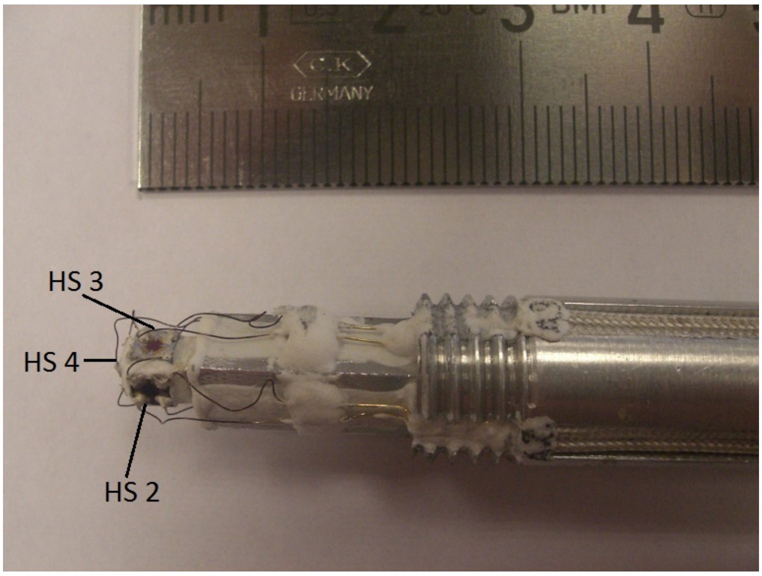

Figure 3.9: Probe head with high-temperature Hall sensors in 3D orthogonal configuration.

The Hall sensors received from Poznan University of Technology (see fig. 3.9) are in principle standard semiconductor-based Hall plates subjected to Hall effect, as it is described in section 2.2 – i.e. they measure B quantity in manner:

$$B = K\frac{U_{hall}}{I}\,. \tag{3.11}$$

In relation above, U_{hall} represents Hall voltage and I supply current. Just as new Mirnov coils, these probes are intended for implementation on diagnostic ring – specifically to be installed on U-shaped connections of rings (see fig. 3.3). However their current form (see fig. 3.9) still requires some additional mechanical modifications before this can happen. Fig. 3.9 shows that there are 3 elements in 3D orthogonal configuration, for simultaneous measurement of all the components of $\mathbf{B}$ vector. There are two such probe heads i.e. 6 Hall elements in total, whose principal parameters have been measured upon their manufacture in Poznan University of Technology see tab. 3.3. K represents sensitivity from relation 3.11 and generally is a function of temperature T and of radiation damage. $R = U_{in}/I$, where U_{in} is voltage drop for driving current. U_{off} is Hall probe offset, equal to detected Hall voltage for $B = 0$ field. Hall voltage is thus obtained from expression:

Detector	R [Ω]	K [TA/V]	U_{off} [mV]
HS A2	7.6	0.627	3.79
HS A3	7.4	0.630	2.30
HS A4	7.3	0.646	6.60
HS C2	8.5	0.534	6.94
HS C3	8.3	0.556	1.95
HS C4	8.3	0.547	5.08

Table 3.3: Basic Hall probe parameters, as provided by Poznan University. Notation of detectors can be seen in fig. 3.9. Calibration took place at room temperature, using DC field of $B = 0.133$ T and $I = 40$ mA. K represents sensitivity and U_{off} offset voltage at given conditions.

$$U_{hall} = U_{sig} - U_{off},$$

where U_{sig} stands for detected transverse voltage.

An unique trait of these specific sensors is, that they are supposed to keep their properties and withstand high temperatures, which would make them relevant for measurements of steady-state magnetic fields on future fusion reactors. Therefore, an investigation of their T resistance was carried out. The sensors of C-probe were subjected to known pulsed DC magnetic field generated by thick Helmholtz coils (see ref. [23]), while being placed into Venticell oven. Pulsed character of calibrating field enabled to measure U_{off}, which is necessary to obtain sensitivity K. Driving current was stabilized to $I = 10$ mA and $B \approx 25$ mT. Temperature of Helmholtz coil-probe head system was increased and decreased several times and measured by thermocouple located on the probe head. The results of temperature dependency of K and U_{off} measurements can be seen in fig. 3.10.

From plots in fig. 3.10 it is evident, that probe operational quantities are invariant on applied temperature. This is a non-trivial observation, since not many industrial-issue Hall probes can survive such temperatures, yet alone to maintain K and U_{off}. By calibration, $K_{C4} = 0.547$ [AT/V] at room temperature was obtained as well, which corresponds well to value in tab. 3.3. For other probes, $K_{C2} = 0.508$ [AT/V] and $K_{C3} = 0.520$ [AT/V], which is slightly different from the values in tab. 3.3. However, during measurement of these two quantities, it was not possible to properly place the probe into the center of Helmholtz coils, thus systematic error might be present in result.

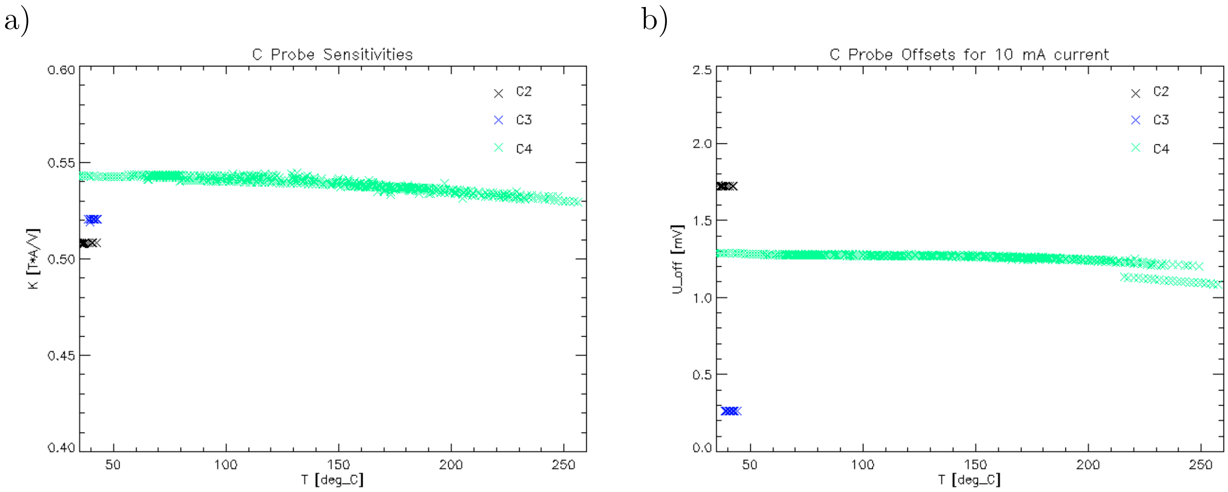

Figure 3.10: Figure a) – temperature dependence of Hall element sensitivities. Figure b) – temperature dependence of Hall voltage offset for 10 mA current.

It can be seen from fig. 3.10, that a small drop in U_{off} takes place at highest temperatures. Still, this is of minor concern – it was shown that this has no influence on K whatsoever. Total resistance of all the 3 sensors combined yields $R_{tot} = 23.34$ [Ω], once again in good correspondence to tab. 3.3, where $R_{tot} = 25.1$ [Ω]. Future plans with these sensors include their implementation onto the diagnostic ring in order to test their performance in real tokamak environment.

Chapter 4

Tokamak GOLEM magnetic fields

Fields described in this chapter are those of tokamak GOLEM windings and include specifically toroidal magnetic field B_ϕ (section 4.1), poloidal magnetic field $\mathbf{B}_\theta = (B_R, B_Z)$ (section 4.2) and stray fields induced either by chamber current or by current drive windings upon transformer saturation (section 4.3). This chapter provides analytical expressions on how to calculate these fields and compares their output to that of numerical models and measurements.

4.1 Toroidal magnetic field of tokamak GOLEM

The most common model of tokamak toroidal field uses straightforward implementation of Ampere's law. This yields:

$$B_\phi(R) = N_c N_t \frac{\mu_0 I_c}{2\pi R} \sim \frac{1}{R}\,. \tag{4.1}$$

with N_c being number of coils ($N_c = 28$ for GOLEM), N_t their turn number ($N_t = 8$ for GOLEM), I_c current per turn and $R \in (R_0 - R_c, R_0 + R_c)$. $1/R$ dependency is obtained from integral properties and analogy of system in fig. 4.1 a) to infinitely long conductor. This may work for small aspect ratio and D-shaped tokamaks, but for GOLEM coils – see fig. 4.1 b), it might be different. To investigate this further, profile of B_ϕ in GOLEM was calculated using 3D model based on Biot-Savart's law and known configuration of windings.

Use of Biot-Savart's law is optimal way how to calculate magnetic field from fixed

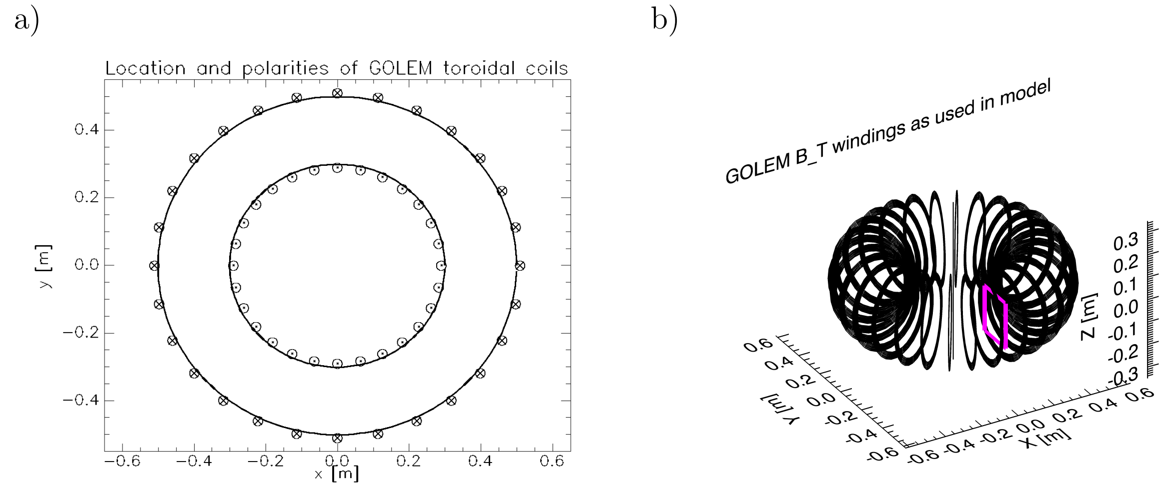

Figure 4.1: Topology of toroidal field coils of tokamak GOLEM. a) mid-plane cut as seen from above, with winding polarities. b) 3D geometry. Location of plane of measurements and model calculations shown as purple square. Note the high density of B_ϕ windings.

conductor of known location and current in 3D geometry. The law has vector form:

$$\mathbf{B} = \frac{\mu_0 I_c}{4\pi} \oint_{\mathbf{l}} \frac{\mathrm{d}\mathbf{l} \times \mathbf{R}}{|\mathbf{R}|^3}, \tag{4.2}$$

where $\mathbf{R} = \mathbf{r}_{calc} - \mathbf{r}_{dl}$, with $\mathbf{r}_{calc}$ being location modelled point in space and $\mathbf{r}_{dl}$ location of element of conductor contour $\mathbf{l}$. I_c represents current per turn of winding. Let it be defined $\mathbf{r}_{calc} = (x_0, y_0, z_0)$. If $x_0 = 0$, then $B_\phi = B_x$. In that case, by using notation in fig. 1.2, dividing poloidal angle θ into $N_i \sim 10^2$ elements and defining a_k as radius of k-th turn of coil and toroidal angle of location of this coil as ϕ_j, then for $B_\phi = B_\phi(0, y_0, z_0)$ follows numerical relation:

$$B_\phi = \frac{\mu_0 I_c}{4\pi} \sum_{i,j,k}^{N_i,N_j,N_k} \frac{2\pi a_k (a_k \sin\theta_i - z_0)\sin\theta_i \cos\phi_j + [(R_0 + a_k\cos\theta_i)\cos\phi_j - y_0]\cos\theta_i}{N_i\left[(R_0 + a_k\cos\theta_i)^2 \sin\phi_j + (y_0 - (R_0 + a_k\cos\theta_i)\cos\phi_j)^2 + (z_0 - a_k\sin\theta_i)^2\right]^{1.5}}. \tag{4.3}$$

Parameters of $N_k = 8$ and $N_j = 28$ are fixed, given by number of turns per coil and by total number of coils respectively. $\phi_j = 2\pi\frac{j}{N_j} + \phi_0$ equidistantly divides toroidal angle ϕ and represents location of coils. By setting its initial value $\phi_0 = 2\pi\frac{0.5}{N_j}$, modelled plane will be located in inter-coil region (see fig. 4.1), while $\phi_0 = 0$ represents plane located under the B_ϕ coil. Comparison of results for different ϕ_0 enables investigate B_ϕ ripple. Coil radii a_k are span equidistantly on $a_k \in (0.1670, 0.1704)$ m.

4.1.1 Comparison of B_T models to each other and to measurements

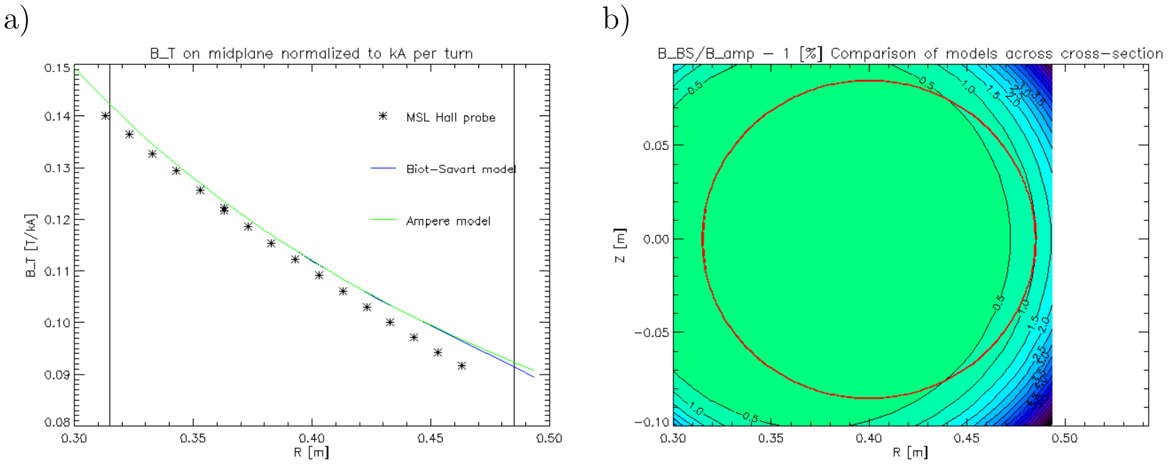

Figure 4.2: Figure. a) – B_ϕ comparison of model in eq. 4.1 ($B_{\phi 1}$), model in eq. 4.3 ($B_{\phi 2}$) and measurements by MSL Hall probe on miplane. Black lines represent limiter. Figure b) – $\frac{B_{\phi 2}}{B_{\phi 1}} - 1$ quantity across plasma region (inside red line). Note negative magnitude of values.

Besides numerical calculations using Ampere's law in relation 4.1 and Biot-Savarat's law in relation 4.3, direct measurements of B_ϕ quantity on midplane took place as well. MSL Hall probe (ref. [23]) was inserted into open chamber of tokamak via large diagnostic port. Scan of $B_\phi(R)$ was obtained by making discharge into B_ϕ winding for every R location of probe, while I_c current per turn of winding was detected. R profile of measured and modelled $\frac{\max(B_\phi)}{\max(I_c)}$ is shown in fig. 4.2 a). It can be seen that both models are practically undistinguishable from each other. Moreover, across the whole plasma region, difference between both calculations stays below 1 %, as can be seen from fig. 4.2 b). Nevertheless, measurements by MSL Hall probe in fig. 4.2 a) imply that B_ϕ might be in fact lower. However, even thought precision of the probe itself is $\approx 1\%$ (ref. [23]), accuracy of its R location cannot be guaranteed into such degree. Due to probe being installed on > 1 m long steel rod, R systematic error could be imposed by rod deformation and thus model

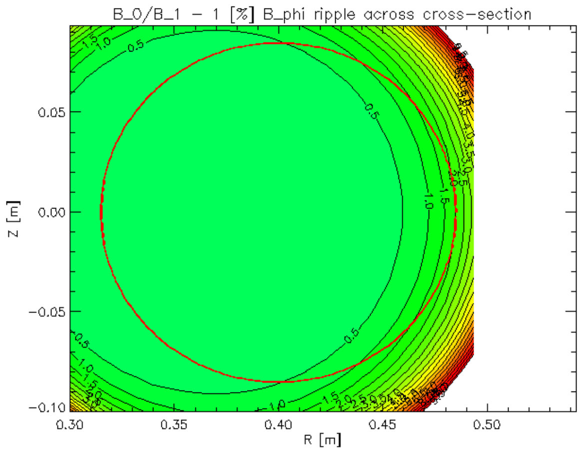

Figure 4.3: Toroidal field ripple of tokamak GOLEM as given by model in relation 4.3. B_0 represents B_ϕ of $\phi_0 = 0 \cdot 2\pi/N_k$ and B_1 stands for B_ϕ of $\phi_0 = 1 \cdot 2\pi/N_k$. Quantity of $B_1/B_0 - 1$ is plotted.

predictions might as well fall within x-error bar uncertainty. The difference in $\nabla B_\phi(R)$ observed on LFS might be due to fact that around large port opening, neighboring B_ϕ coils are separated from each other by more than $2\pi/N_k$ angle.

Even thought fig. 4.2 shows that Ampere's law model is sufficient for B_ϕ characterization, relation 4.3 is necessary to model B_ϕ ripple. Fig. 4.3 represents $B_0/B_1 - 1$ quantity, where B_0 represents B_ϕ of $\phi_0 = 0 \cdot 2\pi/N_k$ and B_1 stands for B_ϕ of $\phi_0 = 1 \cdot 2\pi/N_k$. As can be seen, maximal difference in plasma region is below 2%, thus ripple on tokamak GOLEM is negligible. This is of no surprise, since as can be seen in fig. 4.1, this tokamak has unusuallly high density of B_ϕ coils.

4.2 External poloidal magnetic field of tokamak GOLEM

As was shown in chapter 1, existence of external poloidal magnetic fields in tokamak is necessary for its operation. On tokamak GOLEM, externally generated B_θ is used to counteract hoop force and to control plasma column position. Spatial distribution of GOLEM poloidal field windings is shown in fig. 4.4, together with number of turns per coil. These windings also include high-temperature superconductors (HTS), which are

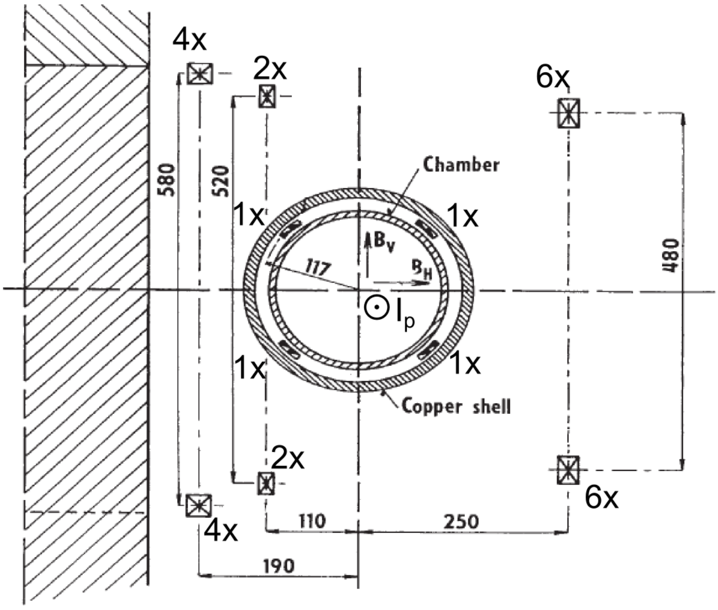

Figure 4.4: Scheme of poloidal field windings of tokamak GOLEM used for generation of external B_R and B_Z component (in scheme refered to as B_H and B_V respectively), together with number of coil turns and with standard GOLEM polarity of plasma current I_p. Dimensions are in mm

located on outboard side of tokamak (on LFS) on R coordinate of 0.65 m. As can be seen, all the windings are located ex-vessel, including a set of 4 fast-feedback control windings located underneath its copper shell.

Due to their toroidal symmetry, windings may be modelled in a more efficient way than it was done in the case of B_ϕ coils in section 4.1, where field from each element of each coil turn had to be accounted for individually. This symmetry enables to express integral part of equation 4.2 analytically (see ref. [24]). If

$$\mathbf{R} = \mathbf{r_0} - \mathbf{r_1}$$

where $\mathbf{r_0} = (R_0, Z_0)$ represents poloidal coordinates of point, where magnetic field is to be calculated and $\mathbf{r_1} = (R_1, Z_1)$ represents poloidal location of current-carrying conductor of toroidal symmetry, then (R,Z) components of integral vector can be expressed as follows:

$$\left[\oint_{\mathrm{l}} \frac{\mathrm{d}\mathbf{l} \times \mathbf{R}}{|\mathbf{R}|^3}\right]_R = \frac{(Z_1 - Z_0) f_1(k)}{R_0\sqrt{R_0 R_1}} ,$$

$$\left[\oint_{\mathbf{l}} \frac{\mathrm{d}\mathbf{l} \times \mathbf{R}}{|\mathbf{R}|^3}\right]_Z = \frac{R_0 f_1(k) + R_1 f_2(k)}{R_0\sqrt{R_0 R_1}} .$$

Quantities k, $f_1(k)$ and $f_2(k)$ are defined:

$$k^2 = \frac{4R_0R_1}{(R_0+R_1)^2 + (Z_0-Z_1)^2} ,$$

$$f_1(k) = k\left[K(k) - \frac{2-k^2}{2(1-k^2)}\,E(k)\right] ,$$

$$f_2(k) = \frac{k^3}{2(1-k^2)}\,E(k).$$

$K(k)$ and $E(k)$ represent Legendre's complete elliptic integrtal of the first and second kind for parameter k respectively. Thus, magnetic field on location $\mathbf{r_0} = (R_0, Z_0)$ from any toroidally symmetric current-carrying conductor placed in $\mathbf{r_1} = (R_1, Z_1)$ can be analytically expressed:

$$B_R(\mathbf{r_0}, \mathbf{r_1}) = \frac{\mu_0 I_c}{4\pi}\,\frac{(Z_1 - Z_0) f_1(k)}{R_0\sqrt{R_0R_1}} , \tag{4.4}$$

$$B_Z(\mathbf{r_0}, \mathbf{r_1}) = \frac{\mu_0 I_c}{4\pi}\,\frac{R_0 f_1(k) + R_1 f_2(k)}{R_0\sqrt{R_0R_1}} . \tag{4.5}$$

As can be seen from above relations, problem was fully transferred to calculation of complete elliptic integrals $K(k)$ and $E(k)$. Their calculation is a popular problem in mathematics and number of numerical algorithms that offer good efficiency and accuracy of calculation is available (in this work, iterative method of K and E calculation provided by [25] is used). Advantage of use of relations 4.4 and 4.5 becomes the most evident when problem with $\frac{|\mathbf{r_0}-\mathbf{r_1}|}{|\mathbf{r_0}|} << 1$ needs to be solved. This represents situation when magnetic field in very close proximity to its source needs to be known. Direct numerical calculation of eq. 4.2 will require a very small *dl* elements and even then it cannot guarantee accurate result, nor to provide an estimation on possible error of calculation. For elliptic integrals, $\frac{|\mathbf{r_0}-\mathbf{r_1}|}{|\mathbf{r_0}|} << 1$ condition is equivalent to $k \to 1$ which is where singularity occurs. Method in [25] exploits iterative algorithms that guarantee eventual calculation for any pre-defined precision.

4.2.1 Tokamak ferromagnetic core

Due to presence of ferromagnetic core, B_θ of tokamak GOLEM is not straightforward to model. It is a well-known fact that presence of ferromagnetic medium changes magnetic field in its vicinity, especially if field source is close to medium. Models of tokamak iron core are standardly toroidally symmetric (see models in ref. [24, 26, 27, 28]) and so is the one that was developed for tokamak GOLEM.

Model is based on integral approach as published in [24, 26]. It is assumed that all the effects of processes taking place within the core can be projected onto its surface. In the case of interest, a full model including correct form of volumetric effects is described in ref. **??** (the same is also provided in better accessible ref. [30]). For integral models, core surface represents iron-air boundary, where discontinuity of relative permeability μ_r takes place. Ref. [28] shows that condition of conservation of poloidal magnetic flux ψ on both sides of this boundary is equivalent to induction of surface currents on transformer core. Since these currents screen those in conductors which generated the aforementioned ψ, they are referred to as *screening currents*. Screening current density vector σ is given by following relation:

$$\sigma(\mathbf{r_0}) - \frac{\lambda}{2\pi}\int_S \left(\sigma(\mathbf{r_1}) \times \frac{\mathbf{r_0}-\mathbf{r_1}}{|\mathbf{r_0}-\mathbf{r_1}|^3}\right) \times \mathbf{n}(\mathbf{r_0})\mathrm{d}S_1 = \frac{\lambda}{2\pi}\int_V \left(\mathbf{j}(\mathbf{r_1}) \times \frac{\mathbf{r_0}-\mathbf{r_1}}{|\mathbf{r_0}-\mathbf{r_1}|^3}\right) \times \mathbf{n}(\mathbf{r_0})\mathrm{d}V_1. \tag{4.6}$$

There, vectors $\mathbf{r_0}$ and $\mathbf{r_1}$ represent locations of point of calculation and of conducting element respectively, this time in general 3D Cartesian coordinate system. Surface integral on left-hand side is across the whole surface of transformer, while volume integral on right-hand side is across the whole space outside the core (i.e. where external sources of B_θ, such as windings and plasma, are situated). $\mathbf{n}$ is normale vector to transformer surface and $\lambda = \frac{\mu_r - 1}{\mu_r + 1} \in (0, 1)$ is function of local relative permeability μ_r.

Since equation 4.6 is of 3D character, it can be used for ferromagnetic medium of any arbitrary location or shape. Right-hand side of the equation 4.6 represents toroidal currents in B_θ windings and plasma. Thus (if toroidally axisymmetric core is assumed), σ is toroidal as well. However, left-hand side of equation represents σ dependence on total B_θ, that is present on (R, Z) location. This includes field generated by screening currents of the rest of the core. If its surface is discretized into N toroidally symmetric filaments, σ is obtained by solving a set of N non-linear equations. The non-linearity comes from $\lambda = \lambda(\mu_r)$. Since $\mu_r = \mu_r(|\mathbf{B}|)$, λ depends on local B_θ. However, this quantity depends on σ as well. Since $\sigma = \sigma(\lambda)$, $B_\theta = B_\theta(\lambda)$ and $\lambda = \lambda(|\mathbf{B}|)$ at the same time. Ref. [26] and [28] show how this non-linearity can be accounted for by semi-analytical or by experimental $\mu_r = \mu_r(B)$ relations respectively. For tokamak GOLEM, the whole problem is linearized by assumption of $\mu_r > 10^2$, i.e. by assumtion of core being unsaturated across its whole surface.

4.2.2 Axisymmetric model of GOLEM core and its comparison to experiment

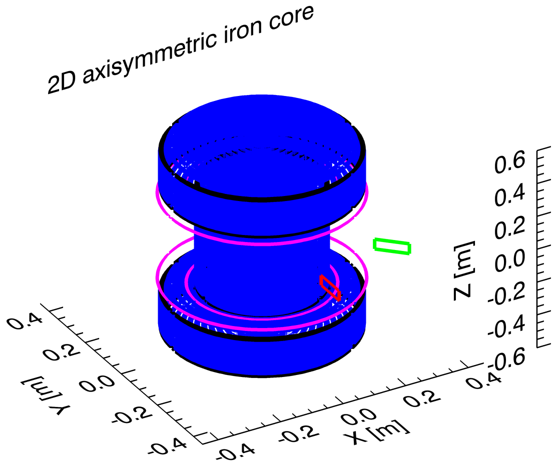

Figure 4.5: Blue – toroidally axisymmetric form of tokamak GOLEM core. Purple – coils that provided external poloidal field during the experiment. Red and green – areas where measurements took place, located at $\phi = \pi/2$ and $\phi = \pi/4$ respectively (large and small port).

An axisymmetric equivalent of tokamak GOLEM core is in form of central column cyllinder of radius R_{cen}, with two additional discs below and above of radii R_{disc} (see fig. 4.5). In order to find optimal values of R_{cen} and R_{disc}, a dedicated experiment took place. Current impulse of $I_c \sim 10^2$ A order from capacitor of $C = 3.2$ F was discharged into B_θ windings close to the core (see fig. 4.5 and fig. 4.6). Polarity configuration of coils was chosen to generate B_R field. Temporal evolution of B_R and of I_c was measured using MSL Hall probe, inserted into open tokamak chamber in a same manner as it was described in section 4.1.1. For each of the measurement locations (60 in total across

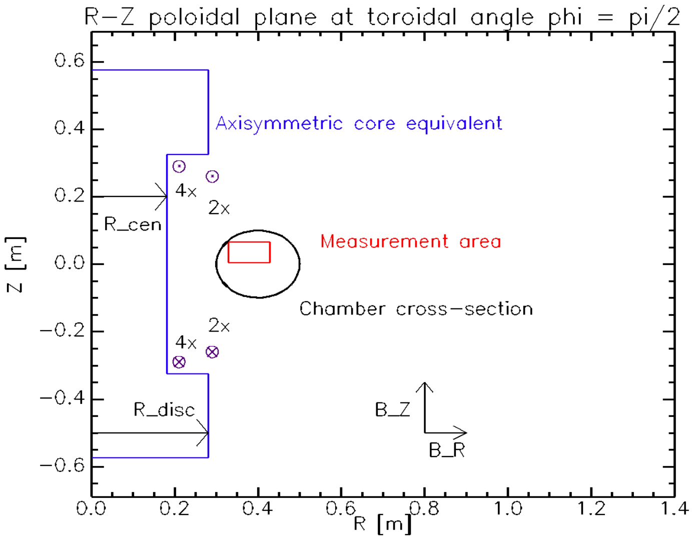

Figure 4.6: Poloidal cut through fig. 4.5 located at $\phi = \pi/2$. Purple symbols represent number of turns, locations and polarities of coils used to generate transformer response.

$R - Z$ plane for each of the ports), separate discharge into B_θ coils took place. Skin effect on tokamak chamber wall and copper shell, had slightly delayed B_R with respect to I_c evolution and thus quantity of $\max(B_R)/\max(I_c)$ was investigated. Current drive coils were not operational during the course of the experiment, thus it was safe to assume that core was unsaturated, i.e. that $\lambda \to 1$. It was found out (using experimental data as reference) that optimal dimensions of GOLEM axisymmetric core are $R_{cen} = 0.18$ m and $R_{disc1} = 0.23$ m for $\phi = \pi/2$ measurements and $R_{disc2} = 0.25$ m for $\phi = \pi/4$ measurements.

Both measured and modelled B_R densities are shown in fig. 4.7. Comparing fig. a) fig. to b) and fig. c) to fig. d) suggests that satisfactory axisymmetric equivalent of GOLEM core was found. However, difference between R_{disc1} and R_{disc2}, implies that such a model (in the case of strongly nonaxisymmteric GOLEM core) may be fully valid only for given ϕ. Nevertheless, poloidal field density provided by model for $\phi = \pi/4$ might be taken as an average one – $\phi = \pi/2$ on location of large port has lower core influence due to large distance from core limbs, while underneath these limbs is the core influence more significant.

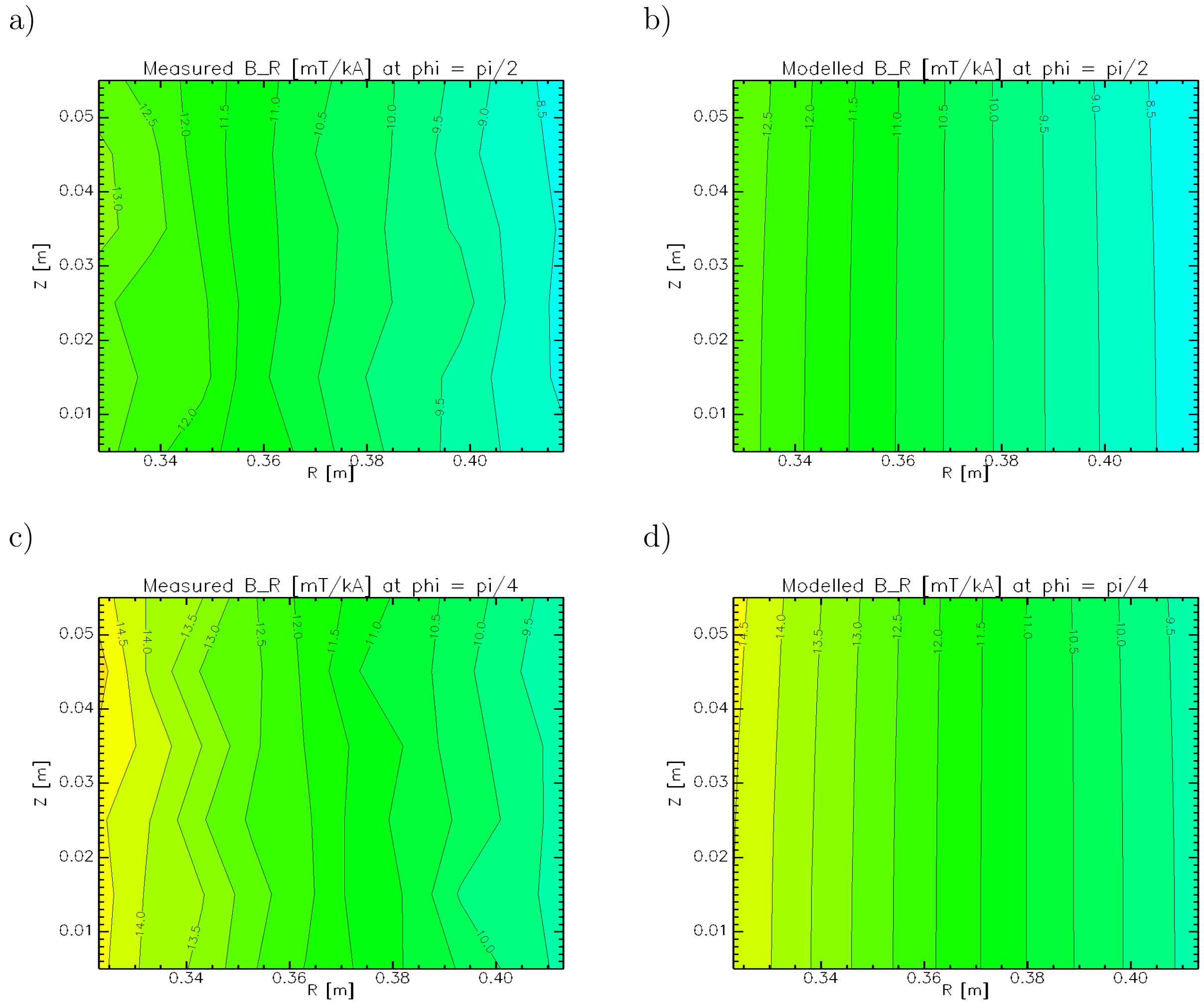

Figure 4.7: B_R/I_c density measured on angle $\phi = \pi/2$ – fig. a) and on angle $\phi = \pi/4$ – fig. c). Modeled density for respective locations is shown in fig. b) and d) for $R_{disc1} = 0.23$ and $R_{disc2} = 0.25$ m respectively. For explanation of dimensions and locations refer to fig. 4.5 and fig. 4.6.

4.2.3 GOLEM poloidal magnetic fields in presence of saturated and unsaturated core

Having acquired satisfactory model of iron core of tokamak GOLEM, external B_θ generated by all the possible coil configurations may be calculated – see figures 4.8, 4.9, 4.10 and 4.11. There, figures a) represent I_c polarities and arrow shows dominant character of generated B_θ. Figures b) represent generated B_θ (per turn of winding) using core of $\mu_r = 1$ across its whole surface and figures c) fields with core of $\mu_r >> 1$ (i.e. two different extremes). Also plasma region boundary defined by limiter is shown as a red line.

On first glance it is evident that iron core mainly affects B_R field generated by external windings in fig. 4.8. HTS windings located on outboard side of tokamak increased generated field across the whole chamber roughly by 5 mT/kA ($\mu_r >> 1$ case), compared to coil arrangement from section 4.2.2. Still, ratio between calculation with unsaturated core to calculation with saturated core:

$$\frac{B_{\mu_r>>1}}{B_{\mu_r=1}} \approx 2.5 - 3$$

was kept. Compared to this, fig. 4.9 shows some influence of core presence as well, but it has more character of change in gradient than change in magnitude. Moreover, fig. 4.10 and fig. 4.11 show that core influences B_θ generated by internal windings into a very small degree across the plasma region.

The main reason why is external-winding B_R field affected into such degree is due to coils being very close to core. Since:

$$B_R = -\frac{1}{2\pi R}\frac{\partial\psi}{\partial Z},$$

the B_R generation requires strong ψ gradient in Z direction. However, screening currents are induced in order to negate any possible $\frac{\partial\psi}{\partial Z}$ close to transformer surface, at the cost of $\frac{\partial\psi}{\partial R}$ increase in the vicinity. Inboard side coils (i.e. those on HFS) generate $\frac{\partial\psi}{\partial Z}$ right next to transformer surface, inducing high screening currents, paradoxly further strenghtening the generated B_R density. When coils are in B_Z generation regime, resulting $\frac{\partial\psi}{\partial R}$ induces lower screening currents, thus field in chamber is less affected, being far from the core. Similarly, coils under the copper shell are too far away from the core to be effectively screened.

As it was said, figures b) and c) represent two different extremes (althought scenario of completely saturated core in b) excludes possibility of plasma in tokamak) and thus real generated field is always somewhere in between. Future work on the model will include implementation of $\mu_r(|\mathbf{B}|)$ dependency, as well as generalization of model into 3D character.

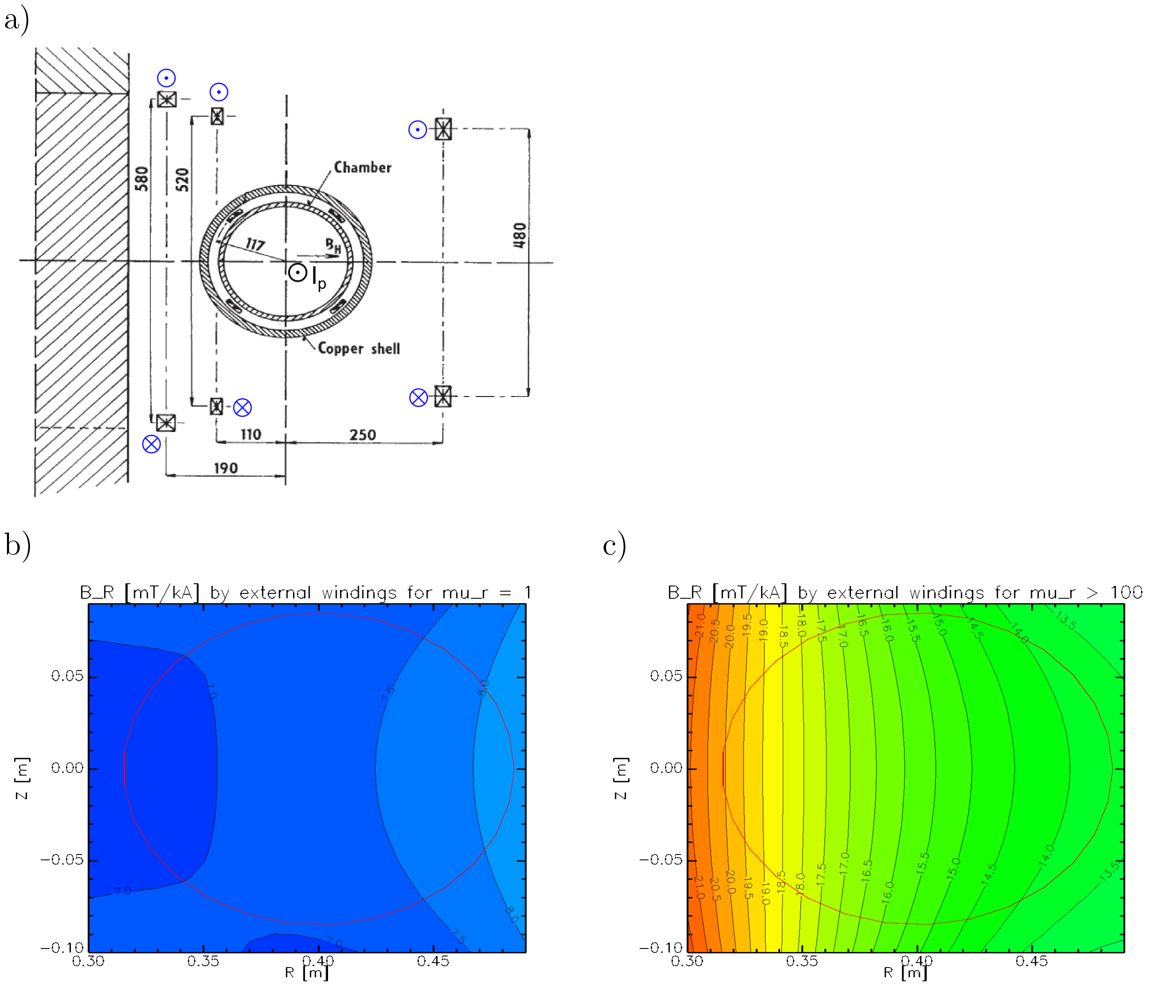
a)
b)
c)

Figure 4.8: B_R component of field generated by external windings of horizontal field shown in fig. a). Figure b) represents case of fully saturated core (air core model) and figure c) represents case of unsaturated core. Plasma limiter is represented by circular red line.

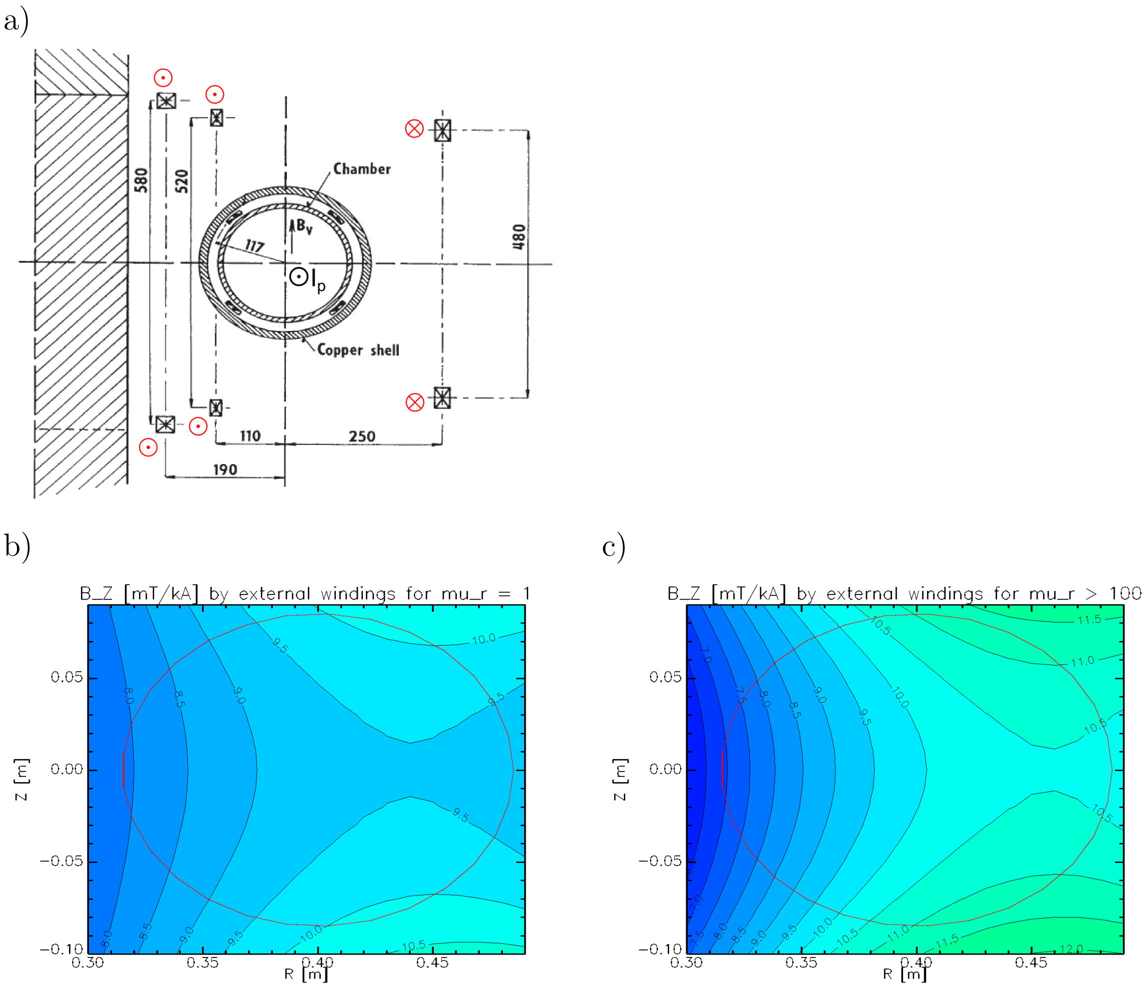

Figure 4.9: B_Z component of field generated by external windings of vertical field shown in fig. a). Figure b) represents case of fully saturated core (air core model) and figure c) represents case of unsaturated core. Plasma limiter is represented by circular red line.

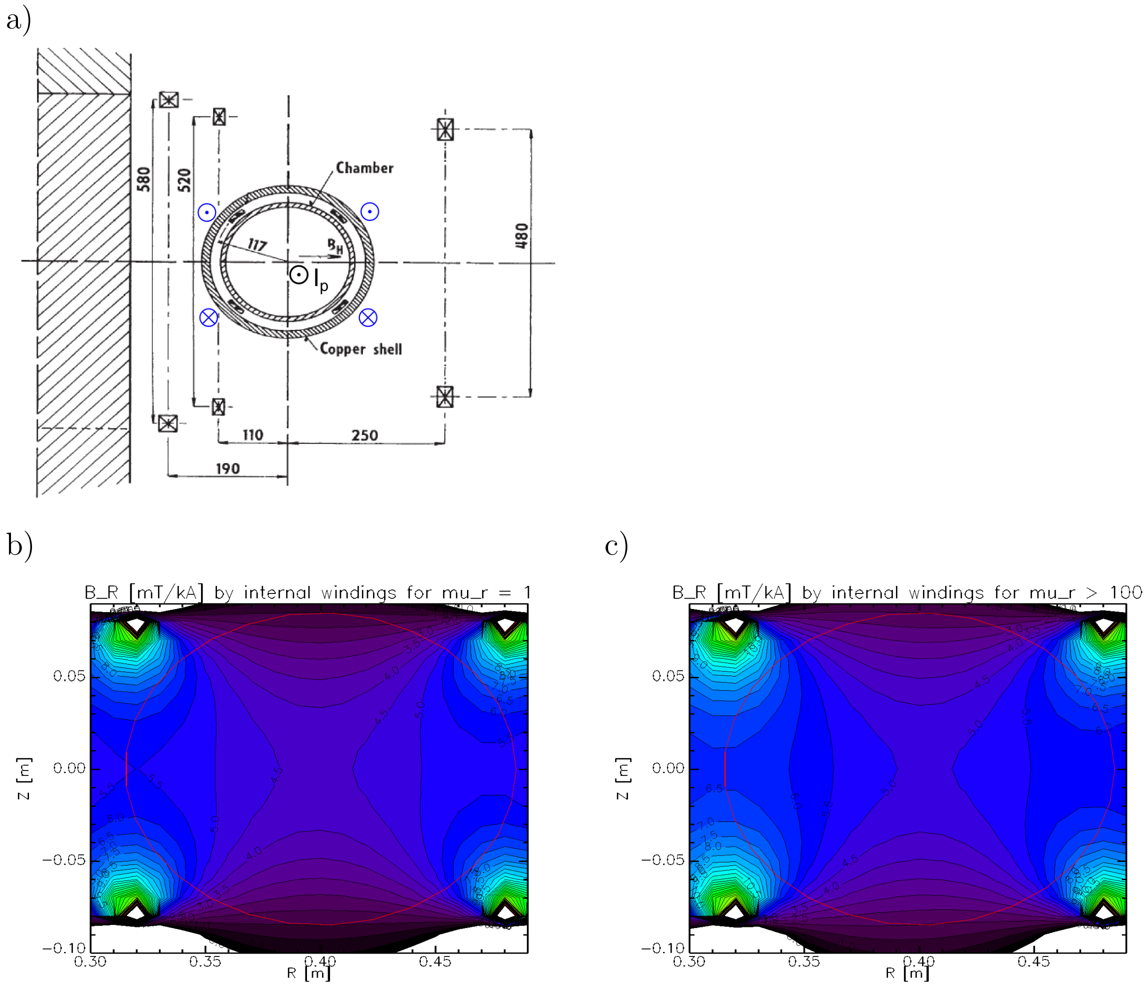

Figure 4.10: B_R component of field generated by fast feedback internal windings shown in fig. a). Figure b) represents case of fully saturated core (air core model) and figure c) represents case of unsaturated core. Plasma limiter is represented by circular red line.

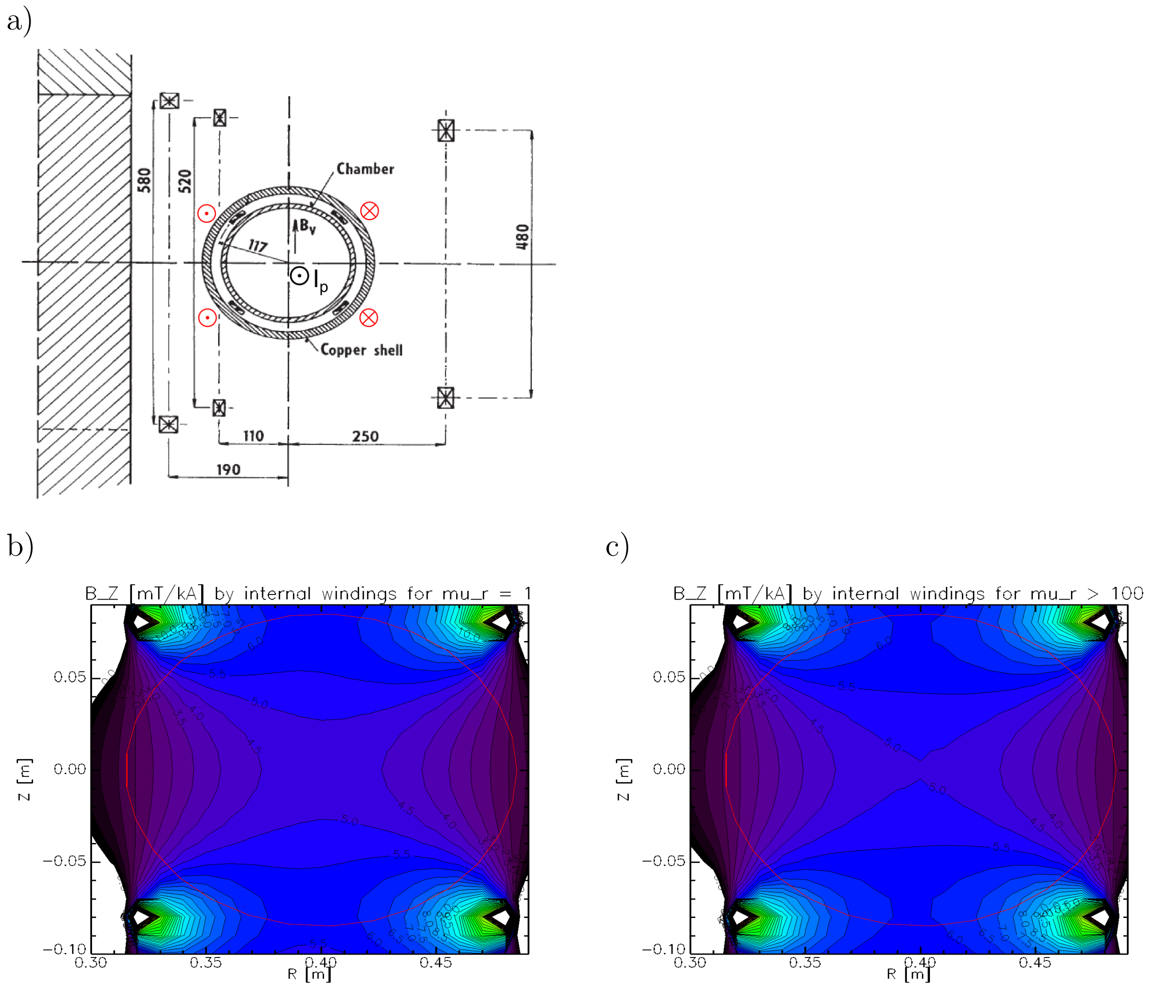

Figure 4.11: B_Z component of field generated by fast feedback internal windings shown in fig. a). Figure b) represents case of fully saturated core (air core model) and figure c) represents case of unsaturated core. Plasma limiter is represented by circular red line.

4.3 Stray fields

In iron core tokamaks, stray fields from current drive windings are significantly mitigated while the core is far from saturation. However, it was already mentioned in section 2.3.1 that in tokamak chamber, total toroidal current of

$$I_{ch} = \frac{U_{loop}}{R_{ch}}$$

is present. This current is responsible for induction of an additional stray field of B_Z character in pre-breakdown phase in following manner: Let tokamak chamber be divided into N conductors, located at different (R_i, Z_i) coordinates and having shape of toroidal loops of $2\pi R_i$ circumferences. In such a conducting loop, current is driven by presence of $\mathbf{E}$, induced in accordance with Faraday's law:

$$-\frac{\partial}{\partial t}\int_{S_l} \mathbf{B}\cdot \mathrm{d}\mathbf{S} = \oint_l \mathbf{E}\cdot \mathrm{d}\mathbf{l}.$$

For toroidal loops, only B_Z component is of relevance, as it induces toroidal E_ϕ. During pre-breakdown phase, dominant B_Z is that of transformer action, which is present within cross-sectional area S_c of central column. Thus:

$$-S_c\frac{\partial B_Z}{\partial t} = 2\pi R E_\phi = U_{loop}.$$

From previous relation, the important implication is:

$$U_{loop}(R, Z) = \text{const} \quad \rightarrow \quad E_\phi \sim \frac{1}{R}\,.$$

Note analogy to $B_\phi \sim \frac{1}{R}$ profile. If electrical properties of chamber are fully characterized by its resistivity per unit of length ρ_l, then currents I_i in chamber elements follow relation:

$$I_i(R_i) = \frac{U_{loop}}{2\pi\rho_l R_i} \sim \frac{1}{R_i}\,. \tag{4.7}$$

By using condition of $I_{ch} = \sum_i I_i$, more elegant expression is obtained:

$$I_i = \frac{1}{R_i}\frac{I_{tot}}{\sum_j 1/R_j}\,. \tag{4.8}$$

$I_i \sim 1/R_i$ character implies that chamber currents on HFS are highest in magnitude, which is intuitively expected as current chooses way of the lowest resistivity. Resulting stray field of chamber as a whole is calculated by summation over all of the $\mathbf{B_i} =$

(B_{Ri}, B_{Zi}) stray fields by each individual loop. Since the loops are toroidally symmetric, numerically efficient eq. 4.4 and eq. 4.5 can be used for $\mathbf{B_i}$ evaluation.

At this point, it should be noted that model above is relevant only for pre-breakdown phase of the discharge, provided that transformer is far from its saturation. Otherwise, not only I_{ch} drops to low magnitudes, but also $U_{loop}(R, Z) \neq \text{const}$ and thus I_i distribution is of different character than of $\sim 1/R$.

4.3.1 Comparison of measurements to model

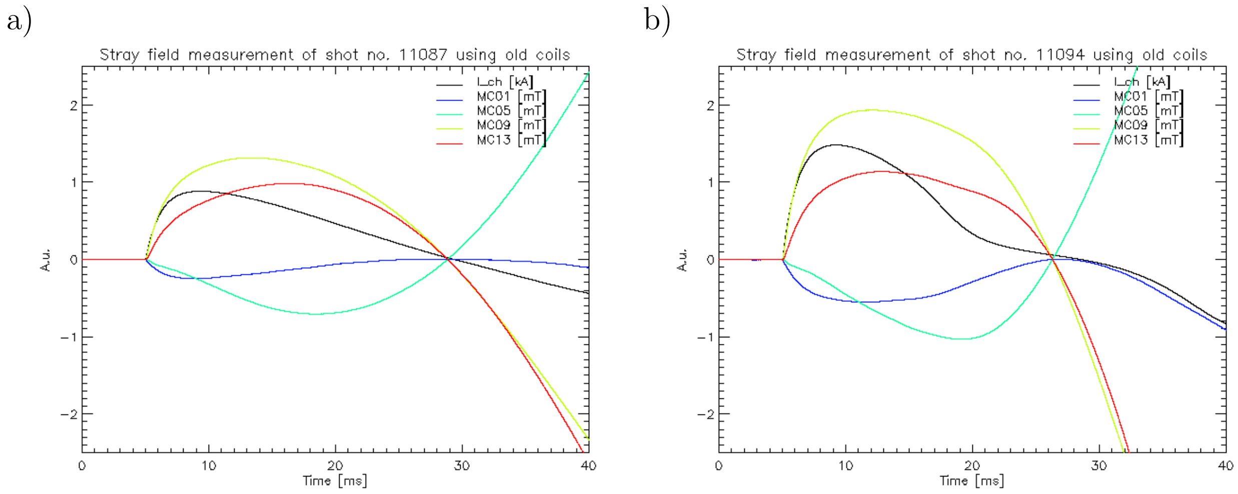

Figure 4.12: An example of B_θ stray fields measurement by old Mirnov coils, using two shots with different degree of iron core saturation (see character of I_{ch} evolution around 20th ms).

	LFS	HFS	TOP	BOT
B_Z [mT/kA]	-0.38 ± 0.08	-1.3 ± 0.1	–	–
B_R [mT/kA]	–	–	0.72 ± 0.07	0.8 ± 0.2

Table 4.1: Results of stray fields with old Mirnov coil measurements over multiple discharges.

The measurement of stray fields took place with closed chamber, i.e. without MSL Hall probe. Instead, ring coils and old Mirnov coils had been used for measurements. B_θ was obtained from

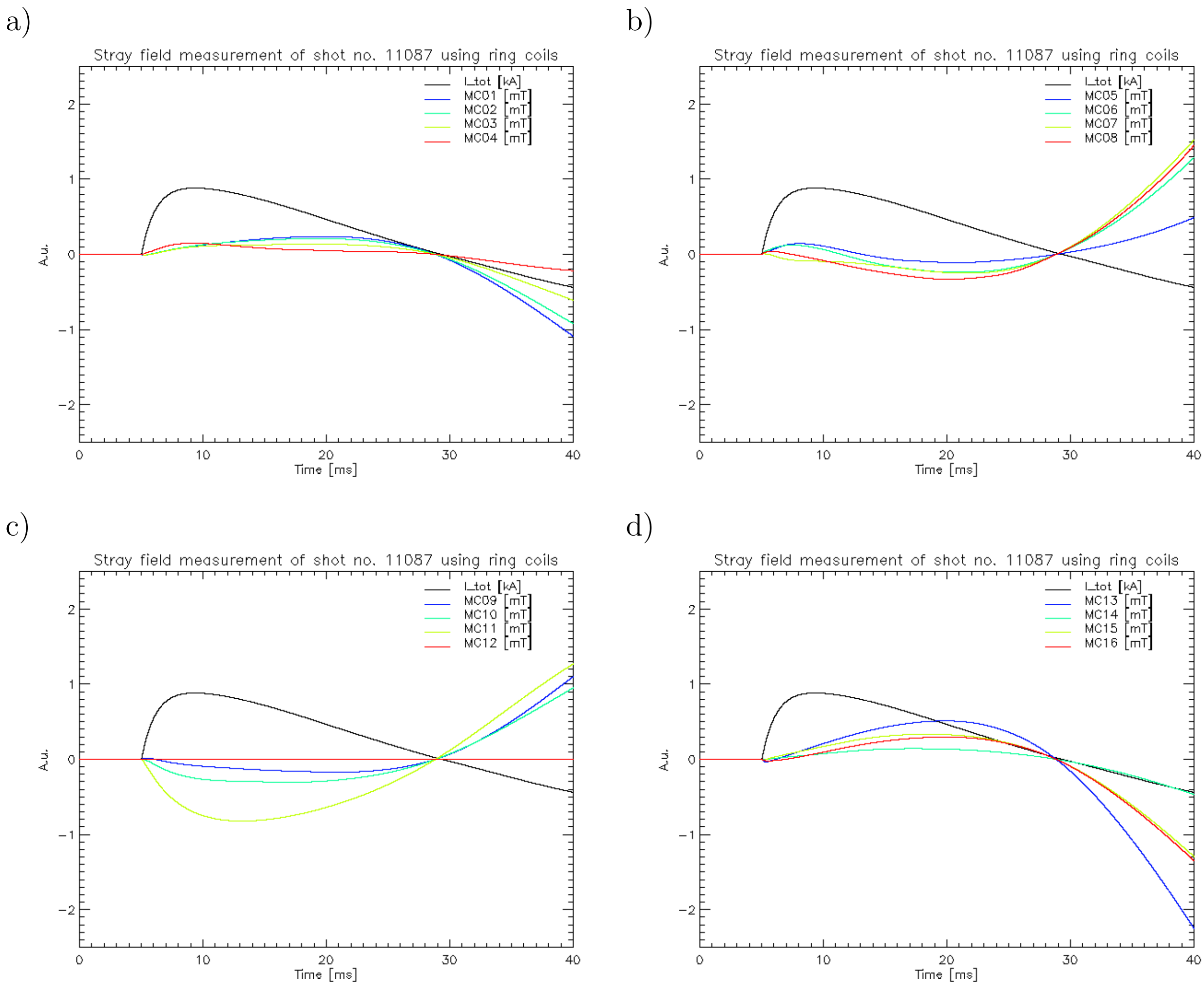

Figure 4.13: B_θ stray fields measurement by ring coils for discharge with low core saturation.

$$B_\theta(t_N) = \frac{POL}{f_s A_{eff}} \sum_{i=0}^{N} U_{out}(i),$$

where $U_{sig} = U_{out}$ was assumed (refer to section 5.1). f_s represents sampling frequency and POL and A_{eff} quantities are obtained from tab. 5.1. Of tokamak windings only current drive coils were energized, thus the only B field present was that of stray character. In the course of the experiment, stray fields of 10 discharges with different degree of core saturation were investigated and it was observed, that results from both old Mirnov coils and ring coils strongly depend on degree of this saturation – see fig. 4.12 for old Mirnov coils and fig. 4.13 and fig. 4.14 for ring coils. Note B_θ component is plotted and thus:

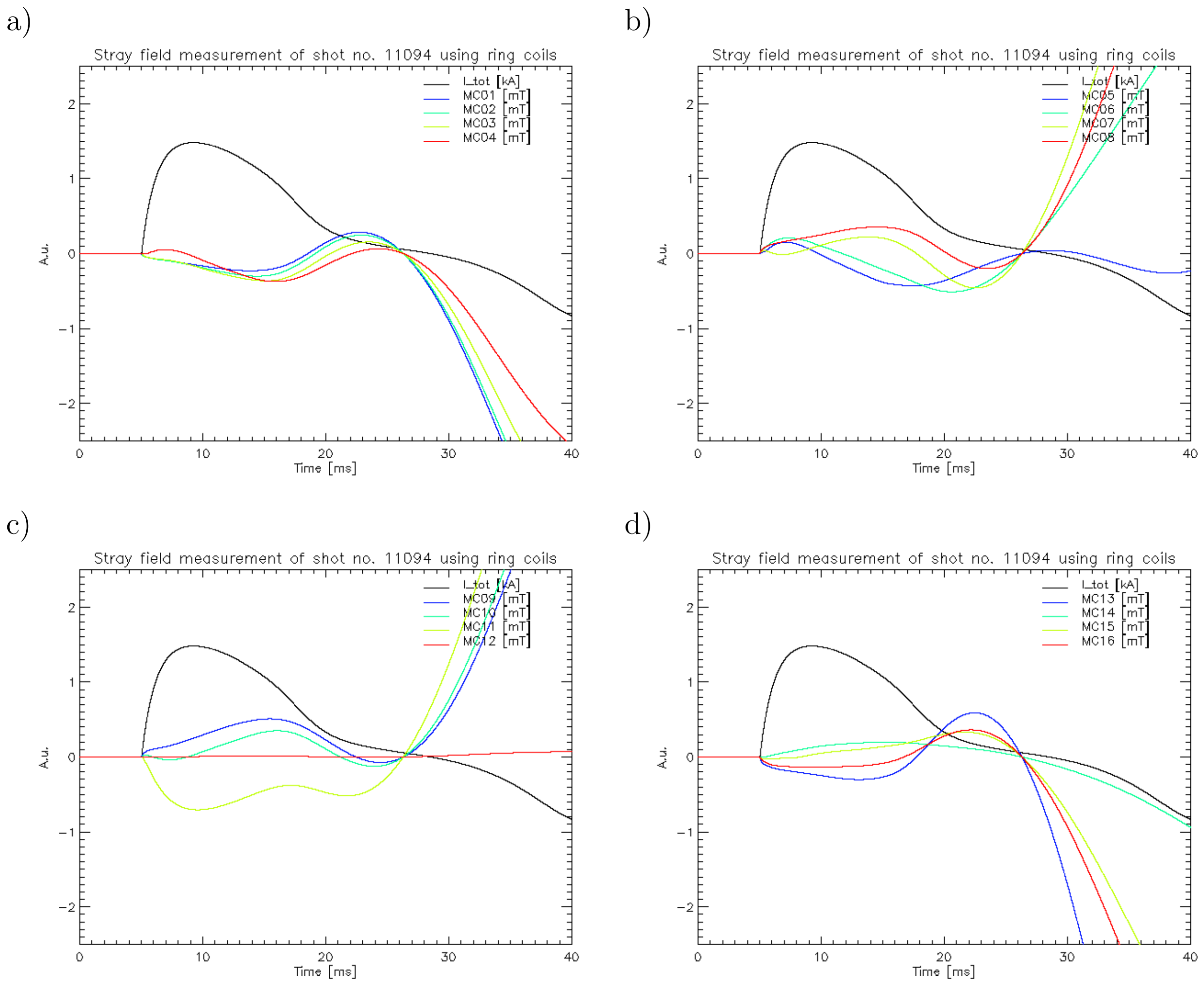

Figure 4.14: B_θ stray fields measurement by ring coils for discharge with high core saturation.

$$B_R = -B_\theta \sin\theta \quad \text{and} \quad B_Z = B_\theta \cos\theta,$$

where θ is poloidal location of detection coil obtained from fig. 2.8 and fig. 3.5. Therefore fig. 4.12 implies that old Mirnov coils detect stray field of $-\mathbf{i_Z}$ direction on LFS and HSF, and $+\mathbf{i_R}$ direction on TOP and BOT, regardless of core saturation degree. Moreover tab. 4.1, which represents $\frac{\max B_\theta(t)}{\max I_{tot}(t)}$ for $t \in (0, 30)$ ms, implies that magnitude of the field stays the same as well (upon normalization to I_{ch}) – over 10 different discharges, the relative deviation from mean value is in range of $8 - 25\%$. Fig. 4.15 compares these detected values to model of stray fields induced by chamber currents. For reference, a popular approximation model with uniform chamber currents of $I_i = I_{tot}/N$ is shown as well. As

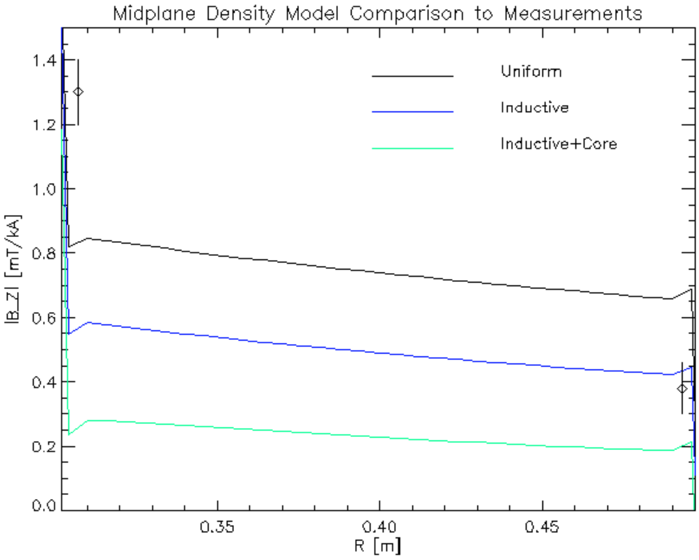

Figure 4.15: Comparison of stray fields, calculated using different models of I_i current distribution, with results in tab. 4.1.

can be seen, only on LFS prediction by one of models falls into uncertainty interval of measurement – on HFS the detected magnitude is far too strong. The same goes for TOP and BOT – expected B_R field by models is virtually zero. Also, the drift of signal at the end of discharge is not of stochastic character – in fact the opposite is the case as it exhibits very good reproducibility. This implies that it represents real B_θ quantity present on given location.

The same applies for the signal drift of the ring coils in fig. 4.13 and fig. 4.14, althought in this case there seems to be stronger dependence on degree of core saturation and lower detected B_θ magnitudes. Around 16th ms in fig. 4.14 (i.e. around the time when starts to approach saturation), B_θ seems to dramatically change its character. This, supported by plots in fig. 4.12 and fig. 4.13, implies that stray fields by current drive system are dominant over those induced by I_{ch}. Still, this investigation took place at areas close to tokamak chamber wall, thus measurement of stray fields in the center of chamber (using MSL Hall probe) is advised to be done in future.

Chapter 5

Plasma magnetic field measurements

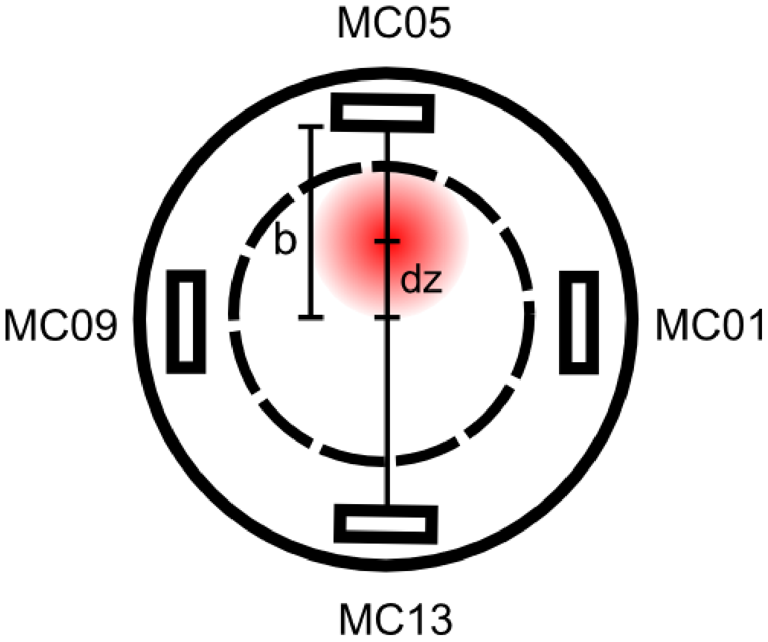

Figure 5.1: Shift of plasma column position in vertical direction. MC's represent Mirnov coils of respective number, be it old or new array.

Since magnetic fields of tokamak device as such are generated by fixed external windings, their character is from the most part predictable. This is not the case of plasma B, which is generated by $\mathbf{j}(r)$ current density. Since in tokamaks $\mathbf{j} \approx j_\phi \mathbf{i}_\phi$, plasma field $\mathbf{B} \approx B_\theta \mathbf{i}_\theta$. Thought there are some exceptions, e.g. generation of B_{dia} antiparallel to B_ϕ due to plasma diamagnetism. Since $\frac{B_{dia}}{B_\phi} \sim 10^{-3}$, a specifically precise and accurate diagnostics is needed to quantify this effect. However, this is not yet installed on tokamak GOLEM.

Measurements of (unperturbed) B_θ are necessary input for plasma equilibrium reconstruction, thus section 5.1 provides investigation of possibilities of measurements of this quantity on GOLEM. Relevance of used methods is then discussed in section 5.2 on estimation of vertical position of plasma position.

While for linear conductor $B_\theta \sim 1/R$, for toroidal loop conductor this is no longer generally the case, since magnetic field density is shifted from outward regions towards center of loop. In that case, $B_\theta \sim 1/R$ represents average field, which equals actual magnitude of B_θ only on location directly above and below of loop conductor. Using two B_θ detectors on these locations (event. together with Rogowski coil), it is possible to specify vertical location of plasma column dz. By taking situation in fig. 5.1 into consideration:

$$B_5 = \frac{\mu_0 I_p}{2\pi}\frac{1}{b-dz} \quad \text{and} \quad B_{13} = \frac{\mu_0 I_p}{2\pi}\frac{1}{b+dz}$$

where I_p represents total plasma current. Let there be definition:

$$B_0 = \frac{\mu_0 I_p}{2\pi b}\,.$$

Then, under assumption that $b^2 >> dz^2$, it is straightforward to show that:

$$dz = b\frac{B_5 - B_{13}}{2B_0}\,. \tag{5.1}$$

Also, under the same assuption, $B_5 + B_{13} = 2B_0$ is valid. Thus, more elegant, relation is obtained:

$$dz = b\frac{B_5 - B_{13}}{B_5 + B_{13}}\,.$$

This specific expression however, is more prone to systematic errors, since $b^2 >> dz^2$ approximation had to be used twice and since B_5 and B_{13} quantities are measured less reliably than I_p (as can be seen in following section).

5.1 Processing of Mirnov coils signal

It was shown in section 3.3 that all the B_θ probes on tokamak GOLEM may be considered as ideal transfer systems even for highest-frequency oscillations. This is even more valid for global B_θ evolution taking place at lowest frequencies, thus $U_{out} = U_{sig}$. Since there

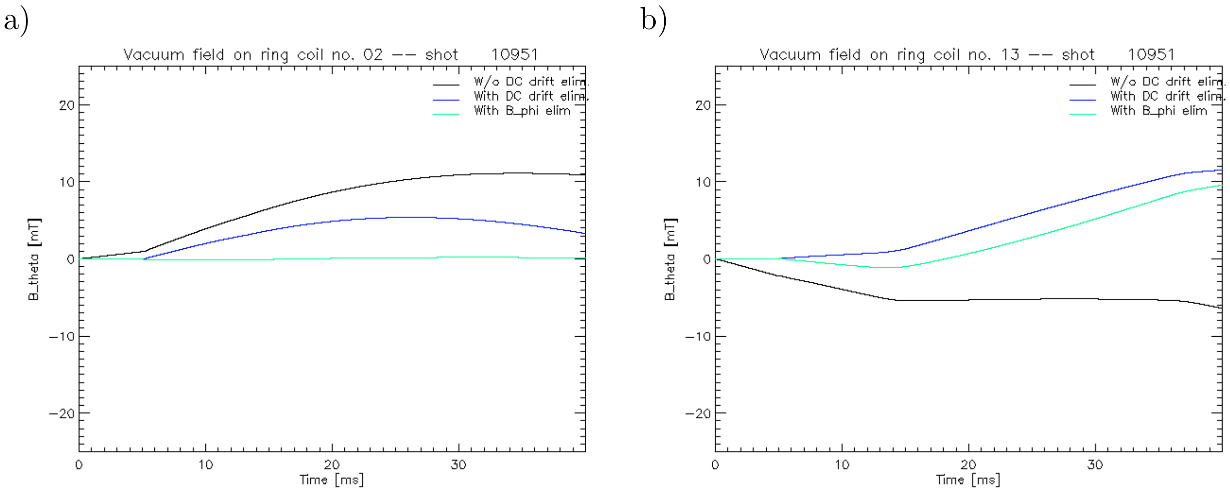

Figure 5.2: Application of relations 5.2, 5.3 and 5.4 respectively for two different ring coils.

are no routinely operational analogue integrators on tokamak GOLEM, integration of U_{out} is carried out numerically:

$$B_\theta(t) = \frac{POL}{A_{eff}} \int_0^t U_{out}(\tau)\mathrm{d}\tau \quad \rightarrow \quad B_\theta(t_N) = \frac{POL}{f_s A_{eff}} \sum_{i=0}^{N} U_{out}(i). \tag{5.2}$$

Quantity f_s is sampling frequency, $POL = \pm 1$ polarity of the coil and $t_N = N/f_s$. However, should there be constant DC offset of U_{DC}, the result would be superposition of integrated plasma signal and linear dependency from integrated DC offset. Therefore, relation

$$B_\theta(t_N) = \frac{POL}{f_s A_{eff}} \sum_{i=0}^{N} \left(U_{out}(i) - U_{DC}\right). \tag{5.3}$$

is more relevant than the one before.

It must be kept in mind that here U_{out} represents signal from both plasma magnetic field and the field of external tokamak windings – i.e. that of *vacuum field*. This part of signal is not of interest in the case of plasma investigation and needs to be subtracted from result. First of all, for plasma discharge to take place, high-magnitude B_ϕ field must be present. Since it is not possible to provide perfect poloidal orientation of the coils, part of A_{eff} of coils is aligned toroidally, causing non-negligible cross-talk by this B_ϕ. Making series of vacuum discharges allows to specify A_ϕ constant for each B_θ probe,

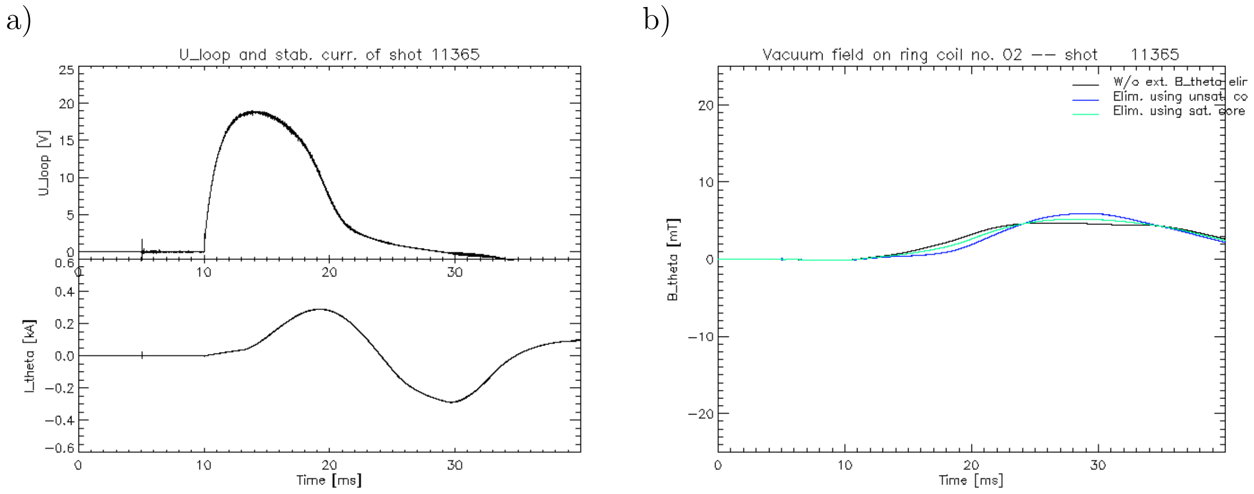

Figure 5.3: Subtraction of B_θ from external windings. Fig. a) – global parameters of discharge. Above - loop voltage, below - current in external winding (in fig. 4.8). b) output of relations 5.4 and 5.5 (using $A_{\theta 1}$ and $A_{\theta 2}$ from tab. 5.1 resp.).

which will enable elimination of this cross-talk in following manner:

$$B_\theta(t_N) = \frac{POL}{f_s A_{eff}} \sum_{i=0}^{N} (U_{sig}(i) - U_{DC}) - A_\phi B_\phi(t_N). \tag{5.4}$$

A_ϕ constants for both new and old GOLEM Mirnov coils are to be found in tab. 5.1. Results of application of relations 5.2, 5.3 and 5.4 to process vacuum discharge signal of two different coils are shown in fig. 5.2. It can be clearly seen that only the use of expression 5.4 is relevant of the three. Despite that, signals of ring coil 13 and of ring coil 16 show significant drift. Also, signal of ring coil 12 is one order lower than the rest: $U_{sig12} \approx 10^{-1} \cdot U_{sig}$. It was concluded that there might be damage of some sort to the coils or twisted pair cable and therefore, it is not advised to fully trust output of ring coils 12, 13 and 16, until the matter is investigated further.

In the case that external B_θ is generated by tokamak windings, this field should be subtracted from result as well. This can be done in similar way as it was done with B_ϕ cross-talk, i.e.:

$$B_\theta(t_N) = \frac{POL}{f_s A_{eff}} \sum_{i=0}^{N} (U_{sig}(i) - U_{DC}) - A_\phi B_\phi(t_N) - A_\theta I_{stab}. \tag{5.5}$$

I_{stab} represents current in respective stabilization winding. A_θ is obtained from relevant model of given poloidal field – see chapter 4. Tab. 5.1 provides A_θ for external B_R

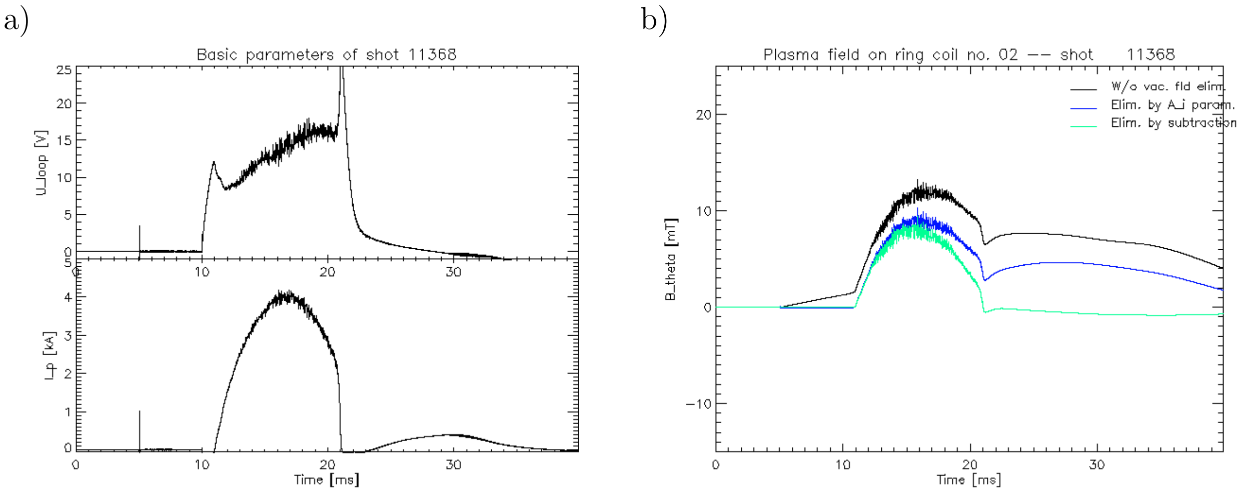

Figure 5.4: Fig. a) – global parameters of plasma discharge. Fig. b) – plasma magnetic field obtained using expression 5.3, 5.5 and 5.6 respectively.

generation winding, for the case of unsaturated and saturated transformer. Results in fig. 5.3 b) nevertheless show that even thought external B_θ cross-talk might be eliminated this way, there is an additional signal of different character present. Fig. 5.3 a) shows that U_{loop} signal has typical signature of core saturation, therefore stray fields from current-drive winding are suspected to be the cause.

Finally, there is also a completely different approach on how to eliminate vacuum field part of signal. By making discharge of the same currents in all the windings of tokamak, and without injection of work gas to prevent breakdown, U_{vac} signal for each probe can be obtained. Then:

$$B_{theta}(t_N) = \frac{POL}{f_s A_{eff}} \sum_{i=0}^{N} \left[(U_{sig}(i) - U_{DC}) - (U_{vac}(i) - U_{DC}^{vac}) \right] . \tag{5.6}$$

Fig. 5.4 shows B_θ of plasma, obtained by relations 5.3, 5.5 and 5.6 respectively. It is evident that elimination of vacuum field signal needs to take place, as its effect is not negligible. An optimal method for this seems to be the one using an additional vacuum discharge and simple subtraction (i.e. eq. 5.6). However, making an extra vacuum shot is not always possible. Fig. 5.4 b) shows both methods of vacuum field signal elimination give very similar results until maximum of I_p, which implies that relation 5.5 might be trusted during current ramp-up period. This matter is investigated further in following section.

Name	A_{eff} [cm^2]	POL [-]	A_ϕ [-]	$A_{\theta 1}$ [T/A]	$A_{\theta 2}$ [T/A]
MC01	37.0	-1	$15.3 \cdot 10^{-3}$	$0.0 \cdot 10^{-6}$	$0.0 \cdot 10^{-6}$
MC05	37.0	-1	$-34.8 \cdot 10^{-3}$	$15.2 \cdot 10^{-6}$	$7.0 \cdot 10^{-6}$
MC09	37.0	+1	$-45.8 \cdot 10^{-3}$	$0.0 \cdot 10^{-6}$	$0.0 \cdot 10^{-6}$
MC13	37.0	+1	$-12.4 \cdot 10^{-3}$	$-15.2 \cdot 10^{-6}$	$-7.0 \cdot 10^{-6}$
1	68.9	-1	$13.2 \cdot 10^{-3}$	$0.0 \cdot 10^{-6}$	$0.0 \cdot 10^{-6}$
2	140.7	-1	$15.2 \cdot 10^{-3}$	$4.7 \cdot 10^{-6}$	$2.1 \cdot 10^{-6}$
3	138.9	+1	$-15.4 \cdot 10^{-3}$	$9.1 \cdot 10^{-6}$	$4.1 \cdot 10^{-6}$
4	140.4	+1	$14.3 \cdot 10^{-3}$	$12.7 \cdot 10^{-6}$	$5.8 \cdot 10^{-6}$
5	68.6	-1	$9.0 \cdot 10^{-3}$	$15.2 \cdot 10^{-6}$	$7.0 \cdot 10^{-6}$
6	134.5	+1	$19.0 \cdot 10^{-3}$	$15.6 \cdot 10^{-6}$	$7.2 \cdot 10^{-6}$
7	134.3	-1	$4.6 \cdot 10^{-3}$	$13.2 \cdot 10^{-6}$	$6.1 \cdot 10^{-6}$
8	142.5	+1	$-12.2 \cdot 10^{-3}$	$7.7 \cdot 10^{-6}$	$3.5 \cdot 10^{-6}$
9	67.6	-1	$1.0 \cdot 10^{-3}$	$0.0 \cdot 10^{-6}$	$0.0 \cdot 10^{-6}$
10	142.8	+1	$-7.8 \cdot 10^{-3}$	$-7.7 \cdot 10^{-6}$	$-3.5 \cdot 10^{-6}$
11	140.4	-1	$-11.2 \cdot 10^{-3}$	$-13.2 \cdot 10^{-6}$	$-6.1 \cdot 10^{-6}$
12	138.0	-1	$0.6 \cdot 10^{-3}$	$-15.6 \cdot 10^{-6}$	$-7.2 \cdot 10^{-6}$
13	76.3	-1	$9.3 \cdot 10^{-3}$	$-15.2 \cdot 10^{-6}$	$-7.0 \cdot 10^{-6}$
14	142.2	-1	$0.6 \cdot 10^{-3}$	$-12.7 \cdot 10^{-6}$	$-5.8 \cdot 10^{-6}$
15	139.8	-1	$-1.6 \cdot 10^{-3}$	$-9.1 \cdot 10^{-6}$	$-4.1 \cdot 10^{-6}$
16	139.3	-1	$-38.5 \cdot 10^{-3}$	$-4.7 \cdot 10^{-6}$	$-2.1 \cdot 10^{-6}$

Table 5.1: Overview of operational parameters of all the GOLEM Mirnov coils. MC's represent old Mirnov coils, the rest are those of the ring. POL represents coil polarity, $A_{\theta 1}$ represents unsaturated core and $A_{\theta 2}$ fully saturated core.

5.2 Vertical plasma position determination on tokamak GOLEM

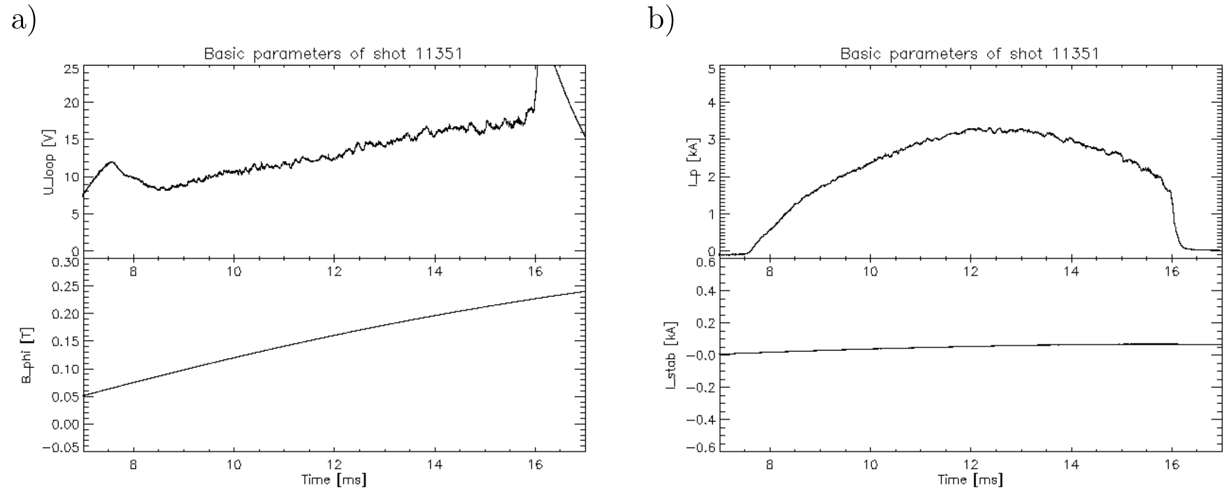

Figure 5.5: Basic plasma parameters – shot without vertical position stabilization. I_{stab} refers to current in winding of external B_R generation in fig. 4.8.

To see how much is B_θ obtained from expression 5.5 reliable, it has been used to estimate dz quantity from relation 5.1. This quantity is then compared to dz obtained using B_θ from relation 5.6. Note that this indeed is estimation, since the relation 5.1 itself is valid only for $dR = 0$ displacement, when detection coils are situated directly above and below plasma column.

For discharge without stabilization (see fig. 5.5), in fig. 5.6 it is seen that plasma drifts towards TOP of the chamber. dz estimation was done both by ring coils – figure a) and by old Mirnov coils – figure b). However, it was mentioned in section 5.1 that signal of ring coil no. 13 might not be fully reliable. Despite that, it seems to manage to characterize the trend in plasma column drift towards TOP. Fig. 5.6 b) yields, that use of relation 5.5 to obtain B_5 and B_{13} causes dz estimation to be initially lower in chamber, but it keeps the same increment in dz as more reliable method by relation 5.6, up until I_p maximum in 12th ms. As was seen in fig. 5.4, after this point the relation 5.5 is no longer valid and thus the observed downwards motion in plot 5.6 b) does not correspond to physical reality.

To see whether discrepancy in position estimation due to use of less reliable probes (such as ring coil 13) takes place, let there now be discharge with vertical plasma position

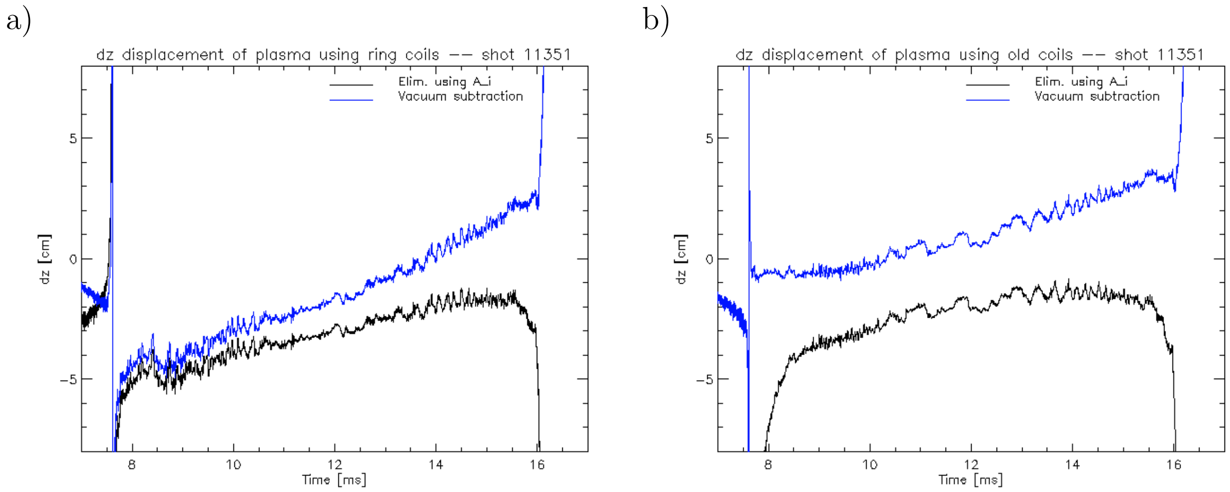

Figure 5.6: Vertical plasma displacement dz from relation 5.1. Fig. a) – using new ring coils. Fig. b) – using old coils. In both cases is B_θ calculated with expressions 5.5 and 5.6 respectively.

stabilization – see fig. 5.7 and let relation 5.6 be used to obtain B_5 and B_{13} for dz estimation. Then, fig. 5.8 implies that plasma was indeed prevented from its upwards motion thanks to this field, althought ring coil 13 seem not to have noticed this.

To conclude this chapter, it was found out that the best way how to eliminate vacuum field part from B_θ signal is to use expression 5.6. However, this requires an additional vacuum discharge, which is not always possible. In that case, expression 5.5 (using parameters from tab. **??**) can be used as well, althought only for limited part of plasma signal. When dz quantity is of interest, it is best to use old Mirnov coils, since coil 13 (and also 12 and 16) of ring coils seems to be of limited reliability – the cause will be investigated in future by their removal from tokamak and close inspection.

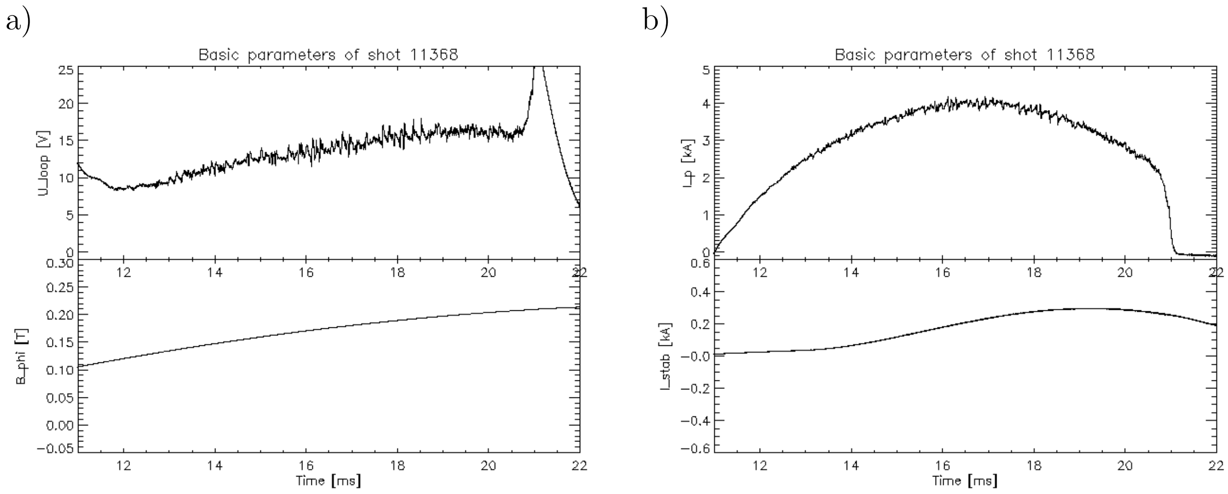

Figure 5.7: Basic plasma parameters – shot with vertical position stabilization. I_{stab} refers to current in winding of external B_R generation in fig. 4.8.

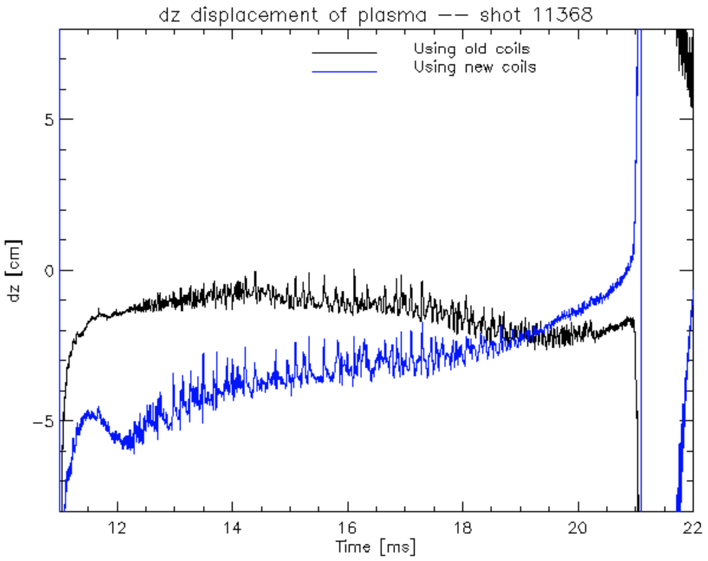

Figure 5.8: Vertical plasma displacement dz from relation 5.1, using new ring coils and old coils respectively. B_θ calculated with expression 5.6.

Chapter 6

Plasma magnetic field fluctuations model

The main motivation behind instalation of new array of 16 ring coils was to detect structure of resistive MHD instabilities of tokamak GOLEM plasma. As is shown in section 6.1, presence and rotation of these structures cause perturbations of B_θ across θ and time respectively. By analysis of these fluctuations, spatial structure of instability and frequency of its rotation f_θ in plasma are obtained. Section 1.2 has shown how structure of specific MHD instability is connected with global plasma parameters and with location of its r_s resonant surface. Once this quantity is obtained, velocity of its poloidal rotation $v_\theta = 2\pi f_\theta r_s$ can be estimated. Even thought instability spatial structure and f_θ can be directly extracted from perturbation of signal in (θ, t) space, in section 6.2 it is shown how statistical methods of analysis (fast Fourier transform and cross-correlation) are applied to obtain more accurate results.

6.1 Simulated plasma MHD structures

For proper interpretation of measurements of MHD structures, relevant simulation of plasma B_θ during presence of these instabilities is necessary. These instabilities come in form of magnetic islands as a perturbation of magnetic field line on resonant $q(r_s)$ surface. In Cartesian coordinate system, this field-line equation is in form:

$$\frac{\mathrm{d}x}{B_x} = \frac{\mathrm{d}y}{B_y} = \frac{\mathrm{d}z}{B_z} = \frac{\mathrm{d}s}{B}\,,$$

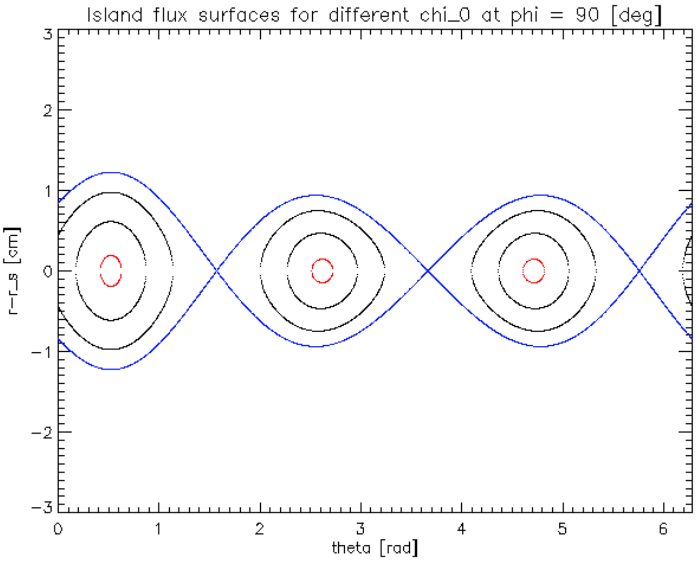

Figure 6.1: Solution of eq. 6.4 for typical GOLEM low q discharge parameters, with island of $m/n = 3/1$ located close to plasma edge.

where s is distance along this field line. On $q(r_s) = m/n$ surface, field line follows helical trajectory and does m/n full toroidal revolutions per each poloidal one. Using transformation:

$$\chi = \theta - \frac{n}{m}\phi,$$

unperturbed B_θ takes form:

$$B^* = B_\theta \left(1 - \frac{n}{m} q(r)\right).$$

For resonant surface, $B^*(r_s) = 0$. Note that χ represents angular coordinate, not toroidal flux. By substitution of χ and B^* relations into that of magnetic field line, expression:

$$\frac{\mathrm{d}r}{B_r} = \frac{r_s \mathrm{d}\chi}{B^*} \tag{6.1}$$

is obtained. Ref. [1] then further shows how this equation can be solved. As can be seen in relation 6.1, magnetic field perturbation is of radial character, in accordance with diffusion of magnetic field from resistive MHD (see section 1.2). Additionally, B_r is constant along the field line, thus:

$$B_r = \overline{B_r}\mathrm{e}^{\mathrm{i}m\chi} \quad \rightarrow \quad B_r = \overline{B_r}\sin m\chi. \tag{6.2}$$

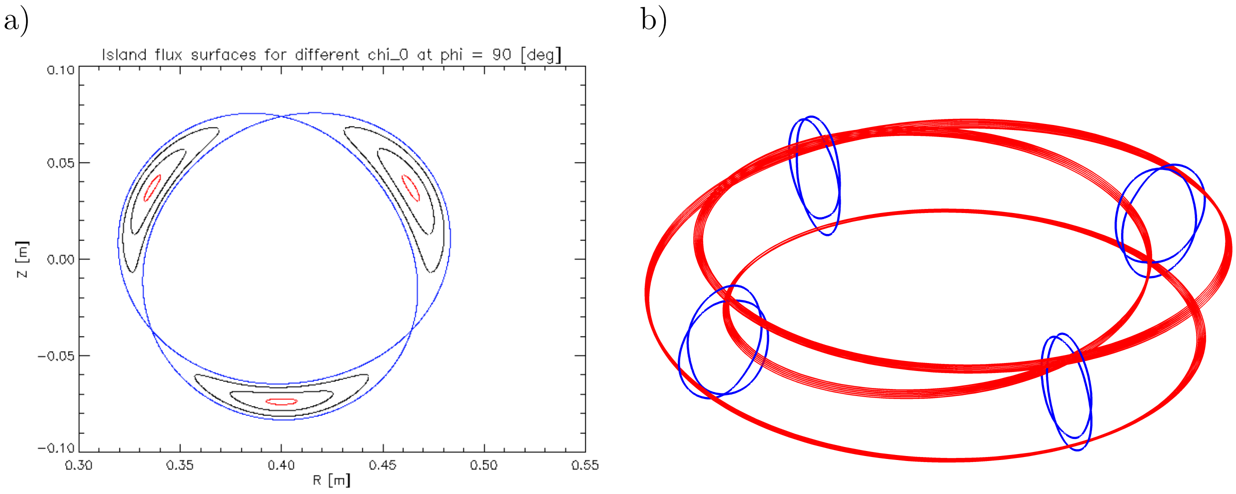

Figure 6.2: Solution of eq. 6.4 for typical GOLEM low q discharge parameters, with island of $m/n = 3/1$ located close to plasma edge. Figure a) – poloidal cros-section view. Figure b) – 3D structure in cartesian coordinates.

In close radial vicinity to resonant surface it is safe to use:

$$B^* \approx -\left(B_\theta \frac{q'}{q}\right)_{r_s} z, \tag{6.3}$$

where $z = (r - r_s)$. By substitution of expressions 6.2-6.3 into relation 6.1, a differential equation in form:

$$-\left(B_\theta \frac{q'}{q}\right)_{r_s} z\mathrm{d}z = r_s \overline{B_r} \sin m\chi \mathrm{d}\chi$$

is obtained, with solution of:

$$z^2(\chi) = \left(\frac{2rq\overline{B_r}}{mq'B_\theta}\right)_{r_s} (\cos m\chi - \cos m\chi_0),$$

$$z(\chi) = \pm\sqrt{\left(\frac{2rq\overline{B_r}}{mq'B_\theta(\chi)}\right)_{r_s}} \operatorname{Re}\left(\sqrt{\cos m\chi - \cos m\chi_0}\right). \tag{6.4}$$

Parameters outside Re operator represent width of island and in first approximation are independent on χ. Of course with exception of B_θ which, as was shown in chapter 4, is due to toroidal effects stronger on inboard side than on outboard side. Thus island width on HFS is smaller than it is on LFS. Quantity χ_0 in eq. 6.4 comes from integration of original differential equation and $\chi_0 \in (0, \frac{\pi}{m})$. For $\chi_0 = \frac{\pi}{m}$, z exists for any χ. If $\chi_0 < \frac{\pi}{m}$,

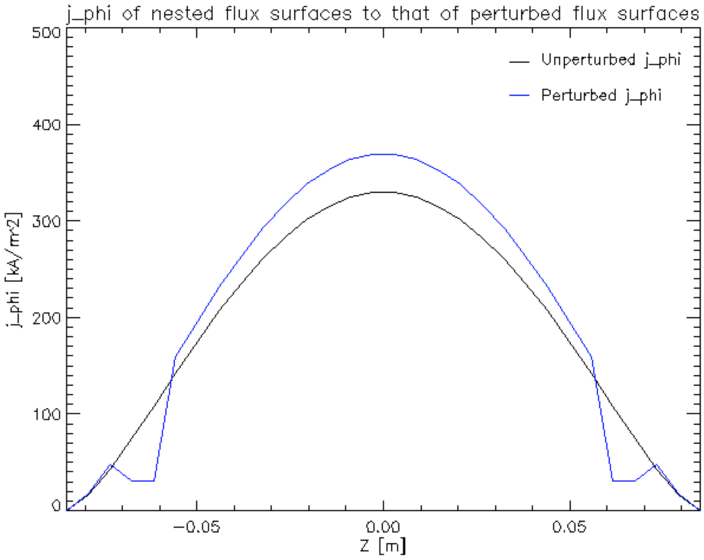

Figure 6.3: Quantity of j_ϕ at $\phi = 0$ across Z coordinate for unperturbed and perturbed field lines respecively. Difference in j_0 is due to normalization of $\int j_\phi \mathrm{d}S = I_p$.

then z is defined only for specific intervals of χ. Relation 6.4 depends on global discharge parameters of plasma column position, I_p, B_ϕ and ν. This is because $z = z(q, q')$, while:

$$q(r) = \frac{2\pi B_\phi}{R\mu_0 I_p} \frac{r^2}{1 - (1 - \frac{r^2}{a^2})^{\nu+1}}$$

as was shown in section 1.2. Solution of eq. 6.4 for $m/n = 3/1$ resonance, using $B_\phi = 0.15$ T, $I_p = 3.5$ kA, $\overline{B_r} = 0.2$ mT and $\nu = 1.5$ is shown in fig. 6.1. The same in (R, Z) poloidal plane or in (x, y, z) coordinates is shown in fig. 6.2 a) and b) respectively. Blue lines represent $\chi_0 = \pi/m$ solution, red lines represent $\chi_0 \to 0$ one and black lines solutions with χ_0 parameter in between these two extremes. From the plot, characteristic structure of island defined by m number is evident, along with dependency of its width along θ coordinate. Centres of red line areas are referred to as *O-point*, while crossings of flux surfaces represented by blue line are referred to as *X-point*.

In plasma in equilibrium where pressure p, temperature T and current density j_ϕ are constant on nested poloidal flux surfaces, presence of X-points has important implications for radial profile of these quantities, since originally disjunctive flux surfaces are connected on these locations. As a refult, [1] refers of flattening of T and p profiles across the island width (provided that this width is sufficiently large). Ref. [31] also reports observations of j_ϕ flattening across the island, using measurements by motional-Stark effect on tokamak

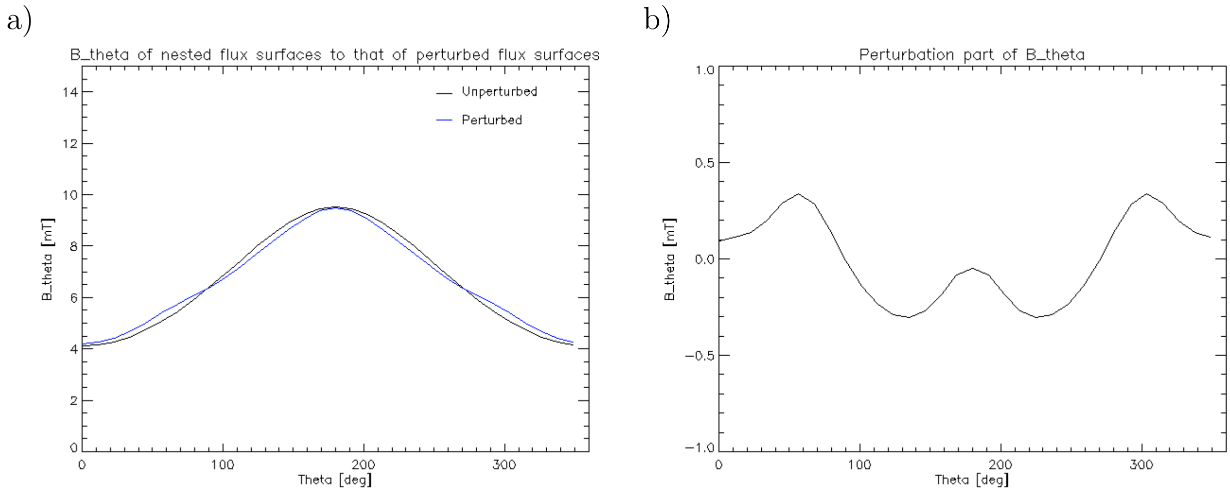

Figure 6.4: Figure a) – B_θ at $r = 0.093$ m for unperturbed and flattened j_ϕ respectively. Figure b) – difference between both results in fig. a).

JT-60U. Thus in first approximation, X-points can be seen as structures that cause short-circuiting of aforementioned quantities across r coordinate.

Of the r profile changes of the quantities above, only the change in j_ϕ is seen by magnetic diagnostics – specifically as B_θ perturbations, induced by flattened $j(r)$. In following model, it is assumed that flattening occurs only inside of boundaries of magnetic island, which are defined as $z(\chi)$ for $\chi_0 = \frac{\pi}{m}$ (i.e. blue line surfaces with X-points). Unperturbed $j_\phi(r)$ follows relation:

$$j_\phi(r) = j_0 \left(1 - \frac{r^2}{a^2}\right)^\nu, \quad \text{where} \quad j_0 = \frac{\nu + 1}{\pi a^2} I_p. \tag{6.5}$$

while flattening itself is assumed as whole volume of island having constant $j_\phi(r) = j(z_{max} + r_s) = j_{flat}$ i.e. of minimal possible value reached by its width. Fig. 6.3 shows both perturbed and unperturbed j_ϕ used in model.

Exploiting toroidal symmetry of unperturbed j_ϕ profile, unperturbed B_θ on locations of ring detection coils can be efficiently calculated from eq. 4.4 and eq. 4.5. Integral properties enable to represent plasma as a single toroidal loop of current I_p. Also, thanks to additivity, the same can be applied for fraction of current present on radii $r \in (0, r_s - z_{max}) \cup (r_s + z_{max}, a)$ (i.e. in most of plasma) in the perturbed case. However, for $r \in (r_s - z_{max}, r_s + z_{max})$, a full 3D approach by Biot-Savart's law in eq. 4.2 must be used due to $j = j(r, \chi)$ dependency imposed by flattening. To numerically solve this

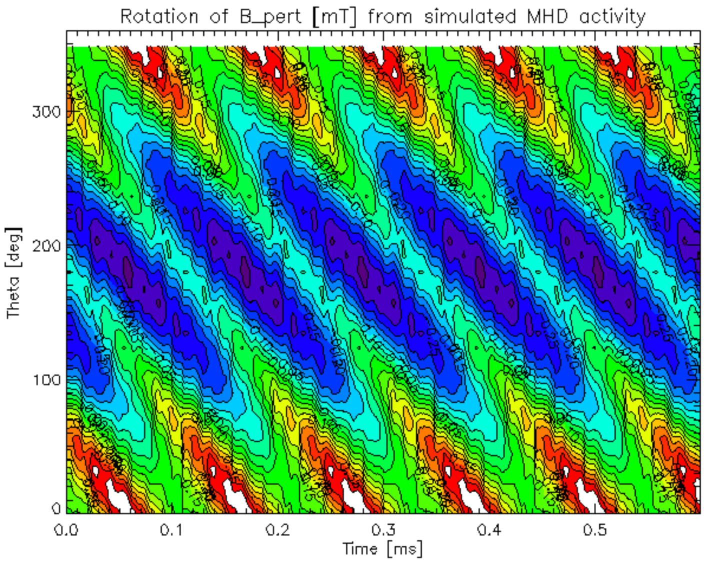

Figure 6.5: Temporal evolution of B_θ perturbations due to plasma poloidal rotation frequency $f_\theta = 3$ kHz.

problem, $r \in (r_s - z_{max}, r_s + z_{max})$ locations need to be transformed into (R, Z) area, which is then discretized into grid. Each of (R_i, Z_i) locations obtained this way represents a toroidal loop. Solution of eq. 6.4 will identify, on which (R_i, Z_i, ϕ) coordinates is $j(R_i, Z_i, \phi) = j_{flat}$ and where is $j(R_i, Z_i, \phi) = j_\phi(r)$ given by eq. 6.5. Then, B_θ detected by sensor located on $(R, Z, \phi = 0)$ is given by:

$$B_\theta = \sqrt{B_R(R,Z) + B_Z(R,Z)}, \tag{6.6}$$

where

$$B_R(R,Z) = B'_R + \frac{\mu_0 dx^2}{4\pi} \sum_i \sum_k j_{ik} dl_{0_i} \frac{(Z_i - Z)\cos\phi_k}{\sqrt{R_i^2 \sin^2\phi_k + (R - R_i\cos\phi_k)^2 + (Z - Z_i)^2}} \tag{6.7}$$

$$B_Z(R,Z) = B'_Z + \frac{\mu_0 dx^2}{4\pi} \sum_i \sum_k j_{ik} dl_{0_i} \frac{(R - R_i\cos\phi_k)\cos\phi_k - R_i\sin^2\phi_k}{\sqrt{R_i^2 \sin^2\phi_k + (R - R_i\cos\phi_k)^2 + (Z - Z_i)^2}} \tag{6.8}$$

Quantities B'_R and B'_Z represent contribution from unperturbed radii of plasma, as calculated by eq. 4.4 and eq. 4.5 respectively. i indexes represent all the (R_i, Z_i) locations mentioned above and k indexes represent discterization of each full toroidal loop located in (R_i, Z_i) into elements dl_{0_i} long and distributed along toroidal angles of ϕ_k. dx represents precision of (R_i, Z_i) grid. Note that for simplicity, whole plasma volume may be discretized into i,k indexes, in which case $B'_R = 0$, $B'_Z = 0$. Using island parameters mentioned above, $B_\theta(r, \theta)$ at $r = r_{det} = 0.093$ m (i.e. where ring coils are located) is shown in fig. 6.4 a) for both perturbed and unperturbed flux surfaces. Fig. 6.4 b) shows difference between these quantities, i.e. perturbation component of B_θ. Calculations imply, that $\frac{\delta B_\theta}{B_\theta} \sim 10^{-1}$ at most.

Also, B_θ perturbation across θ in fig. 6.4 is not stationary in time. In tokamaks, radial electric field is present which, together with B_ϕ field, causes poloidal rotation of plasma due to $E \times B$ drift in negative θ direction:

$$\mathbf{v}_\theta = -\frac{E_r}{B_\phi}\mathbf{i}_\theta.$$

Probe measurements on tokamak GOLEM show that floating potential $\frac{\partial V_{fl}}{\partial r} > 0$ and thus $E_r < 0$. When actual orientation of B_ϕ on this device is taken into consideration – i.e. that of negative ϕ direction, poloidal rotation is indeed in the direction of negative $\mathbf{i}_\theta$. Implementation of e.g. $f_\theta = 3$ kHz rotation into island signal model will yield temporal evolution of B_θ perturbations as shown in fig. 6.5.

Thus, model presented in this section implies that presence of magnetic island manifests itself as $\frac{\delta B_\theta}{B_\theta} \sim 10^{-1}$ fluctuations in both temporal and spatial domain.

6.2 Methods of statistical analysis

6.2.1 Fast Fourier transform

Investigation of frequency domain of signal is standardly carried out with the help of Fourier transform algorithms, as they are optimal for characterization of periodic signals. Continuous forward Fourier transform of function $g(t)$ into $G(f)$ is defined as:

$$G(f) = \frac{1}{\sqrt{2\pi}} \int_{-\infty}^{\infty} f(t)\mathrm{e}^{-\mathrm{i}2\pi f t}\mathrm{d}t,$$

while inverse Fourier transform is in form:

$$f(t) = \frac{1}{\sqrt{2\pi}} \int_{-\infty}^{\infty} G(f)\mathrm{e}^{\mathrm{i}2\pi f t}\mathrm{d}f.$$

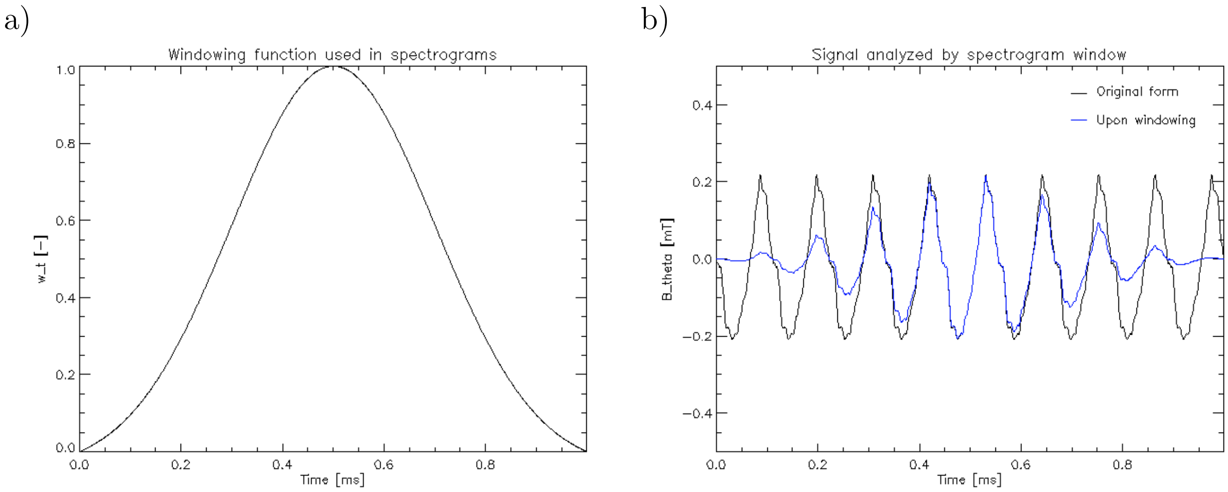

Figure 6.6: Figure a) – Used windowing function for modification of DFT input array. Figure b) – Temporal evolution of B_θ perturbation on fixed θ – original and windowed signal. Fluctuations represent $m/n = 3/1$ magnetic island with poloidal rotation frequency $f = 3$ kHz.

However, in the case of transformation of finite N data points elements, discrete Fourier transform (DFT) is necessary to be used instead:

$$G_k = \frac{1}{\sqrt{N}} \sum_{j=0}^{N-1} g_j \mathrm{e}^{-\mathrm{i}\frac{2\pi}{N}kj},$$

with its inverse form:

$$g_j = \frac{1}{\sqrt{N}} \sum_{k=0}^{N-1} G_k \mathrm{e}^{\mathrm{i}\frac{2\pi}{N}kj}.$$

Original quantity t is connected with index j in following manner:

$$t_j = t_0 + \frac{j}{f_s}$$

where f_s represents sampling frequency of data points and t_0 offset time variable corresponding to time at $j = 0$. Connection of k to frequency f is not as straightforward due to character of the transform and follows relation:

$$f_k = \frac{kf_s}{N_w} \quad \text{for} \quad k \in (0, 1, ..., N_w/2), \tag{6.9}$$

and the same relation for the negative part of k domain:

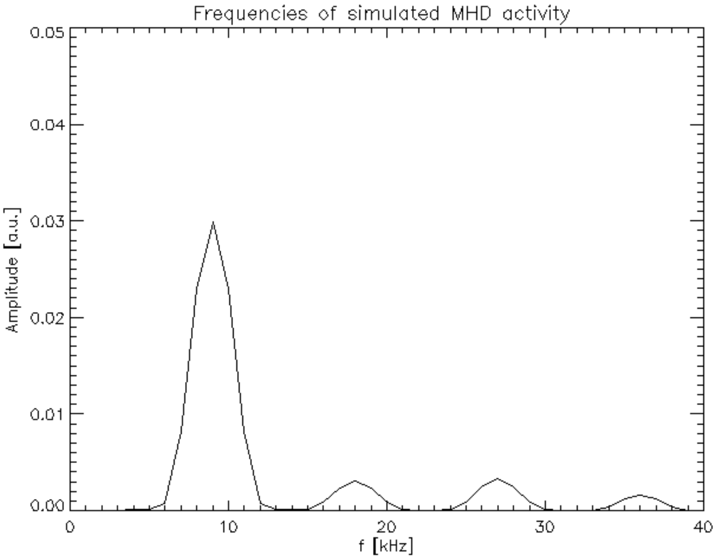

Figure 6.7: Power spectrum of windowed signal in fig. 6.6 b).

$$f_k = \frac{kf_s}{N_w} \quad \text{for} \quad k \in (-N_w/2+1, -N_w/2+2, ..., -1).$$

N_w represents width of window. Input of DFT is generally assumed to be from complex domain. Also, even if input is fully real, the output of DFT is always complex. For investigation of which frequencies are dominant within signal, $|G_k|$ magnitude of obtained coefficients (i.e. *power spectrum*) is used. And since $|G_k| = |G_{-k}|$, use of only first half of output array is sufficient.

Note that t_j and f_k no longer represent continuous quantities, nor are they defined on infinte domains. To extend these domains indefinitely, periodic exrapolation is used for each DFT input array. In that case, it is essential to ensure that $G_0 = G_N = 0$, otherwise an infinite amount of discontinuities with index periodicity of N would be present in DFT input. Note that in this context *discontinuity* refers to analogy with continuous Fourier transform, where all the frequencies from interval $f \in (-\infty, \infty)$ are necessary to fully characterize analytical discontinuity. Due to periodical repetition of discontinuities at the beginning and end of analyzed signal window, in DFT a so-called *leakage of frequencies* takes place. This manifests as presence of virtual frequencies of non-negligible $|G_k|$ magnitudes, which can be prevented by windowing of input array. The most commonly used windows are Hanning and Gaussian ones, and generally have

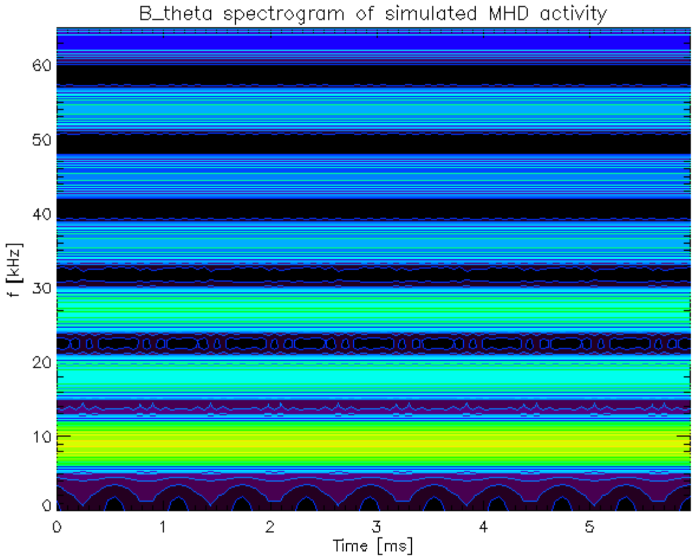

Figure 6.8: Spectrogram of signal in fig. 6.6 b) (the unwindowed one) being periodically repeated after each 6 ms. Time window in spectrogram was chosen to be 1 ms long, windowed by function in fig. 6.6 and overlapped on 95 % of its width from both sides.

properties of $W_0 = W_{N-1} = 0$ and $W_{N/2} = 1$. In this thesis, windowing function of

$$w_t(j) = \mathrm{e}^{-\frac{a_w^2}{2}\left(1-2\frac{j}{N_w}\right)^2} \tag{6.10}$$

was used. a_w is control parameter and j represents data point index. See fig. 6.6 a) for specific form of used w_t. Application of windowing on temporal evolution of B_θ for detector on fixed θ coordinate is shown in fig. 6.6 b).

The most common algorithm of DFT calculation is that of *fast Fourier transform* (FFT). It works with $N = 2^k$ long windows, which enables its optimalization to only $N \log N$ numerical operations being necessary for calculation (intead of N^2). If number of elements of input array is other than power of 2, the array is extended with such number of zero signal data points, as to fulfill $N = 2^k$ condition. Application of FFT on windowed B_θ perturbation signal in fig. 6.6 b) is shown in fig. 6.7. Note that $f_s = 1$ MHz, thus power spectrum goes up to $f_{Nyquist} = 500$ kHz. However, only non-negligible $|G_k|$ were those which corresponded to frequencies below 40 kHz.

Modelled island is of $m/n = 3/1$ structure and with poloidal rotation frequency of $f = 3$ kHz. However, fig. 6.7 identifies major peak at 9 kHz and some minor peaks at 18,27 and 36 kHz respectively. From fig. 6.5 it can be seen that presence of main peak at

9 kHz is due to spatial structure of island – althought each field line rotates poloidally at 3 kHz, it is projected to poloidal plane m times in total. Therefore, poloidal frequency rotation of island is calculated:

$$f = \frac{f_{max}}{m} \, .$$

In order to vizualize temporal variations of power spectrum, *spectrogram* needs to be generated. In that case, data are divided among multiple time windows of the same width and FFT is applied on each of them separatedly. Every output array then represents power spectrum of signal for different moment in time. Since each input array needs to be windowed, it is favourable to make the windows overlap each other as to prevent loss of information. However, use of standard spectrograms always comes with dilemma in choice of N_w. To obtain the best temporal resolution, smallest possible N_w is favourable. On the other hand, relation 6.9 says that low N_w will result in bad frequency resolution and that highest possible N_w should be used. Althought high-degree overlapping of windows will improve the temporal resolution by some degree, combined (averaged) effect of all the events present across the whole window width is always analyzed. A spectrogram for magnetic island in presented model is shown in fig. 6.8.

6.2.2 Correlation analysis

Unlike Fourier transform, correlation method is not principally intended for analysis of periodical events. Rather, it quantifies similarity of two general signals x and y as a function of their lag L. Quantity L has dimension of index and its meaning can seen from definition of *cross-correlation coefficient* of x and y:

$$P_{xy}(L) = \frac{\sum_{k=0}^{N-|L|-1} (x_{k+|L|} - \bar{x}) \cdot (y_k - \bar{y})}{\sqrt{\left[\sum_{k=0}^{N-1} (x_k - \bar{x})^2\right] \cdot \left[\sum_{k=0}^{N-1} (y_k - \bar{y})^2\right]}} \quad \text{for} \quad L < 0,$$

and

$$P_{xy}(L) = \frac{\sum_{k=0}^{N-L-1} (x_k - \bar{x}) \cdot (y_{k+L} - \bar{y})}{\sqrt{\left[\sum_{k=0}^{N-1} (x_k - \bar{x})^2\right] \cdot \left[\sum_{k=0}^{N-1} (y_k - \bar{y})^2\right]}} \quad \text{for} \quad L > 0.$$

If input vectors x and y represent discretized temporal evolution of a physical quantity sampled at f_s frequency, then L is related to shift in time in following manner:

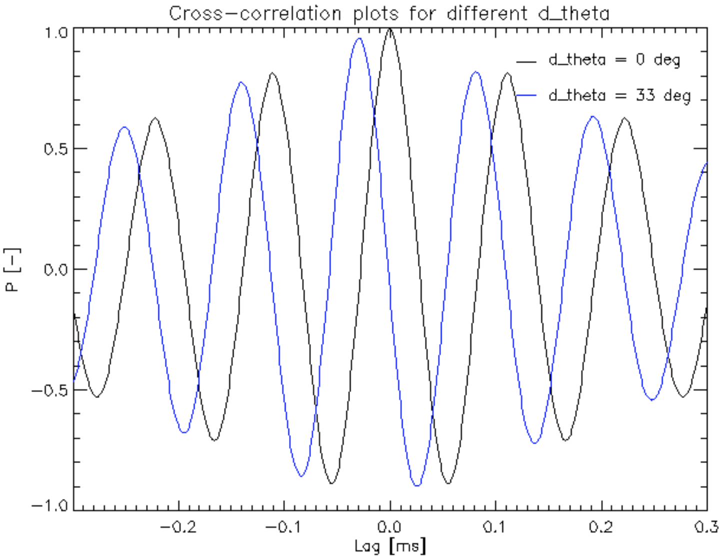

Figure 6.9: Cross-correlation coefficient of signal from fig. 6.6 b) to signal poloidally shifted by $\delta\theta = 0$ (i.e. autocorrelation) and by $\delta\theta = 33$ deg.

$$\tau_L = \frac{L}{f_s}$$

Overlined quantities $\bar{x}$ and $\bar{y}$ represent mean values of input vectors. Numerator in P_{xy} definition is equal to cross-covariance of x and y vectors while denominator represents geometrical average of input array variances (respective $\frac{1}{N}$ coefficients cancelled each other). Thus $P_{xy} \in (-1, 1)$.

From P_{xy}, both similarity and temporal shift of signals x and y are quantified at the same time. Unlike DFT, cross-correlation analysis does not require windowing of input array and output is inherently from real domain. Correlation coefficient of modelled signal in fig. 6.6 b) (the one without windowing) to itself as a function of τ_L is plotted in fig. 6.9, together signal of B_θ perturbations on locality poloidally shifted by $\delta\theta = 33$ deg. Then, correlation coefficients of signal in fig. 6.6 b) to all the signals across θ are plotted in fig. 6.10. By comparison to fig. 6.5 of original temporal evolution of the signals, it can be seen that outputs normalized to $(-1, 1)$ interval do not accomodate constant offset as original signals did. Also, temporal evolution of output is smoothed, since only signal time shift is of matter to cross-correlation analysis and not actual shape of perturbation signal. m mode number of island is obtained by counting number of maxima or minima of P_{xy} present at the same time – see fig. 6.10 for details.

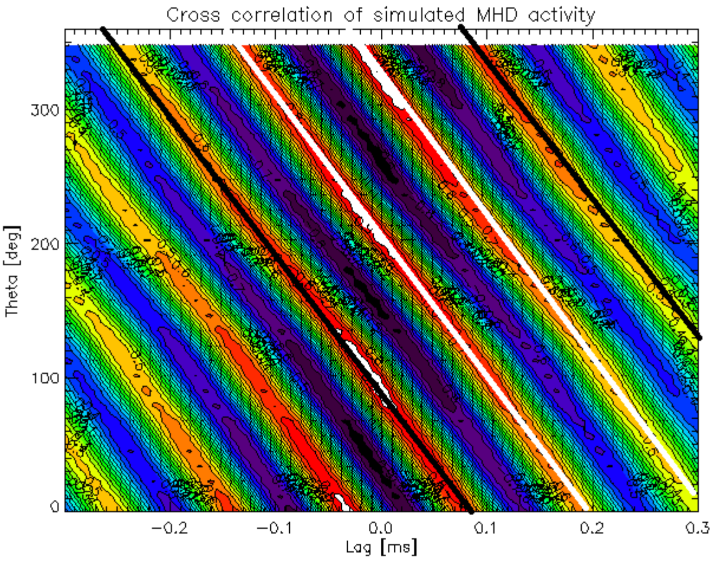

Figure 6.10: Cross-correlation coefficients of signal from fig. **??** to all the signals across θ coordinate. Original form of these signals is shown in fig. 6.5. Black lines trace the same field line. Fig. implies that $m = 3$.

Also, it is possible to identify frequency of island poloidal rotation as:

$$f = \frac{1}{m\Delta\tau},$$

where $\Delta\tau$ is time lag between two maxima of auto-correlation coefficient (or of any cross-correlation coefficients). This method yields $f = 3.084$ kHz, which is not that far from an actual rotation frequency of 3 kHz.

Another way how to visualize output of cross-correlation analysis besides that shown in fig. 6.10 is by use of *polar plot*. By choosing an arbitrary τ_L and calculating P_θ for this single moment across θ, spatial distribution of cross-correlation coefficients is obtained. This is equivalent to single vertical line in fig. 6.10, with temporal location at value of chosen τ_L. In polar plot, θ retains its meaning, while P_θ is transformed into radius r by relation:

$$r(\theta) = a_1(P_\theta + a_0). \tag{6.11}$$

Coefficient $a_0 > 1$ prevents presence of negative radii, while a_1 defines unperturbed radius as $r_0 = a_1 a_0$. Thus $r(\theta) \in (a_1(a_0 - 1), a_1(a_0 + 1))$. Then, transformation $(r, \theta) \rightarrow (R, Z)$

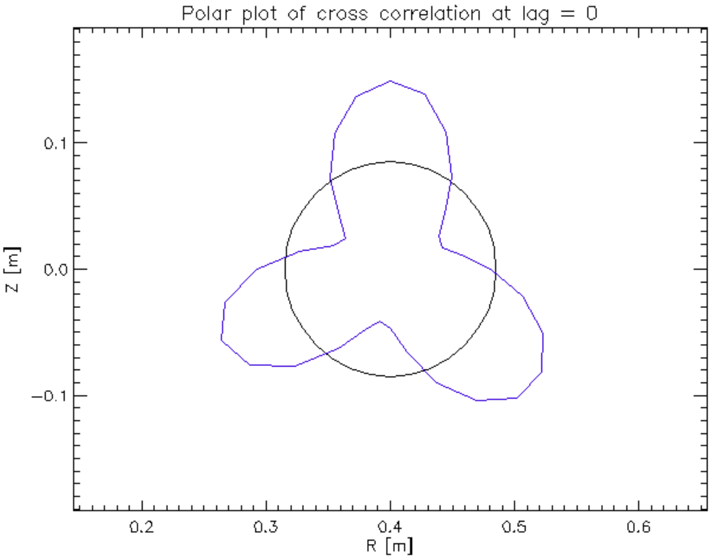

Figure 6.11: Cross-correlation coefficients of signal from fig. 6.10 at lag $\tau_L = 0$ in form of polar plot. Black line represents 0 value of cross-correlation coefficients.

takes place, and by plotting obtained curve along with the one for $r(\theta) = r_0$ (see fig. 6.11), $m = 3$ island structure can be seen.

Chapter 7

Observed MHD structures on tokamak GOLEM

In section 6.1 it was shown how MHD structures cause perturbations of B_θ in (θ, t) domain. Section 6.2 referred how principal parameters of these structures can be obtained by application of methods of statistical analysis, specifically by FFT and cross-correlation methods. In this chapter, MHD structures of tokamak GOLEM plasma are investigated by analysis of B_θ perturbations detected by ring coils. In order to observe magnetic islands under different conditions, several different systematic experimantal sessions took place. However, since MHD structures are present only on specific frequencies in B_θ signal and since optimal conditions for presence of large MHD structures are different from standard GOLEM discharges, section 7.1 describes specifications of experimental conditions and data analysis during these sessions. The principal findings of investigation are summarized in section 7.2 on several representative samples of islands.

7.1 Analysis of magnetic islands

Magnetic islands of m/n structure are generated by tearing instability on r_s resonant surface radius, defined by $q(r_s) = \frac{m}{n}$ (see section 1.2) where

$$q(r) = \frac{2\pi B_\phi}{R\mu_0 I_p} \frac{r^2}{1 - (1 - \frac{r^2}{a^2})^{\nu+1}} \,. \tag{7.1}$$

In fact, $q(r) = q(r, t)$, since $I_p = I_p(t)$, $B_\phi = B_\phi(t)$ and principally even $\nu = \nu(t)$ (althought this quantity cannot be measured on GOLEM yet). Moreover, plasma radius

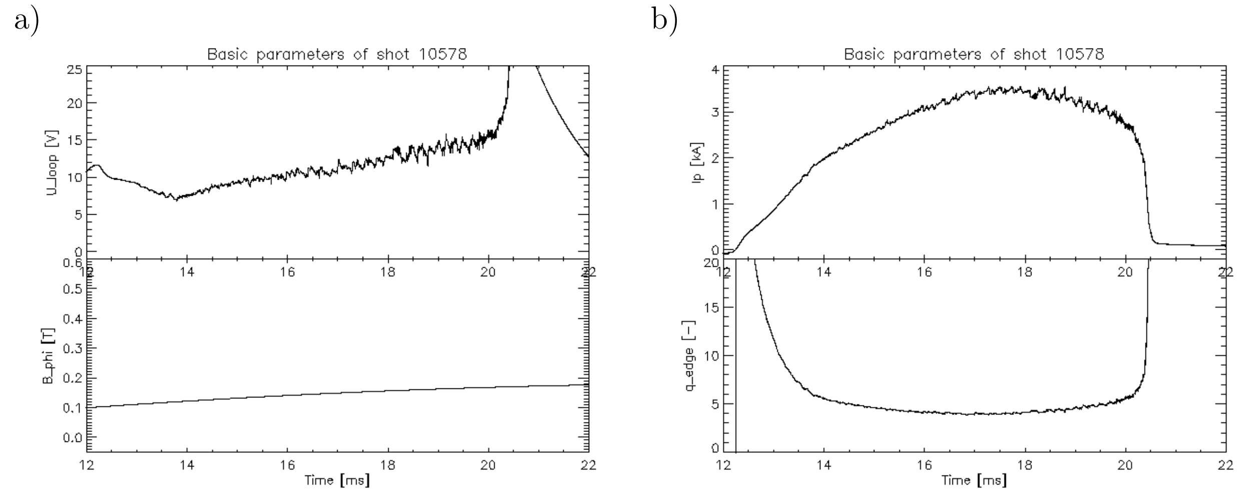

Figure 7.1: Global parameters of low $q(a)$ GOLEM discharge. Figure a) – poloidal loop voltage U_{loop} and B_ϕ toroidal magnetic field. Figure b) – total plasma current I_p and $q(a)$.

is a function of plasma position (R, Z):

$$a = a_0 - \sqrt{(R - R_0)^2 + Z^2},$$

where a_0 represents limiter radius and R_0 major radius of tokamak. Additionally, eq.7.1 explicitly depends on R coordinate of plasma center. However, since proper reconstruction of plasma position is not yet implemented on GOLEM, and since estimations of this position can provide only general trend at most (see fig. 5.6), for q calculation it is assumed that $(R, Z) = (R_0, 0)$ (thus $a = a_0$). Also, due to high degree of stochastic plasma fluctuations on tokamak GOLEM, only low m and n number islands with r_s close to a can be detected. Thus quantity of

$$q(a_0, t) = \frac{2\pi a_0^2}{R_0 \mu_0} \frac{B_\phi(t)}{I_p(t)} \tag{7.2}$$

is used as relevant discharge parameter for characterization of MHD conditions. This also enables to avoid using unknown quantity of ν. This quantity is needed only for specification of island r_s, when $\nu = 1.5$ is assumed. Besides $q(a, t)$, general discharge parameters of U_{loop} (detected by ψ flux loop from section 2.3.1), B_ϕ (detected by B_ϕ coil from section 2.3.4) and I_p (detected by Rogowski coil from section 2.3.2) are monitored as well. However, as can be seen from fig. 1.8, typical GOLEM operational parameters yield too high $q(a)$ values for generation of low m/n magnetic islands and thus discharges

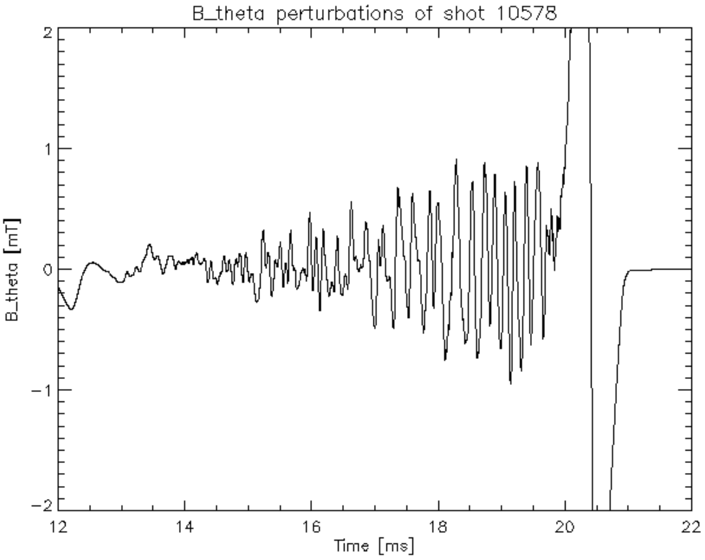

Figure 7.2: Temporal evolution of typical B_θ perturbations for low-q discharge. Obtained using band-pass filter of $f \in (1, 20)$ kHz.

of low B_ϕ and high I_p are necessary for MHD studies – see fig. 7.1.

Some of following discharges applied vertical plasma position stabilization. In such shots, Lorentz force from I_p and B_R (generated by external windings in fig. 4.8 a)) counteracts upwards drift of plasma column (as demonstrated in section 5.2). There, dz quantity estimated by relation 5.1 and using signals of old Mirnov coils (processed with eq. 5.6) as an input is plotted. Since generated B_R varies across (R, Z) plane, I_c current per turn of winding is plotted instead. B_R distribution across (R, Z) can be then obtained by multiplication of I_c with results in fig. 4.8 b) or c) (depending on degree of core saturation).

In fig. 6.4 of section 6.1, B_θ perturbation was obtained by subtraction of unperturbed B_θ from total B_θ. However, for real B_θ a more robust approach by using a digital filter is necessary. A simple low-pass filter can be obtained by smoothing the signal by method of box-car average. If N_w represents index width of averaging window, then it is straightforward to show that all the frequencies above

$$f_{cut} = \frac{f_s}{N_w}$$

are eliminated from smoothed signal. High-pass filter is then obtained by subtraction of smoothed signal from original one. A combination of the two – *band-pass filter* is obtained in following way: Let x be input quantity and $\mathrm{avg}(x, N_w)$ its form smoothed by

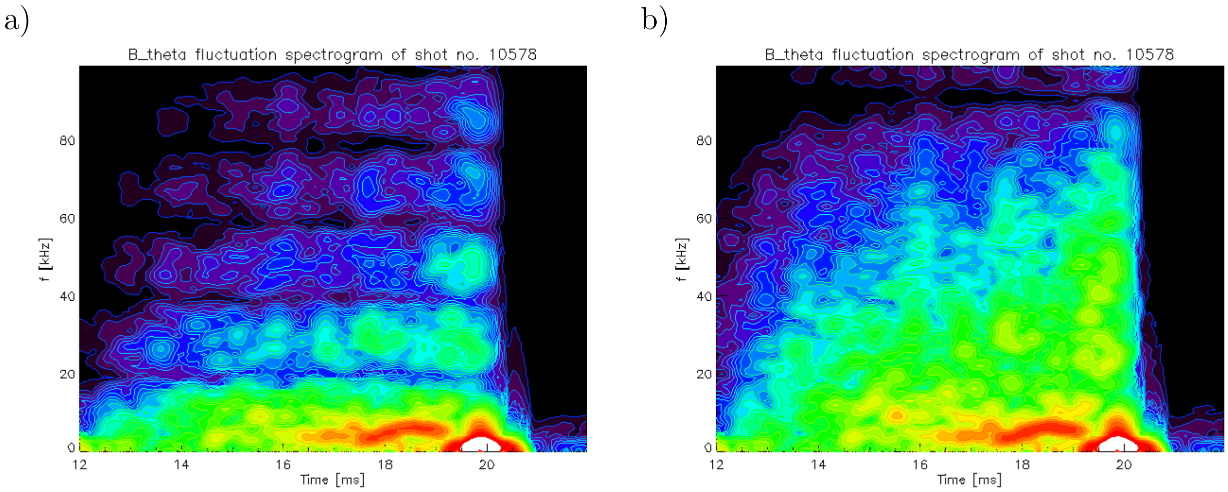

Figure 7.3: Spectrogram of B_θ fluctuations in fig. 7.2. Figure a) – band-pass filter of $f \in (1, 20)$ kHz applied. Figure b) – band-pass filter of $f \in (1, 100)$ kHz applied.

window of N_w data points length. Quantity of

$$y = \text{avg}\left(x - \text{avg}(x, N_{w1}), N_{w2}\right)$$

then represents signal of range $f \in (\frac{f_s}{N_{w1}}, \frac{f_s}{N_{w2}})$. Literature [32] and [1] refers that typical frequencies of MHD structures are in $f \in (1, 10)$ kHz range. In some cases on GOLEM is observed rotation faster than that, thus $f \in (1, 10)$ kHz pass was used, assuming $f_s = 1$ MHz, $N_{w1} = 1000$ and $N_{w2} = 50$. As a result temporal evolution of B_θ perturbations is obtained – see fig. 7.2. Spectrogram of such data is shown in fig. 7.3 a). For comparison, spectrogram for filter of $f \in (1, 100)$ kHz is shown in fig. **??** b). As can be seen, even thought $f \in (1, 20)$ kHz filter did not completely negate frequencies above 20 kHz, they are signifiantly mitigated at the very least. To prevent data loss thought, wide-band pass filters are used to characterize temporal evolution of B_θ fluctuations in spectrograms and perturbation plots, while narrow-band pass filters are applied to study specific frequencies across chosen time windows for analysis of island properties.

As can be seen in fig. 7.3, on time interval of (17.5,19.5) ms, a strong low-frequency fluctuation was present. The same is also evident in fig. 7.2, making this phenomenon a candidate for being a rotating MHD structure of magnetic island. Plot of B_θ perturbations across (θ, t) space over small window of (17.4,17.8) ms in fig. 7.4 a) and its respective correlation profile in fig. 7.4 b) (or its polar form in fig. 7.5 b)) imply presence of $m = 3$ magnetic island. Application of FFT in fig. 7.5 a) yields dominant

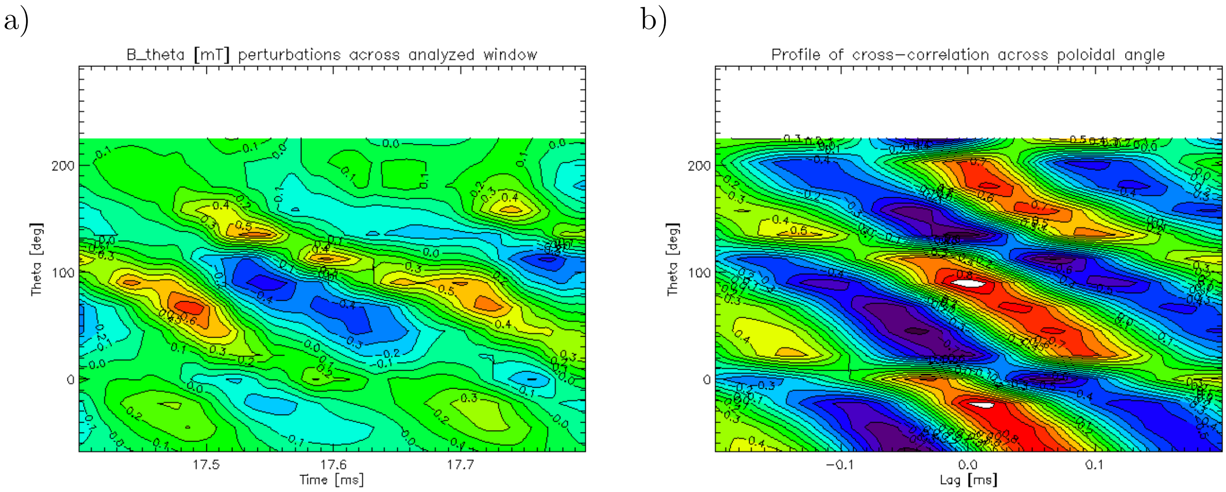

Figure 7.4: Figure a) – B_θ perturbation plot across whole θ and temporal window of (17.4,17.8) ms. Band-pass of $f \in (1, 20)$ kHz used. Figure b) – cross-correlation profile of data in figure a). Ring coil 5 is taken as reference.

frequency of $f_{max} = 5.012$ kHz, thus poloidal rotation of observed MHD structure being $f = \frac{f_{max}}{m} = 1.67$ kHz. If $\nu = 1.5$ is assumed, then relation 7.1 yields $\frac{r_s}{a} = 0.82$, i.e. island is close to edge of plasma. This is expected, since across the analyzed window, $q(a) = 3.99$ in average. Relation

$$v_\theta = 2\pi f r_s$$

yields velocity of island poloidal rotation $v_\theta \approx 0.73$ km/s.

At this point, it should be noted that estimation of $n = 1$ was applied in the analysis above. Althought there is no toroidally oriented detection array for direct measurement of n on GOLEM, it can be clearly seen from $q(r)$ profile plot in fig. 7.6 that $q(r_s) = m/n = 3/2$ resonant surface is not present anywhere in plasma. Even if possibility of higher ν and lower a (the latter due to plasma position shift) is taken into consideration, r_s for 3/2 island would still be very close to plasma center.

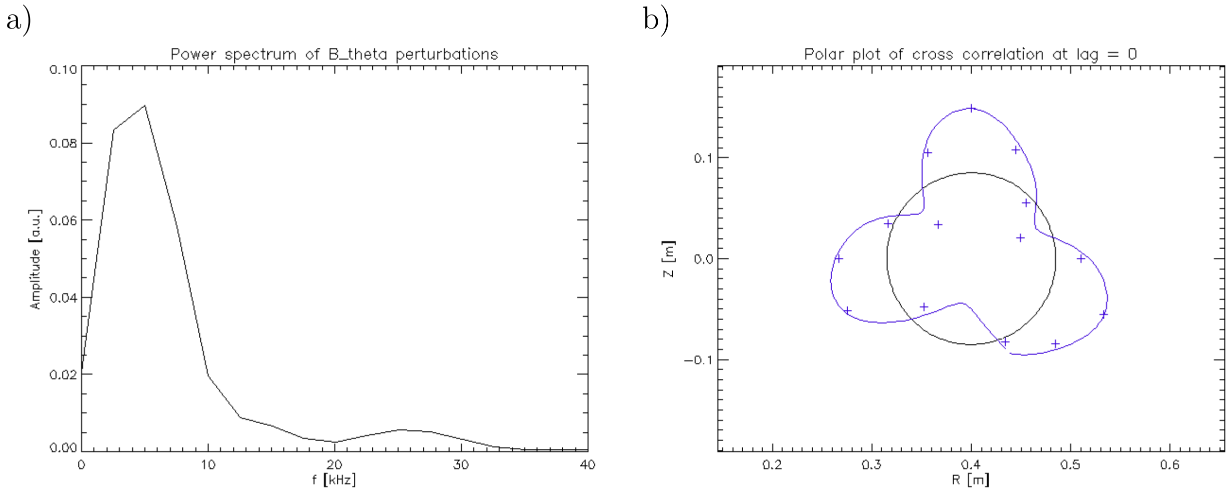

Figure 7.5: Figure a) – power spectrum of B_θ perturbations in fig. 7.2 across analyzed time window. Dominant frequency $f = 5.012$ kHz. Figure b) – polar plot (see eq. 6.11) of cross-correlation coefficient across center of window in fig. 7.4.

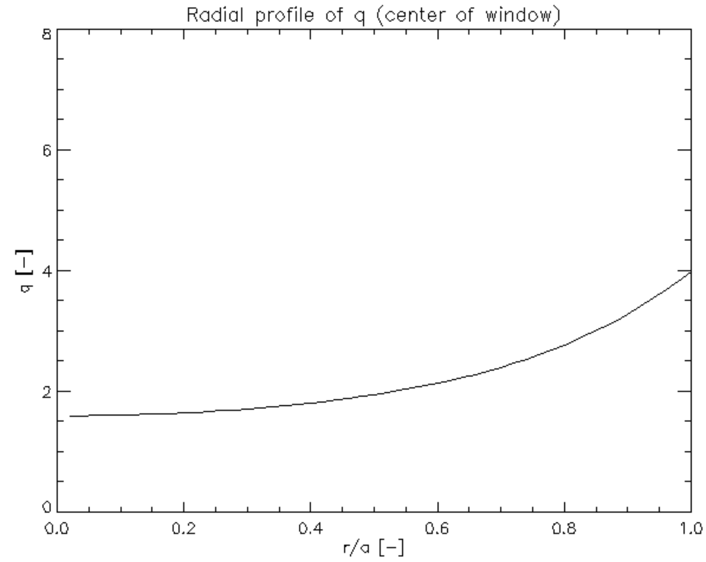

Figure 7.6: $q(r)$ profile for center of analyzed window.

7.2 Island rotation frequency change due to $q(a,t)$

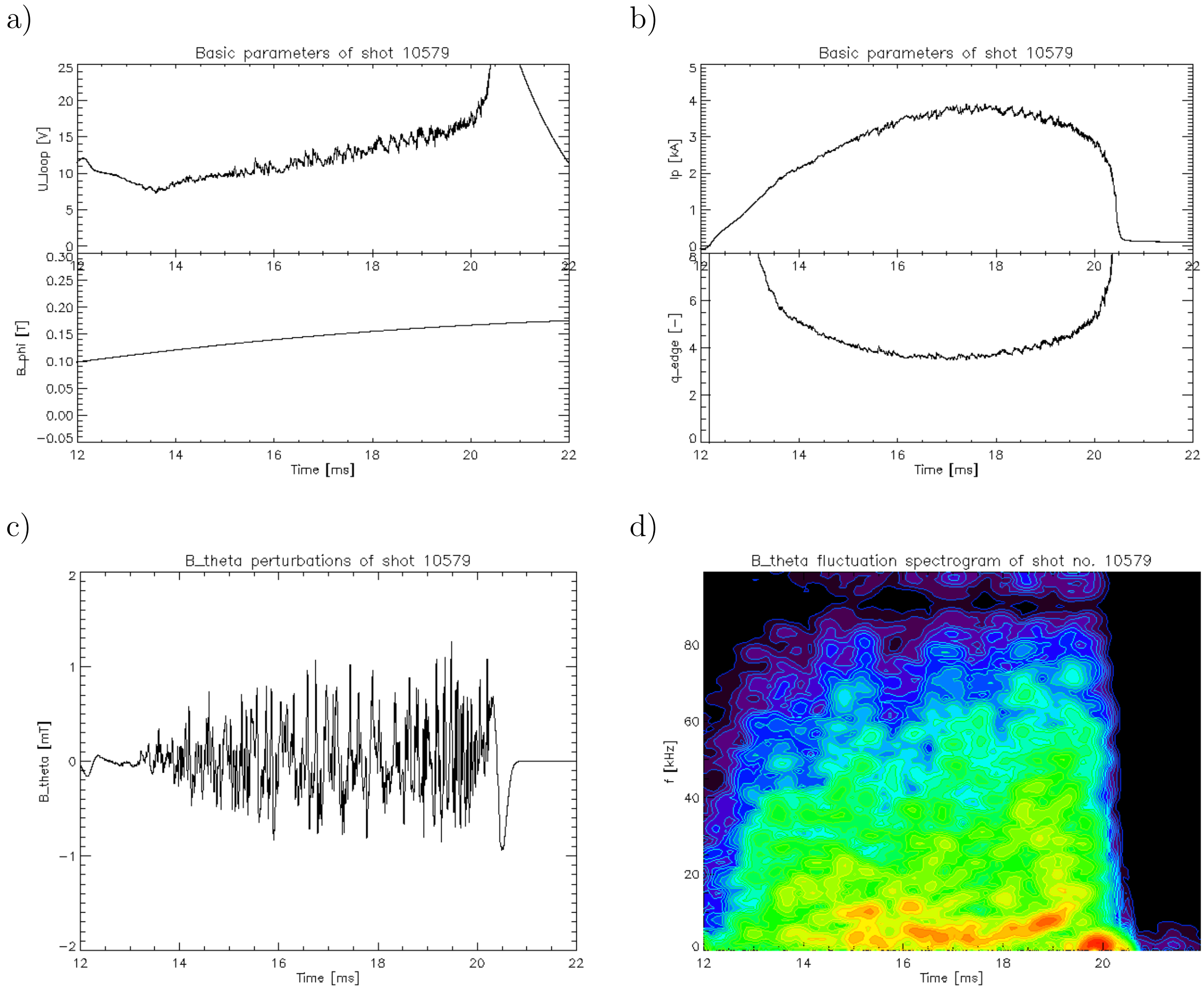

Figure 7.7: Global parameters of analyzed discharge. Fig. a) – U_{loop} and B_ϕ. Fig. b) – I_p and $q(a)$. Fig. c) – B_θ perturbations inside $f \in (1, 100)$ kHz band. Fig. d) – spectrogram of fig. c) data.

Compared to previous discharge, shot no. 10579 has higher I_p, yielding slightly lower $q(a)$ (see fig. 7.7). In this case, B_θ spectrogram in fig. 7.7 d) suggests presence of dominant perturbation on (16.0,19.5) ms interval. However, it can be seen that frequency of this perturbation is a function of time. Comparison with fig. 7.7 b) implies that this change is correlated with that of $q(a)$ – its frequency is initially deccellerated until plateau of $q(a)$ occurs, where f remains constant. Once q starts to rise, so does the frequency. However, at the end of discharge, magnetic islands tend to slow down their rotation due to interaction with eddy currents of tokamak chamber and thus observed of increase of

f was unexpected. Moreover, this is not an isolated case, but typical representation of perturbation behavior at low q GOLEM discharges.

An explanation of this effect requires closer investigation of signal across smaller time windows. Analysis of (17.1,17.8) ms window from the center of structure occurence (using band-pass of $f \in (2, 25)$ kHz) in fig. 7.8 reveals presence of $m = 3$ island. Across this window, average $q(a) = 3.63$. Relation 7.1 yields that $r_s/a = 0.9$, i.e. island is virtually at the edge of plasma and that $n = 1$ due to the same reasons as described in section 7.1. FFT reveals dominant frequency of $f_{max} = 4.29$, kHz thus $f = f_{max}/m = 1.43$ kHz in reality. Poloidal velocity of island rotation is then $v_\theta = 0.687$ km/s.

Analysis of (18.6,19.2) ms window of B_θ perturbations, i.e. right before the disappearance of island (see spectrogram in fig. 7.7), using band-pass of $f \in (2, 30)$ kHz yields $f = 1.82$ kHz. Due to $q(a) = 4.1$ the island is now deeper in plasma on $r_s/a = 0.82$. In this case $v_\theta = 0.797$ km/s, which is relatively close to value of $v_\theta = 0.687$ km/s from previous window – if island stayed on $r_s/a = 0.82$ surface (but kept his increased f), its v_θ would be even higher – 0.874 km/s.

Thus it seems that observed correlation of f to $q(a)$ in fig. 7.7 is given by resulting radial motion of island resonant surface and by simultaneous (partial) conservation of v_θ. One possible explanation of this would be that for edge plasma on tokamak GOLEM are v_θ magnitudes connected to respective flux surfaces. Magnetic island is always bound to specific resonant flux surface, thus its v_θ in that case would be seen as (close to) contant. Other possible explanation would be that v_θ itself is constant across the edge plasma of tokamak GOLEM. This is supported by rake probe measurements which have shown that over edge plasma $E_r =$ const. However, since these measurements correspond to high-q discharges, joint experiment to measure v_θ by both rake probe and ring coils is suggested in future in order to shed more light into this matter.

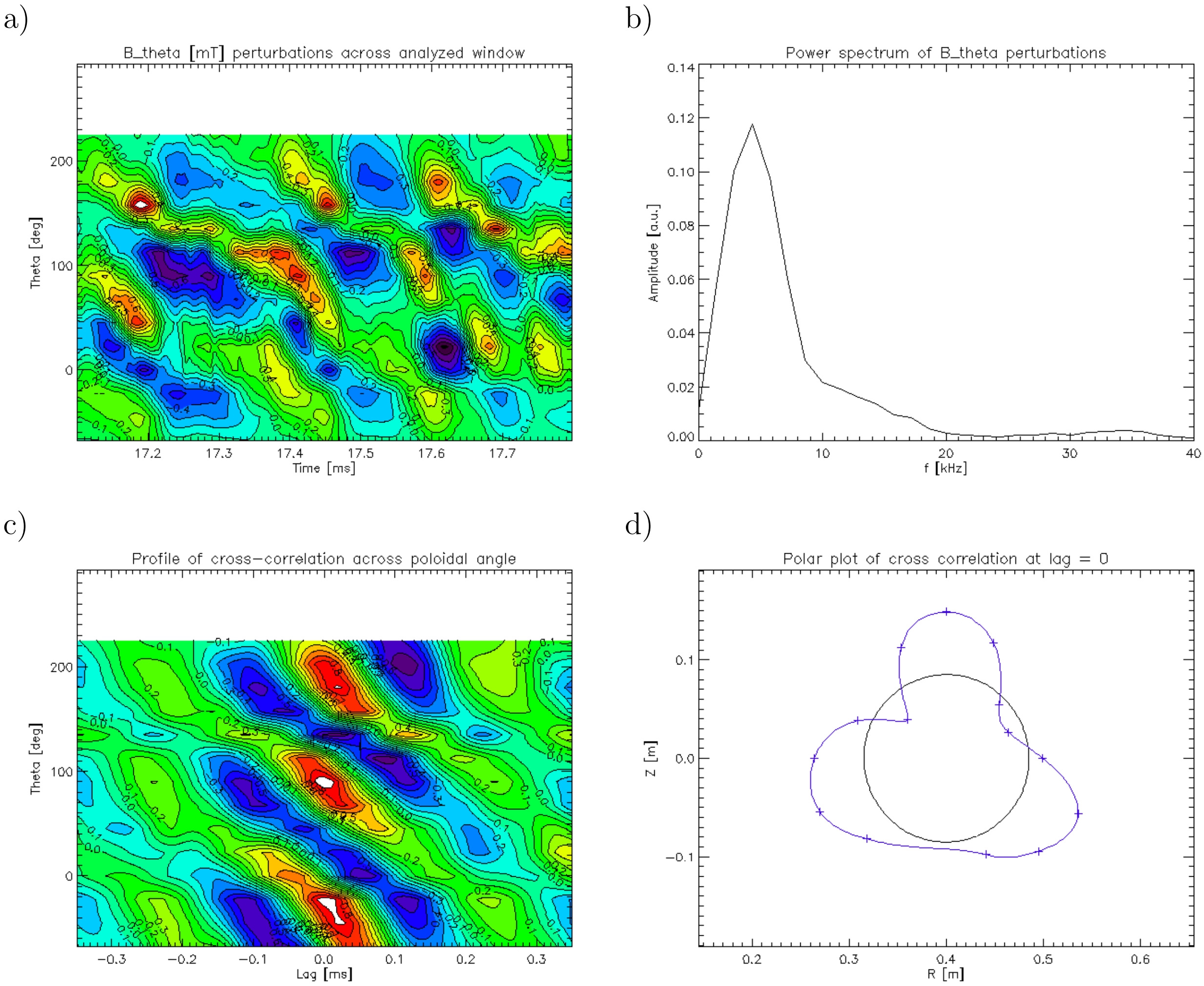

Figure 7.8: B_θ perturbations with $f \in (2, 25)$ kHz band-pass applied. Figure a) – signal profile. Figure b) – signal power spectrum. Figure c) – cross-correlation profile. Figure d) – polar plot of fig. c) at lag = 0.

7.3 v_θ of high m island

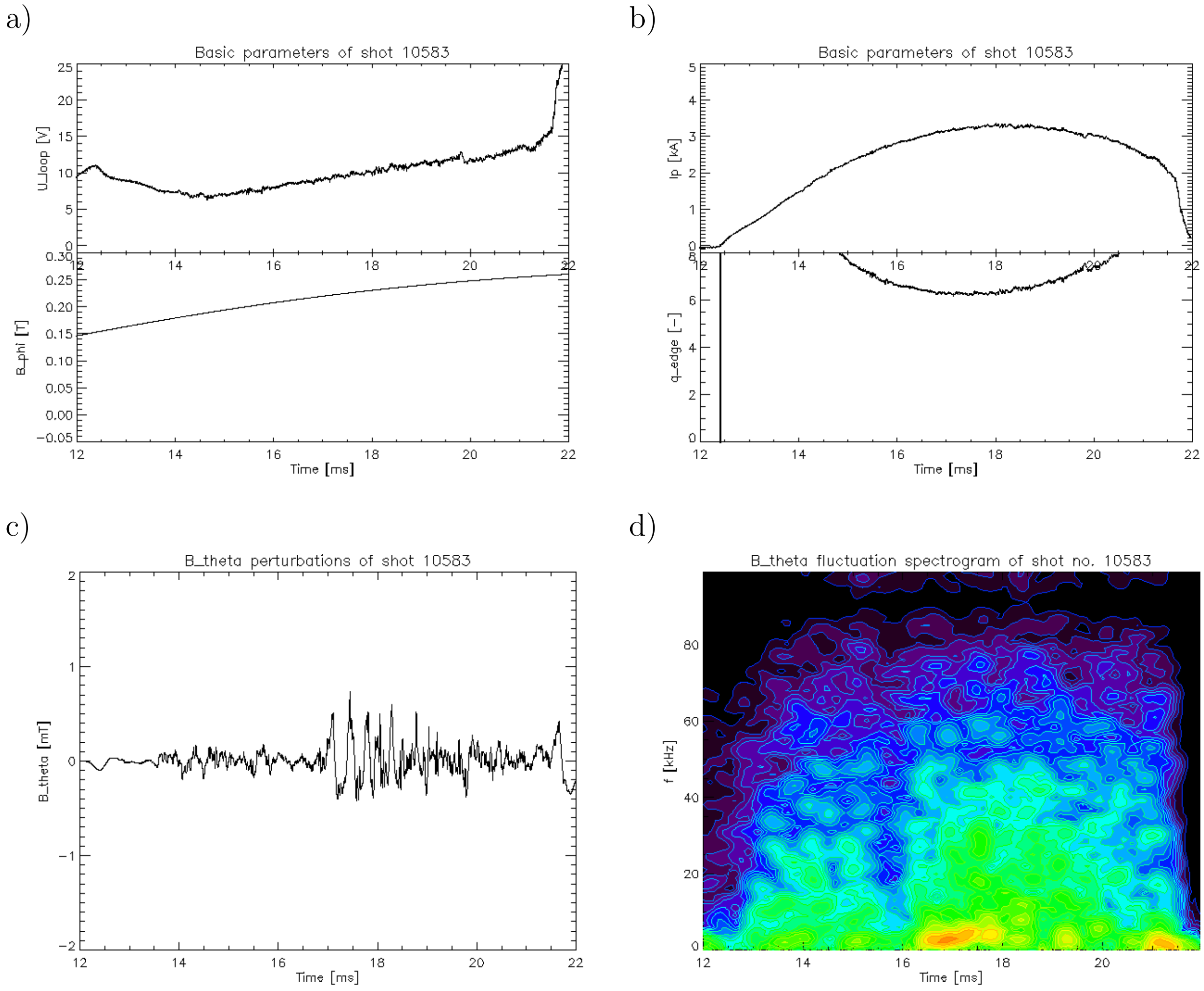

Figure 7.9: Global parameters of analyzed discharge. Fig. a) – U_{loop} and B_ϕ. Fig. b) – I_p and $q(a)$. Fig. c) – B_θ perturbations inside $f \in (1, 100)$ kHz band. Fig. d) – spectrogram of fig. c) data.

For this specific discharge, $q(a) > 6$ at all time, due to higher B_ϕ and of lower I_p – see fig. 7.9. It can be seen in fig. 7.9 c) that level of B_θ perturbations of such a discharge is relatively low (compared to fig. 7.1 c) and fig. 7.7 c)). Moreover, perturbation only take place within (16.5,18.0) ms interval.

Closer look on signal across (16.95,17.80) ms window, using band-pass of $f \in (1, 30)$ kHz (see fig. 7.10 a)) shows perturbative character of low magnitude and high spatial periodicity. Application of FFT and cross-correlation (figures 7.10 b) and c-d) respectively) identifies this structure as a $m = 5$ magnetic island of $f = f_{max}/m = 0.47$ kHz frequency of rotation. Since $q(a) = 6.27$, once again $n = 1$. Resulting radial location of $r_s/a = 0.86$ situates island to edge plasma region, resulting in $v_\theta = 0.215$ km/s.

For $m = 3$ located in the same region, $v_\theta \approx 0.7$ km/s – see section 7.1 and section 7.2, in contrast to observed v_θ for $m = 5$ island. Moreover, this seems to be systematic across experimental sessions – detected v_θ of inherent island rotation was observed to decrease with its m. Since all of the islands in question were located in edge plasma region, possible explanation might be that v_θ is connected with global plasma parameters such as I_p and B_ϕ. Another explanation might be due to interaction of island in edge plasma with conductive tokamak wall which might be more efficient for higher m islands.

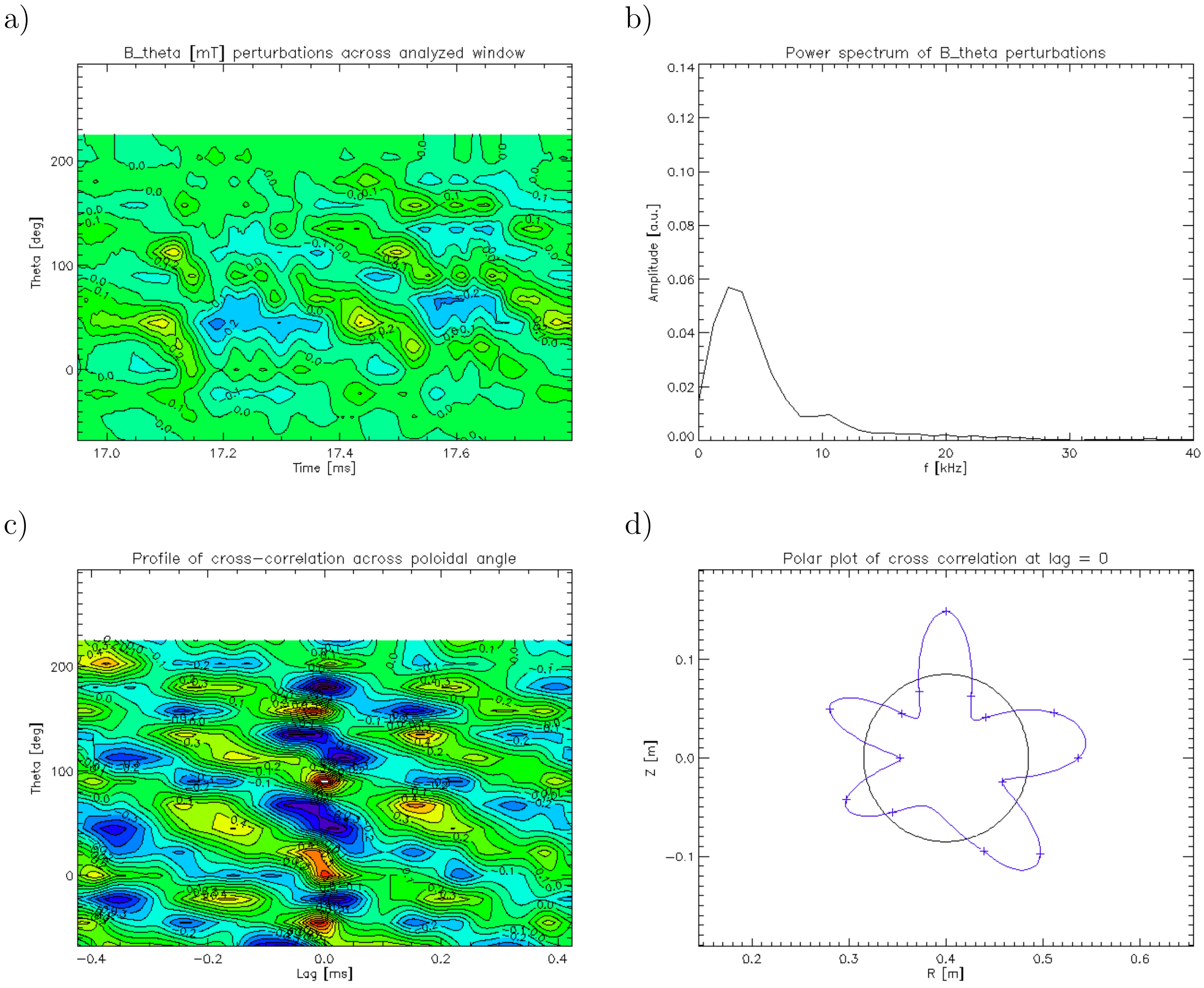

Figure 7.10: B_θ perturbations with $f \in (1, 30)$ kHz band-pass applied. Figure a) – signal profile. Figure b) – signal power spectrum. Figure c) – cross-correlation profile. Figure d) – polar plot of fig. c) at lag = 0.

7.4 v_θ acceleration by external B_R field

It was shown in section 5.2 that plasma column drifts towards top of the chamber, unless external B_R field is applied. Stabilization was not used for shots analyzed in sections 7.1 and 7.2, thought. As can be seen in fig. 7.11 e), by energizing vertical plasma stabilization windings (shown in fig. 4.8), upwards drift of plasma column was prevented in this discharge. Global parameters in fig. 7.11 a) and b) are similar to those under which $m = 3$ island was detected in sections 7.1 and 7.2. However this time, fig. 7.11 c) and d) show increase in frequencies of B_θ perturbations.

Spectrogram implies possible existence of magnetic island in interval of (15.0,18.5) ms. Closer analysis of signal across window of (18.20,18.85) ms in fig. 7.12 identifies a stable $m = 3$ island with exceptionally high dominant frequency of $f_{max} = 15.4$ kHz. Radial location of resonant surface $r_s/a = 0.74$ also implies that this island is slightly deeper in plasma than islands observed up till now (althought this is due to choice of global parameters). Taking $q(a) = 4.71$ into consideration, $n = 1$ and since $f = f_{max}/m = 5.13$ kHz, observed velocity of poloidal rotation is $v_\theta = 2.03$ km/s.

Once again, observed character of island rotation is not a singular case, but systematic occurence across experimental session. Moreover, whenever reference discharge without plasma position stabilization took place, $v_\theta \approx 0.7$ km/s typical for $m = 3$ islands was seen (as that in sections 7.1 and 7.2). Since B_R is of the same polarity across the whole plasma region (see fig. 4.8), net effect of eventual poloidal drift due to this field should be 0. Thus it seems that main cause of island v_θ acceleration might be accompanying effects of B_R presence. In order to investigate this matter, more dedicated experiments will need to take place, preferably within scope of joint experiment with probe measurements.

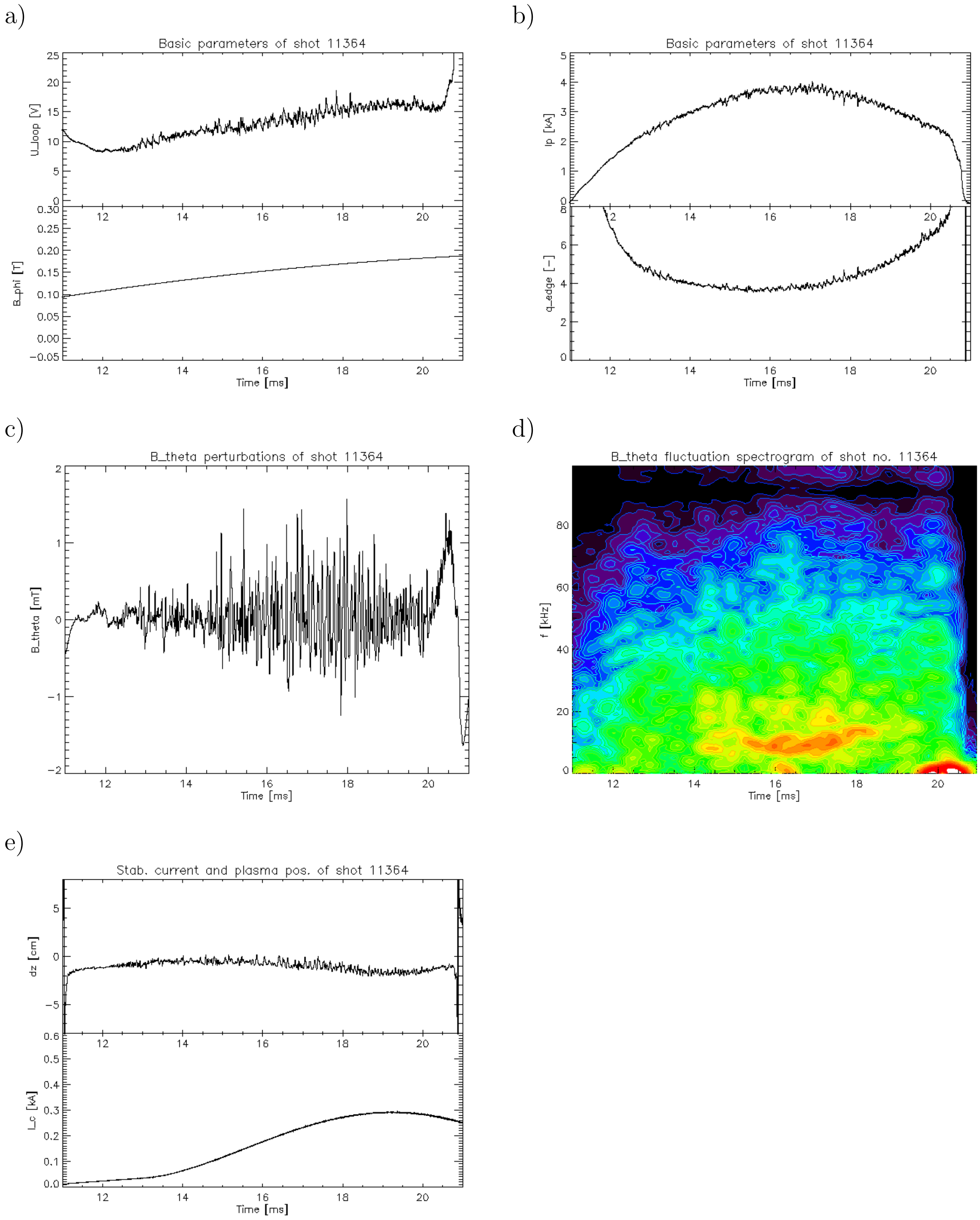

Figure 7.11: Global parameters of analyzed discharge. Fig. a) – U_{loop} and B_ϕ. Fig. b) – I_p and $q(a)$. Fig. c) – B_θ perturbations inside $f \in (1, 100)$ kHz band. Fig. d) – spectrogram of fig. c) data. Fig. e) – vertical plasma position estimation and I_c winding current per turn.

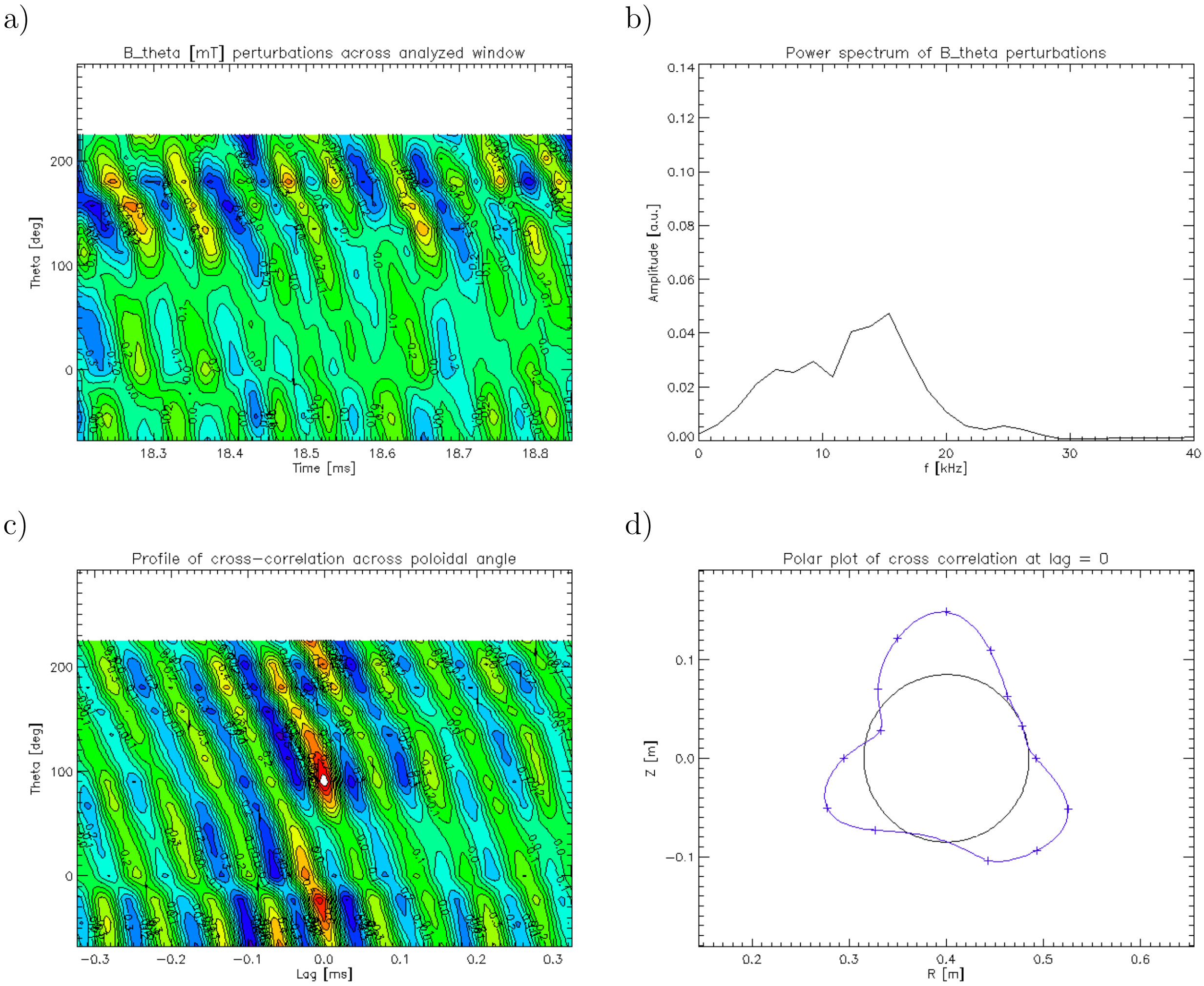

Figure 7.12: B_θ perturbations with $f \in (5, 30)$ kHz band-pass applied. Figure a) – signal profile. Figure b) – signal power spectrum. Figure c) – cross-correlation profile. Figure d) – polar plot of fig. c) at lag = 0.

Chapter 8

Summary

In this thesis, magnetic fields and methods of their measurement on tokamak GOLEM were characterized. These fields are generated by tokamak windings and its plasma and are most commonly detected with conducting inductive loops, or eventually with semi-conducting galvanometric elements. General principle of both approaches was described, followed by detailed overview of up-to date GOLEM magnetic diagnostics, including details of their calibration and practical application. All of these are inductive loops and are represented by toroidal and poloidal flux loop, Rogowski coil for I_p measurements, single saddle coil and most importantly – local magnetic field sensor used to detect B_ϕ and old Mirnov coils of $A_{eff} = 37$ cm^2 for high-frequency measurements of B_θ.

Possibilities of B_θ measurements were significantly enhanced by design, construction, calibration and implementation of a new array of magnetic diagnostics (named as *ring coils*), undertaken within scope of this thesis. Taking signal and bandwidth issues of coils into consideration, coil cyllinder dimensions follow $D = l$, with diameter D being largest possible. Due to dimensional constraints of new mechanical manipulator, two different coil types were made – with $A_{eff} = 163.4$ cm^2 and $A_{eff} = 84.5$ cm^2 respectively. Characterization and calibration of state-of-art Hall probe detectors from Poznan University of Technology has shown that these probes exhibit significantly higher temperature resistance than industrial-issue probes.

Current state of developed model of tokamak GOLEM vacuum field (i.e. pre-breakdown phase field) includes B_ϕ windings, external B_θ windings, 2D axisymmetric equivalent of iron core and tokamak chamber as a source of stray fields. B_ϕ model, as well as measurements, yield that toroidal field ripple is negligible across plasma region of tokamak GOLEM and that $1/R$ approximation of this field is sufficient. Measured and modelled B_θ show that presence of unsaturated iron core amplifies B_R field from vertical position stabilization windings by factor of 2.5-3, while for the rest of windings is its influence negligible. Comparison of stray fields model to systematic measurements has shown that on tokamak GOLEM, most of these fields come from current-drive windings upon saturation of transformer core.

For measurements of unperturbed B_θ of plasma (e.g. for plasma equilibrium reconstruction purposes), it is necessary to eliminate cross-talk signal from tokamak windings and stray fields. The best results are obtained by doing a vacuum discharge of the same parameters as those of shot with plasma, and then directly subtracting cross-talk signal obtained this way. Also, semi-analytical specification of cross-talk from winding currents can be trusted (with some reserves) up till maximum of I_p.

Simple numerical model of B_θ of plasma containing MHD structures has shown that rotating magnetic islands manifest their presence as B_θ perturbations across time and θ. For such a signal, cross-correlation analysis and FFT can be used to extract information of island structure and frequency of its rotation respectively. Use of analytical expression for $q(r)$ profile (with some additional assumptions) then provides also radial location of island resonant surface r_s and velocity of its poloidal rotation v_θ. In signal of real GOLEM islands of different m (althought $m = 3$ seems to be the most common one), there is observed a correlation of frequency of island rotation with temporal evolution of $q(a)$. The cause is most likely due to respective change of r_s location, while v_θ close to constant value is kept (for $m = 3$ islands, it is $v_\theta \approx 0.7$ km/s). Besides dependency of poloidal rotation on $q(a)$, a dependency on m of island ($m = 5$ islands exhibit $v_\theta \approx 0.2$ km/s) and presence of external B_R ($m = 3$ islands are accelerated to $v_\theta \approx 2.0$ km/s) was observed as well.

In the scope of future work, joint experiment with rake probe is suggested to further investigate the observed v_θ issues. Also, implementation of Hall effect probes on mechanical manipulator is planned, once necessary modifications are done. This is expected to enhance capacities for measurement of unperturbed plasma B_θ, which is incidentally the weakest point of ring coils applicability. Also, for better understanding of magnetic fields of tokamak GOLEM, implementation of a full 3D iron core model with $\mu_r(B)$ dependency is in progress.

References

[1] J.A. Wesson, *Tokamaks*, Clarendon Press, Oxford, 2004.

[2] J. Freidberg, *Plasma Physics and Fusion Energy*, Cambridge University Press, Cambridge, 2007.

[3] K. Lackner, et al, *Fusion Physics*, International Atomic Energy Agency, Vienna, 2012.

[4] EFDA, *Fusion Electricity - A roadmap to the realisation of fusion energy*, European Fusion Development Agreement, 2012.

[5] P. Kulhánek, *Úvod do teorie plazmatu* [Introduction to theory of plasma], Aldebaran Group for Astrophysics, Prague, 2011.

[6] V. S. Mukhovatov and V. D. Shafranov, "Plasma Equilibrium in a Tokamak," *Nuclear Fusion*, vol. 11, 1971.

[7] L. Bardos, F. Zacek, et al, *Experientální zařízení TOKAMAK TM-1-MH* [Experimental Device Tokamak TM-1-MH], Institute of Plasma Physics AV CR, Institute Report 35/77, December, 1977 (in Czech).

[8] I. Ďuran, "Fluktuace magnetického pole na tokamaku CASTOR" [Magnetic field fluctuations of tokamak CASTOR], doctoral dissertation, Dept. Electronics and Vacuum Physics, Faculty of Mathematics and Physics, Charles Univ. in Prague, 2003.

[9] M. Valovič, "Magnetic Diagnostics on the CASTOR Tokamak," *Czechoslovak Journal of Physics*, vol. B 38, 1988.

[10] V. Svoboda, et al, "Former Tokamak CASTOR Becomes Remotely Controllable GOLEM at the Czech Technical University in Prague," 37^{th} *EPS COnference on Plasma Physics*, June, 2010.

[11] E.J. Strait, et al, "Magnetic Diagnostics," *Fusion Science and technology*, vol. 53, 2008.

[12] S. Tumanski, "Induction coil sensors – a review," *Meas. Sci. Technol.*, vol. 18, 2007.

[13] I. H. Hutchinson, *Principles of Plasma Diagnostics*, Cambridge University Press, Cambridge, 2002.

[14] R. S. Popovic, *Series in Sensors: Hall Effect Devices*, IOP Publishing Ltd, Bristol, 2004.

[15] J. Brotánková, "Studium horkého plazmatu v experimentálních zařízeních typu Tokamak" [Study of High Temperature Plasma in Tokamak-like Experimental Devices], doctoral dissertation, Dept. Surface and Plasma Science, Faculty of Mathematics and Physics, Charles Univ. in Prague, 2009.

[16] W. Rogowski and W. Steinhaus, "Die Messnung der magnetischen Spannung," [The measurements of magnetic potential] *Arch. Elektrotechnik*, vol. 1, 1912.

[17] M. Valovič, "Control of plasma position in the CASTOR tokamak," *Czechoslovak Journal of Physics*, vol. B 39, 1989.

[18] E. J. Strait, "Magnetic diagnostic system of the DIII-D tokamak," *Rev. Sci. Instrum.*, vol. 77, 2006.

[19] R. F. Heeter, et al, "Fast magnetic fluctuation diagnostics for Alfven eigenmode and magnetohydrodynamics studies at the Joint European Torus," *Rev. Sci. Instrum.*, vol. 71, 2000.

[20] J. G. Bak, et al, "Performance of the magnetic sensor and the integrator for the KSTAR magnetic diagnostics," *Rev. Sci. Instrum.*, vol. 75, 2004.

[21] I. Štoll, *Elektřina a Magnetismus* [Electrics and Magnetism], Vydavatelství ČVUT, Prague, 1998 (in Czech).

[22] I. Ďuran, et al, "Magnetic measurements using array of integrated Hall sensors on the CASTOR tokamak," *Rev. Sci. Instrum.*, vol. 79, 2008.

[23] K. Kovařík, "Měření magnetických polí na fúzních reaktorech typu tokamak/stellarátor" [Measurement of magnetic field on tokamak/stellarator fusion reactors], diploma thesis, Dept. Nucl. Reactors, Faculty of Nuclear Sciences and Physical Engineering, Czech Tech. Univ. in Prague, 2009.

[24] M. Gryaznevich, T. G. Kilovataya and V. N. Pyatov, "Effect of ferromagnet on the equilibrium of a tokamak plasma," *Sov. J. Plasma Phys.*, vol. 9, 1983.

[25] B. C. Carlson, "Numerical computation of real or complex elliptic integrals," http://arXiv.org/abs/math/9409227v1, Sep, 1994.

[26] C. V. Atanasiu and L. E. Zakharov, "Description of magnetohydrodynamic equilibrium in iron core transformer tokamaks," *Nucl. Fusion*, vol. 30, 1990.

[27] E. R. Solano, et al, "Equilibrium and stability studies for an iron core tokamak with a poloidal divertor," *Nucl. Fusion*, vol. 30, 1990.

[28] D. P. Brien, et al, "Equilibrium analysis of iron core tokamaks using a full domain method," *Nucl. Fusion*, vol. 32, 1992.

[29] O. V. Tozoni and I. D. Mayergoiz, *Calculation of three-dimensional electromagnetic fields*, Tekhnika, Kiev, 1974.

[30] B. Cucic, "The 3D calculation of the quasistatic magnetic field around a current carrying conductor and ferromagnetic plate by means of integral equations," *Energija*, vol. 56, 2007.

[31] T. Oikawa, et al, "Evolution of current density profile associated with magnetic island formation in JT-60U," *Phys. Rev. Lett.*, vol. 94, 2005.

[32] S. V. Mirnov and I. B. Semenov, "Investigation of the Instabilities of the Plasma String in the Tokamak T-3 by Means of a Correlation Method," *Atomnaya Energiya*, vol. 30, 1971.

Contents

List of Figures

List of Tables